

Recent Advances in RF Propagation Modeling for 5G Systems

Lead Guest Editor: Mihajlo Stefanovic

Guest Editors: Stefan R. Panic, Rausley A. A. de Souza, and Juan Reig





Recent Advances in RF Propagation Modeling for 5G Systems

International Journal of Antennas and Propagation

Recent Advances in RF Propagation Modeling for 5G Systems

Lead Guest Editor: Mihajlo Stefanovic

Guest Editors: Stefan R. Panic, Rausley A. A. de Souza,
and Juan Reig



Copyright © 2017 Hindawi. All rights reserved.

This is a special issue published in "International Journal of Antennas and Propagation." All articles are open access articles distributed under the Creative Commons Attribution License, which permits unrestricted use, distribution, and reproduction in any medium, provided the original work is properly cited.

Editorial Board

Ana Alejos, Spain
Mohammad Ali, USA
Jaume Anguera, Spain
Rodolfo Araneo, Italy
Alexei Ashikhmin, USA
Herve Aubert, France
Paolo Baccarelli, Italy
Xiulong Bao, Ireland
Toni Björninen, Finland
Stefania Bonafoni, Italy
Paolo Burghignoli, Italy
Shah Nawaz Burokur, France
Giuseppe Castaldi, Italy
Luca Catarinucci, Italy
Felipe Catedra, Spain
Marta Cavagnaro, Italy
Shih Yuan Chen, Taiwan
Yu Jian Cheng, China
Renato Cicchetti, Italy
Riccardo Colella, Italy
Laura Corchia, Italy
Lorenzo Crocco, Italy
Claudio Curcio, Italy
Francesco D'Agostino, Italy
María Elena de Cos Gómez, Spain
Tayeb A. Denidni, Canada

Giuseppe Di Massa, Italy
Michele D'Urso, Italy
Francisco Falcone, Spain
Miguel Ferrando Bataller, Spain
Flaminio Ferrara, Italy
Vincenzo Galdi, Italy
Claudio Gennarelli, Italy
Farid Ghanem, Algeria
Sotirios K. Goudos, Greece
Rocco Guerriero, Italy
Kerim Guney, Turkey
Song Guo, Japan
Tamer S. Ibrahim, USA
M. R. Kamarudin, UK
Slawomir Koziel, Iceland
Luis Landesa, Spain
Ding-Bing Lin, Taiwan
Angelo Liseno, Italy
Pierfrancesco Lombardo, Italy
Lorenzo Luini, Italy
Atsushi Mase, Japan
Diego Masotti, Italy
C. F. Mecklenbräuker, Austria
A. T. Mobashsher, Australia
Ananda S. Mohan, Australia
Jose-Maria Molina-Garcia-Pardo, Spain

Giuseppina Monti, Italy
Giorgio Montisci, Italy
N. Nasimuddin, Singapore
Mourad Nedil, Canada
Symeon Nikolaou, Cyprus
Giacomo Oliveri, Italy
Ikmo Park, Republic of Korea
Josep Parrón, Spain
Matteo Pastorino, Italy
Xianming Qing, Singapore
Ahmad Safaai-Jazi, USA
Safieddin Safavi-Naeini, Canada
Magdalena Salazar-Palma, Spain
Stefano Selleri, Italy
Raffaele Solimene, Italy
Gino Sorbello, Italy
Seong-Youp Suh, USA
Sheng Sun, Hong Kong
Larbi Talbi, Canada
Luciano Tarricone, Italy
Parveen Wahid, USA
Wen-Qin Wang, China
Shiwen Yang, China
Yuan Yao, China

Contents

Recent Advances in RF Propagation Modeling for 5G Systems

Mihajlo Stefanovic, Stefan R. Panic, Rausley A. A. de Souza, and Juan Reig
Volume 2017, Article ID 4701208, 5 pages

The Complex α - μ Fading Channel with OFDM Application

Wander H. M. Freitas, Roberto C. D. V. Bomfin, Rausley A. A. de Souza, and Michel Daoud Yacoub
Volume 2017, Article ID 2143541, 7 pages

Performance Analysis of 5G Transmission over Fading Channels with Random IG Distributed LOS Components

Dejan Jaksic, Risto Bojovic, Petar Spalevic, Dusan Stefanovic, and Slavisa Trajkovic
Volume 2017, Article ID 4287586, 4 pages

60 GHz Modular Antenna Array Link Budget Estimation with WiGig Baseband and Millimeter-Wave Specific Attenuation

Joongheon Kim, Liang Xian, and Ali S. Sadri
Volume 2017, Article ID 9073465, 9 pages

Novel Method for 5G Systems NLOS Channels Parameter Estimation

Vladeta Milenkovic, Stefan Panic, Dragan Denic, and Dragan Radenkovic
Volume 2017, Article ID 5236246, 5 pages

Validation of the Decomposition Method for Fast MIMO Over-the-Air Measurements

Bernhard Auinger, Thomas Zemen, Michael Gadringer, Adam Tankielun, Christoph Gagern, and Wolfgang Bösch
Volume 2017, Article ID 8284917, 18 pages

Attenuation by a Human Body and Trees as well as Material Penetration Loss in 26 and 39 GHz Millimeter Wave Bands

Qi Wang, Xiongwen Zhao, Shu Li, Mengjun Wang, Shaohui Sun, and Wei Hong
Volume 2017, Article ID 2961090, 8 pages

Measured Performance Comparisons between Spatial Multiplexing and Beamforming Arrays in the 28 GHz Band

Dazhi Piao, Xingning Jia, Xiaochuan Ma, Qingxin Guo, and Zengrui Li
Volume 2017, Article ID 7253623, 9 pages

Novel Method for Optimal Synthesis of 5G Millimeter Wave Linear Antenna Array

Zarko Rosic, Olivera Mihic, Danijela Aleksic, and Dejan Drajić
Volume 2017, Article ID 6848234, 6 pages

Outage Analysis of Multihop Wireless Backhaul Using Millimeter Wave under Blockage Effects

Haejoon Jung and In-Ho Lee
Volume 2017, Article ID 4519365, 9 pages

Editorial

Recent Advances in RF Propagation Modeling for 5G Systems

Mihajlo Stefanovic,¹ Stefan R. Panic,² Rausley A. A. de Souza,³ and Juan Reig⁴

¹Faculty of Electrical Engineering, University of Nis, Nis, Serbia

²Faculty of Natural Science and Mathematics, University of Pristina, Kosovska Mitrovica, Serbia

³National Institute of Telecommunications (Inatel), Santa Rita do Sapucaí, MG, Brazil

⁴Institute of Telecommunications and Multimedia Applications (iTEAM), Universitat Politècnica de Valencia, Valencia, Spain

Correspondence should be addressed to Stefan R. Panic; stefanpnc@yahoo.com

Received 30 July 2017; Accepted 30 July 2017; Published 15 October 2017

Copyright © 2017 Mihajlo Stefanovic et al. This is an open access article distributed under the Creative Commons Attribution License, which permits unrestricted use, distribution, and reproduction in any medium, provided the original work is properly cited.

Continuously increasing demand for higher data rates, larger network capacity, higher energy efficiency, and higher mobility has motivated research within fifth-generation (5G) communication systems modeling. 5G is generally agreed for a set of new requirements for wireless communications systems. These requirements will need to address several critical performance areas including cost constraints, traffic latency, reliability, security, availability, heterogeneous structure of networks, multicast/broadcast requirements, the requirement to serve a variety of different devices, and reduced energy consumption. Accurate 5G indoor and outdoor channel characterization and modeling are crucial for determining the system performance and thus for system and for 5G network realization. Namely, 5G radio frequency (RF) propagation is affected by various phenomena that more or less deteriorate the original transmitted signal arriving at the receiver (free-space propagation, object penetration, reflection, scattering, diffraction, and absorption caused by atmospheric gases, fog, and precipitation).

To generate reliable propagation models for 5G systems and further to determine standard performance measurements of 5G systems, corresponding path loss models must be built for link budget evaluation and signal strength prediction, with the inclusion of directional and beamforming antenna arrays and cochannel interference, while temporal dispersion caused by multipath propagation (impacting the timing, packet and frame sizes, and other air interface design parameters) should also be characterized. Therefore, general statistical models could not be sufficient in order to assess

the performance of system and specific models related to real-world reference scenarios with fine classification of terms will be required.

For the development of new 5G systems to operate in millimeter bands, there is a need for accurate propagation modeling at these bands. Exploitation of unused millimeter wave (mmWave) band spectrum (spectrum between 6 and 300 GHz) is an efficient solution for meeting the standards for 5G networks enormous data demand growth explosion. Measurements provided at 38 GHz (Base Station-to-Mobile Access Scenario [1] and Peer-to-Peer Scenario [2]), 60 GHz (Peer-to-Peer Scenario and Vehicular Scenario [3]), and 73 GHz [4] have clearly identified the existence of non-line-of-sight (NLOS) conditions. One of the most intensively used statistical models for characterizing the complex behavior and random nature of NLOS fading envelope is the Nakagami- m distribution. In [5–7] for the purpose of modeling observed 5G system propagation properties, the Nakagami- m parameter is directly computed from the measured data. Two most well-known procedures used for the estimation of the Nakagami- m fading parameter, m , are (1) maximum likelihood (ML) estimation and (2) moment-based estimation. However, it is known that sample moments are often subjected to the effects of outliers (even a small portion of extreme values, outliers, can affect the Gaussian parameters, especially the higher order moments). Moreover, occurrence of outliers is especially problematic when higher order sample moments are used for estimation, since estimation inaccuracy arises in such cases. Providing the best

moment-based estimator is still major issue that should be addressed.

Because of that, there is a need for developing a novel approach for NLOS channels parameter estimation based on performance measurements, which will enable us to estimate propagation parameters in real time and to avoid weaknesses of ML and moment-method estimation approaches.

Stochastic channel models for mmWave communications in both indoor and outdoor environments have been mostly characterized with a Rician distribution in line-of-sight (LOS) environments where a dominant path is present [8]. In [8] it has been shown that Ricean K -factor is ranging over a defined set of values for observed LOS and NLOS conditions in vertical-to-vertical (V-V) copolarized antenna scenario and corresponding set of values for observed LOS and NLOS conditions vertical-to-horizontal (V-H) cross-polarized antenna scenario. However, despite the fact shown in [8] that Rician distribution provides the best fit to the measurement data, results of [8] imply that conventional fading models fall short of accurate modeling of the random fluctuations of 5G wireless channel signal. In [9] it has been concluded that for accurate 5G systems channel modeling, proposed models should ensure that the channel LOS and NLOS conditions, the second-order statistics of the channel, and the channel realizations should change smoothly in the function of time, antenna position, and/or frequency. Therefore a need arises for novel characterization of propagation in LOS conditions, by observing Ricean K -factor as a random process.

In particular, the diversity of scenarios envisaged for the 5G applications at the mmWave band will certainly lead to a variety of propagation conditions. Currently, an enormous variety of waveforms are considered to be potential candidates for the 5G air interface. They include (i) single-carrier frequency division multiplexing (SC-FDMA), already used in 4G Long-Term Evolution (LTE) uplink, also called differently generalized discrete Fourier transforms- (GDFTs-) orthogonal frequency division multiplexing (OFDM) [10]; (ii) zero-tail (ZT) or unique-word (UW) DFT-spread-OFDM [11, 12], ultra-wideband- (UW-) OFDM, generalized frequency division multiplexing (GFDM) [13], and cyclic prefix- (CP-) OFDM (already used in the 4G LTE downlink); (iii) resource-block-filtered OFDM, filter-bank-multicarrier (FBMC), and universal filter multicarrier (UFMC). As it can be seen, the OFDM technique is omnipresent in the 5G waveform proposals. The OFDM technique shall certainly remain as the root framework for the new 5G waveform design, with some optimization to support the new 5G requirements [14, 15].

Therefore it is necessary to propose an efficient, simple, and general method to generate samples for general 5G channel and further to make use of this channel in order to assess the bit error rate performance of an OFDM system model.

Stochastic geometry has been a powerful technique to evaluate system performance in conventional cellular networks [16], which reveals the impacts of multiple system parameters such as base station density, transmit power, and path loss exponent on the performance parameters such as data rate or reliability. The key idea in [17] is to model

random obstacles (e.g., buildings) as rectangles with random sizes and orientations whose centers form a Poisson point process (PPP) in 2-dimensional space. However, instead of one-hop communication between the macro cell base station (MBS) and a single small cell base station (SBS) cluster, the 5G cellular networks may have multiple SBS clusters, which require multihop transmissions to improve the cell coverage. Considering the distance-dependence of the blockage effects (i.e., the likelihood of a blockage event increases as the distance increases) at mmWave, multihop communication can be an effective solution to build mmWave wireless backhaul systems. In this context, motivated by the limitation in [18], the single-hop wireless backhaul system from [18] can be extended to a multihop scenario with multiple SBS clusters. Multiple points-to-multiple-points (MBMs-to-MBMs) links could be also studied, instead of [18] single-point-to-multiple-points (MBS-to-SBSs) links. Therefore, with different distance statistics from [18], the intercluster SBS-to-SBS communication can benefit from higher order of spatial diversity compared to the MBS-to-SBS communication in [18].

From this point of view, the analysis of an optimal and suboptimal hop count to minimize the end-to-end outage performance between the MBS and the destination SBS cluster for a given end-to-end distance could be of interest, where the suboptimal hop count is based on only the per-hop outage performance.

Interference issues will become of crucial importance due to the coexistence of 5G devices, since a number of mmWave devices are expected to grow extensively in the near future [19]. In order to satisfy 5G quality-of-standard requirements and meet user mobility, due to the higher path loss at mmWave frequency range, multiple antenna arrays could be used in outdoor mmWave systems for providing an additional gain [20, 21]. The increasing growth of 5G devices number will prompt the study of array pattern nulling techniques. The objectives of design of the antenna arrays are to achieve a minimum side lobe level (SLL) and a narrow first null beam width (FNBW). Methods used for the antenna array synthesis can be classified into two categories: deterministic and stochastic. The biggest advantages of using stochastic methods are their ability in dealing with large number of optimization parameters and avoiding getting stuck in local minimum.

An interesting idea for 5G mmWave antenna array synthesis could be based on genetic algorithm for the synthesis of linear array with nonuniform interelement spacing in order to obtain the optimal position of the elements in order to obtain the minimum side lobe level and nulls in desired directions.

The use of mmWave bands for next-generation wireless systems could offer ultra-wideband spectrum availability and increased channel capacity. All these benefits come at the expense of potentially higher system complexity particularly in terms of radio frequency (RF) front end and antenna design. However, the recent advancements around mmWave wireless systems development have produced cost-effective solutions that can be leveraged to overcome these challenges. 60 GHz frequency band has its own standardized protocol,

that is, the Wireless Gigabit Alliance (WiGig) standard which is equivalent to IEEE 802.11ad [22]. A promising study would be the link budget estimation, performed based on WiGig/IEEE 802.11ad standard-defined modulation and coding scheme (MCS) modes and 60 GHz mmWave specific path loss and auxiliary attenuation factors. The considered systems parameters for this link budget estimation could be obtained from real-world hardware prototypes for next-generation mmWave mesh backhaul networks in industry.

Although multiple-input and multiple-output (MIMO) techniques have been widely employed in cellular and wireless local area network systems working at sub-6 GHz [23–25], the potential realizations of MIMO technique in mmWave band are not fully understood yet, considering the unique multipath propagation characteristics and the increased path loss over the lower frequency bands used in current 3G/4G wireless communication. Spatial multiplexing (SM) and beamforming (BF) are the two most commonly used approaches to realize a MIMO system. The multiplexing gain can be obtained by exploiting the spatial difference of the channel response in different transmit- (Tx-) receive (Rx) element pair. On the other hand, in the mmWave band, the propagation loss is higher compared to the lower frequencies; thus the high-gain antenna arrays are expected to compensate the increased path loss. Several researches have conducted analyses on the performance of SM and BF in the mmWave communications. The feasibility of indoor mmWave MIMO has been investigated by ray-tracing based channel modeling, by virtual antenna array based channel measurement [26, 27], and also by a 2×2 microstrip array in an underground mine environment [28]. The performance of a hybrid transmission combining BF and SM in mmWave communication is also analyzed based on a ray-tracing method in both LOS and multipath environment [29].

It could be of interest to provide the measurement-based channel capacity comparison between SM and BF under realistic antenna arrays, with the same Tx power, the same array position, and the same propagation condition. In particular, a SM system could be analyzed and divided into 4 subarrays, each one of them consisting of 4 elements, corresponding to a 4×4 MIMO system, while in the BF system, the antenna array could be constructed by the whole 16 elements, which corresponds to a single-input and single-output (SISO) system but with a larger array gain than that of the SM system.

The introduction of MIMO and receiver diversity wireless devices provides large gains in the throughput performance. These gains are highly dependent on the performance of the receiving-antenna system and the receiving algorithm [30]. The devices can change the behavior of the antenna systems, for example, by using beamforming mechanisms, and also can adapt software algorithms to suit the environment they are currently used in. Wireless equipment manufacturers as well as network providers are pushing to have performance tests of the hand-held devices. Network providers expect to recommend the user equipment (UE) with the best performance to their customers; manufacturers wish to be able to compare the quality of their own UE to the one of the competitors. These comparisons should include

the effect of the antenna systems, the analog frontends, digital receiving algorithms, and baseband processing. One of the methods proposed by 3GPP, yet very promising one, is the decomposition method (DM). Over-the-air (OTA) throughput tests of wireless MIMO devices are an important tool for network operators and manufacturers. The UE is placed in an anechoic chamber and a random fading process is emulated by a base station emulator (BSE). The antenna characteristic of the UE is taken into account by sampling the sphere around the UE with the BSE test antenna at a large number of positions. For low-variance throughput results, long measurement intervals over many fading realizations are required, leading to long and expensive measurement periods in an anechoic chamber. Analyzing the possibilities of speeding up OTA testing through upgrading methods for DM analysis could be interesting task in performing throughput testing of wireless MIMO devices.

Attenuation by a human body and trees and penetration losses of material at the ITU proposed frequency bands [31], 24.25–27.5 and 37–40.5 GHz, are important issues for future 5G wireless access systems. In [31] the attenuation by a human body and trees and penetration loss of different materials with 1 GHz bandwidth were measured with a time domain channel sounder at 26 and 39 GHz, respectively. As far as we know, there are no measurements and modeling work reported in open literature on human blockage, attenuation by trees, and penetration loss of different materials at 24.25–27.5 and 37–40.5 GHz frequency bands. The prediction of attenuation by a human body and trees and the penetration losses in this work are important and necessary for future mmWave wireless communication systems deployment. By considering a human body as an infinite absorbing screen, two knife-edge (KE) models were used to predict the attenuation by a person in a frequency range from 4 to 10 GHz in [32]. In addition to regarding a human body as an absorbing screen, a cylindrical model by uniform theory of diffraction (UTD) was also applied to predict human body attenuation. Measurements in [33, 34] were performed at 10 GHz which showed a strong correlation between a human body and a perfect conducting cylinder. Previous works about penetration losses of material in mmWave bands were focused on 28 GHz and 60 GHz. In [35], signals through a hollow plasterboard wall resulted in a penetration loss ranging between 5.4 dB and 8.1 dB. In [36], the measured penetration losses are 2 dB, 9 dB, and 35.5 dB at 60 GHz through a glass door, a plasterboard wall with metallic studs, and a wall with a metal-backed blackboard, respectively. For this reason, it would be of interest to carry out measurements of the attenuation at 26 and 39 GHz by a human body and trees as well as penetration losses for material with a person lateral crossing the transceiver connection line and to use KE and UTD methods to predict its attenuation. Also it would be of interest to measure the attenuation by willow trees at 26 GHz and then to compare with ITU-R P-833-8 model and modify the model at 26 GHz. An interesting investigation would also be carrying out measurements of the penetration loss for different materials as well, for example, transparent glass with different thickness, frosted glass, and wood with plastic clad.

5G wireless communication networks are expected to fulfill the demand for higher data rates, lower latency, and/or massive connectivity of a growing number of users/devices exploiting a variety of wireless applications. This envisioned rapid increase in the use of wireless services would lead the wireless research community to start looking at new technologies to address problems related to the RF propagation modeling. This includes the development of models for new concepts such as massive MIMO systems to improve the spectral efficiency at the link and network layers and developing novel propagation models for characterizing communication in particular in the upper mmWave.

Generally, we need to continue to progress in our research for appropriate 5G radio propagation models, which can adequately and faithfully model mmWave communication properties much more than what has been done at the moment. The progress reported in this Special Edition is just a small step in achieving this goal in the future.

Mihajlo Stefanovic
Stefan R. Panic
Rausley A. A. de Souza
Juan Reig

References

- [1] T. S. Rappaport, E. Ben-Dor, J. N. Murdock, and Y. Qiao, "Proceeding of the 38 GHz and 60 GHz angle-dependent propagation for cellular & peer-to-peer wireless communications," in *Proceedings of the IEEE International Conference on Communications (ICC '12)*, pp. 4568–4573, Ottawa, ON, Canada, June 2012.
- [2] T. S. Rappaport, F. Gutierrez, E. Ben-Dor, J. N. Murdock, Y. Qiao, and J. I. Tamir, "Broadband millimeter-wave propagation measurements and models using adaptive-beam antennas for outdoor Urban cellular communications," *IEEE Transactions on Antennas and Propagation*, vol. 61, no. 4, pp. 1850–1859, 2013.
- [3] E. Ben-Dor, T. S. Rappaport, Y. Qiao, and S. J. Lauffenburger, "Millimeter-wave 60 GHz outdoor and vehicle AOA propagation measurements using a broadband channel sounder," in *Proceedings of the 54th Annual IEEE Global Telecommunications Conference: "Energizing Global Communications" (GLOBECOM '11)*, Kathmandu, Nepal, December 2011.
- [4] G. R. Maccartney Jr. and T. S. Rappaport, "73 GHz millimeter wave propagation measurements for outdoor urban mobile and backhaul communications in New York City," in *Proceedings of the 1st IEEE International Conference on Communications (ICC '14)*, pp. 4862–4867, Sydney, Australia, June 2014.
- [5] S. K. Yoo, S. L. Cotton, R. W. Heath, and Y. J. Chun, "Measurements of the 60 GHz UE to eNB Channel for Small Cell Deployments," *IEEE Wireless Communications Letters*, vol. 6, no. 2, pp. 178–181, 2017.
- [6] D. Beauvarlet and K. L. Virga, "Measured characteristics of 30-GHz indoor propagation channels with low-profile directional antennas," *IEEE Antennas and Wireless Propagation Letters*, vol. 1, pp. 87–90, 2002.
- [7] J. Reig, M.-T. Martínez-Inglés, L. Rubio, V.-M. Rodrigo-Peñarocha, and J. Molina-García-Pardo, "Fading evaluation in the 60 GHz band in line-of-sight conditions," *International Journal of Antennas and Propagation*, vol. 2014, Article ID 984102, 12 pages, 2014.
- [8] M. K. Samimi, G. R. Maccartney, S. Sun, and T. S. Rappaport, "28 GHz millimeter-wave ultrawideband small-scale fading models in wireless channels," in *Proceedings of the 83rd IEEE Vehicular Technology Conference, VTC Spring 2016*, May 2016.
- [9] K. Haneda, L. Tan, Y. Zheng et al., "5G 3GPP-like channel models for outdoor urban microcellular and macrocellular environments," in *Proceedings of the 2016 IEEE 83rd Vehicular Technology Conference (VTC Spring)*, pp. 1–7, Nanjing, China, May 2016.
- [10] G. Berardinelli, K. I. Pedersen, T. B. Sørensen, and P. Mogensen, "Generalized DFT-Spread-OFDM as 5G Waveform," *IEEE Communications Magazine*, vol. 54, no. 11, pp. 99–105, 2016.
- [11] G. Berardinelli, F. M. L. Tavares, T. B. Sørensen, P. Mogensen, and K. Pajukoski, "Zero-tail DFT-spread-OFDM signals," in *Proceedings of the 2013 IEEE Globecom Workshops, GC Wkshps 2013*, pp. 229–234, Atlanta, Ga, USA, December 2013.
- [12] A. Sahin, R. Yang, M. Ghosh, and R. L. Olesen, "An improved unique word DFT-spread OFDM scheme for 5G systems," in *Proceedings of the IEEE Globecom Workshops, GC Wkshps 2015*, USA, December 2015.
- [13] N. Michailow, M. Matthe, I. S. Gaspar et al., "Generalized frequency division multiplexing for 5th generation cellular networks," *IEEE Transactions on Communications*, vol. 62, no. 9, pp. 3045–3061, 2014.
- [14] B. Farhang-Boroujeny and H. Moradi, "OFDM Inspired Waveforms for 5G," *IEEE Communications Surveys & Tutorials*, vol. 18, no. 4, pp. 2474–2492, 2016.
- [15] X. Zhang, L. Chen, J. Qiu, and J. Abdoli, "On the Waveform for 5G," *IEEE Communications Magazine*, vol. 54, no. 11, pp. 74–80, 2016.
- [16] T. Bai, R. Vaze, and R. W. Heath, "Analysis of blockage effects on urban cellular networks," *IEEE Transactions on Wireless Communications*, vol. 13, no. 9, pp. 5070–5083, 2014.
- [17] A. Ghosh, N. Mangalvedhe, R. Ratasuk et al., "Heterogeneous cellular networks: from theory to practice," *IEEE Communications Magazine*, vol. 50, no. 6, pp. 54–64, 2012.
- [18] H. Jung and I.-H. Lee, "Outage analysis of millimeter-wave wireless backhaul in the presence of blockage," *IEEE Communications Letters*, vol. 20, no. 11, pp. 2268–2271, 2016.
- [19] S. Rangan, T. S. Rappaport, and E. Erkip, "Millimeter-wave cellular wireless networks: potentials and challenges," *Proceedings of the IEEE*, vol. 102, no. 3, pp. 366–385, 2014.
- [20] J. Zhang, X. Ge, Q. Li, M. Guizani, and Y. Zhang, "5G millimeter-wave antenna array: design and challenges," *IEEE Wireless Communications Magazine*, pp. 2–8, 2016.
- [21] F. Long and C. Zhang, *Signal Processing for 5G: Algorithms and Implementations*, Wiley-IEEE, 2016.
- [22] T. S. Rappaport, J. N. Murdock, and F. Gutierrez, "State of the art in 60-GHz integrated circuits and systems for wireless communications," *Proceedings of the IEEE*, vol. 99, no. 8, pp. 1390–1436, 2011.
- [23] H. Sampath, S. Talwar, J. Tellado, V. Erceg, and A. Paulraj, "A fourth-generation MIMO-OFDM broadband wireless system: design, performance, and field trial results," *IEEE Communications Magazine*, vol. 40, no. 9, pp. 143–149, 2002.
- [24] Q. H. Li, G. J. Li, W. Lee et al., "MIMO techniques in WiMAX and LTE: a feature overview," *IEEE Communications Magazine*, vol. 48, no. 5, pp. 86–92, 2010.
- [25] J. Kim and I. Lee, "802.11 WLAN: history and new enabling MIMO techniques for next generation standards," *IEEE Communications Magazine*, vol. 53, no. 3, pp. 134–140, 2015.

- [26] M.-T. Martinez-Ingles, D. P. Gaillot, J. Pascual-Garcia, J.-M. Molina-Garcia-Pardo, M. Lienard, and J.-V. Rodríguez, "Deterministic and experimental indoor mmW channel modeling," *IEEE Antennas and Wireless Propagation Letters*, vol. 13, pp. 1047–1050, 2014.
- [27] S. Ranvier, C. Icheln, and P. Vainikainen, "Measurement-based mutual information analysis of MIMO antenna selection in the 60-GHz band," *IEEE Antennas and Wireless Propagation Letters*, vol. 8, pp. 686–689, 2009.
- [28] I. Ben Mabrouk, J. Hautcoeur, L. Talbi, M. Nedil, and K. Hettak, "Feasibility of a millimeter-wave MIMO System for short-range wireless communications in an underground gold mine," *IEEE Transactions on Antennas and Propagation*, vol. 61, no. 8, pp. 4296–4305, 2013.
- [29] S. J. Lee and W. Y. Lee, "Capacity of multiple beamformed spatial stream transmission in millimetre-wave communication channels," *IET Communications*, vol. 7, no. 12, pp. 1263–1268, 2013.
- [30] M. D. Foegelle, "Creating a complex multipath environment simulation in an anechoic chamber," *Microwave Journal*, vol. 53, no. 8, pp. 56–64, 2010.
- [31] ITU, in *Proceedings of the World Radio Communication Conference (WRC '15)*, Geneva, Switzerland, 2015, ITU 500-E.
- [32] J. Kunisch and J. Pamp, "Ultra-wideband double vertical knife-edge model for obstruction of a ray by a person," in *Proceedings of the IEEE International Conference on Ultra-Wideband (ICUWB '08)*, pp. 17–20, Hannover, Germany, September 2008.
- [33] M. Ghaddar, L. Talbi, and T. A. Denidni, "Human body modelling for prediction of effect of people on indoor propagation channel," *IEEE Electronics Letters*, vol. 40, no. 25, pp. 1592–1594, 2004.
- [34] M. Ghaddar, L. Talbi, T. A. Denidni, and A. Sebak, "A conducting cylinder for modeling human body presence in indoor propagation channel," *IEEE Transactions on Antennas and Propagation*, vol. 55, no. 11, pp. 3099–3103, 2007.
- [35] E. J. Violette, R. H. Espeland, R. O. DeBolt, and F. Schwering, "Millimeter-wave propagation at street level in an urban environment," *IEEE Transactions on Geoscience and Remote Sensing*, vol. 26, no. 3, pp. 368–380, 1988.
- [36] K. Sato, T. Manabe, T. Ihara et al., "Measurements of reflection and transmission characteristics of interior structures of office building in the 60-GHz band," *IEEE Transactions on Antennas and Propagation*, vol. 45, no. 12, pp. 1783–1792, 1997.

Research Article

The Complex α - μ Fading Channel with OFDM Application

Wander H. M. Freitas,¹ Roberto C. D. V. Bomfin,²
Rausley A. A. de Souza,¹ and Michel Daoud Yacoub³

¹National Institute of Telecommunications (Inatel), P.O. Box 05, 37540-000 Santa Rita do Sapucaí, MG, Brazil

²Vodafone Chair Mobile Communication Systems, Technische Universität Dresden, 01062 Dresden, Germany

³Wireless Technology Laboratory (WissTek), Department of Communications, School of Electrical and Computation Engineering, State University of Campinas, Campinas, SP, Brazil

Correspondence should be addressed to Rausley A. A. de Souza; rausleyaas@gmail.com

Received 9 December 2016; Accepted 4 July 2017; Published 17 August 2017

Academic Editor: Giuseppe Castaldi

Copyright © 2017 Wander H. M. Freitas et al. This is an open access article distributed under the Creative Commons Attribution License, which permits unrestricted use, distribution, and reproduction in any medium, provided the original work is properly cited.

The aims of this paper are threefold: (i) to present a model for the complex α - μ fading channel; (ii) to propose an efficient, simple, and general method to generate complex α - μ samples; (iii) to make use of this channel in order to assess the bit error rate performance of an OFDM system. An analytical framework is then used, whose output is validated through Monte Carlo simulation. Several important conclusions concerning the system performance as a function of the channel parameters, namely, nonlinearity, clustering, and power imbalance of in-phase and quadrature components, are drawn.

Dedicated to the memory of our beloved and brilliant friend Wander Henrique Machado Freitas, the first author of this paper, who passed away in December 16, 2016, one week after the submission of this paper

1. Introduction

Wireless communication channels are subject to fading, with the received signal varying in a random manner [1, 2]. Because signal variation deteriorates the performance of the communication systems, the correct characterization of the phenomenon is of paramount importance. It is widely understood that the signal oscillates on a statistical basis with several short-term distributions adequately describing this variation. One of such distributions, arising from the α - μ fading model [3], describes the small-scale variations of the signal in a highly diffuse scattering environment. It is a general, flexible, and mathematically easily tractable distribution which models the nonlinearity of the propagation medium, given by the parameter α , as well as the multipath clustering of the radio waves, given by the parameter μ . It includes important and widely accepted distributions such as Gamma, Nakagami- m , exponential, Weibull, one-sided Gaussian, and Rayleigh. Specifically, for $\alpha = 2$ and $\mu = m$, the α - μ model becomes the Nakagami- m one with m representing the degree

of fading. For $\mu = 1$, α - μ deteriorates into Weibull. It is noteworthy that α - μ , as well as Nakagami- m , was initially conceived to model only the signal envelope. Therefore, their corresponding phases constitute an open matter. In several applications, however, the characterization of the phase may be critical, and a model for it is certainly of interest. In the absence of the knowledge of the phase statistics, and for simplicity, some researchers have adopted the uniform phase distribution. However, this is a rather simplistic assumption, since it is hard to imagine a fading signal with uniform distribution whose envelope approximately ranges from Hoyt to Rice, Hoyt and Rice themselves having nonuniform phases. In an attempt to fill this gap, in [4], a complex fading model leading to Nakagami- m envelope and nonuniform phase distribution was proposed. Such a model was then improved in [5] to account for power, or, equivalently, clustering, imbalance between in-phase and quadrature components. It is noteworthy that the Nakagami- m complex model has already been validated in practice through field measurements [6].

The increase of the demand for wireless services has led the systems to operate in a variety of environments. In particular, the diversity of scenarios envisaged for the fifth generation (5G) applications at the millimeter wave (mmWave) band will certainly lead to a variety of propagation conditions, which may not be characterized by simpler fading models. The widely used distributions, such as Rayleigh [7], Hoyt [8], Rice [9], Nakagami- m [10], and Weibull [11], will still find their place, of course, but they are less flexible for encompassing more sophisticated situations. One general and rather flexible, yet simple, model such as α - μ [3] may serve this purpose. Interestingly enough, the α - μ fading distribution has shown yielding an excellent curve fitting performance with real field data collected at a mmWave band, namely, 60 GHz [12].

In [13], a very general, probably the most general, complex short-term model, the α - η - κ - μ fading model, was proposed. Such a model comprises as special cases a number of important distributions, for example, α - μ , η - μ , κ - μ , and η - κ (Beckmann), already widely explored in the literature. Hence, it is possible to specialize the α - η - κ - μ model into the complex α - μ scenario with an aim at assessing some wireless performance metrics upon which in-phase and quadrature distributions may impact. And this is one of the objectives of this paper.

Currently, an enormous variety of waveforms are considered to be potential candidates for the 5G air interface. They include (i) Single-Carrier Frequency Division Multiplexing, also called differently cyclic prefix (CP) DFT-Spread-OFDM (already used in 4G LTE uplink), G-DFT-s-OFDM [14]; (ii) Zero-Tail (ZT) or Unique-Word (UW) DFT-Spread-OFDM [15, 16], UW-OFDM, GFDM [17], CP-OFDM (already used in the 4G LTE downlink); (iii) Resource-Block-Filtered OFDM, Filter-Bank-Multicarrier (FBMC), and Universal Filter Multicarrier (UFMC). As can be seen, the OFDM technique is omnipresent in the 5G waveform proposals. The OFDM technique shall certainly remain as the root framework for the new 5G waveform design, with some optimization to support the new 5G requirements [18, 19].

This paper makes use of the complex α - μ fading channel to assess the bit error rate (BER) performance of a BPSK-based OFDM system. In particular, it generalizes the results of [20], in which such a performance metric was carried out for the Nakagami- m case. The generalization approaches two important issues concerning their impact on the system performance: (i) the effect of the nonlinearity parameter; (ii) the effect of the power (or, equivalently, clustering) imbalance between in-phase and quadrature components. The analytical results are contrasted with simulation and a perfect agreement between them is found.

As a by-product of our main investigation, we propose an efficient method for generating complex α - μ random variables, in which clustering imbalance is found. It is noteworthy that the proposed α - μ variate generation method is simple and can be used in several other scenarios.

The paper is organized as follows. In Section 2, we present the complex α - μ model highlighting its main statistics, namely, the probability density function (PDF) of the envelope, phase, and the joint PDF of in-phase and quadrature

components. Section 3 presents an efficient, simple, and general method to generate α - μ random variables. Section 4 details the procedure used to estimate the BER in a given subcarrier. The results both for the simulation algorithm and for the BER performance are shown in their respective sections. Finally, Section 5 concludes the paper.

2. The Complex α - μ Model

This section introduces the complex α - μ model. The complex α - μ random variable Z is defined as

$$Z = X + jY, \quad (1)$$

where X and Y correspond to the in-phase and quadrature components. Define $R = |Z|$ and $\Theta = \arg(Z)$ as the envelope (modulus) and the phase (argument) of the complex α - μ variate, respectively. The PDF $f_R(r)$ of the envelope R is known to be given by [3]

$$f_R(r) = \frac{\alpha \hat{r}^\mu r^{\alpha\mu-1}}{\hat{r}^{\alpha\mu} \Gamma(\mu)} \exp\left(-\mu \frac{r^\alpha}{\hat{r}^\alpha}\right), \quad (2)$$

with $r \geq 0$, and (i) $\alpha > 0$ describes the nonlinearity of the propagation medium; (ii) $\mu > 0$ represents the number of multipath clusters adding up at the receiver; (iii) $\hat{r} = \sqrt[\alpha]{\mathbb{E}[R^\alpha]}$ is the α -root mean value of the envelope; (iv) $\mathbb{E}[\cdot]$ is the expectation operator; (v) and $\Gamma(\cdot)$ is the Gamma function [21, eqn. (6.1.1)]. As already mentioned, as far as the envelope statistics are concerned, the α - μ random variable includes the Gamma (and its discrete versions Erlang and central Chi-squared), Nakagami- m (and its discrete version Chi), exponential, Weibull, one-sided Gaussian, and Rayleigh ones. The Weibull distribution can be obtained from the α - μ distribution by setting $\mu = 1$. From the Weibull distribution, by setting $\alpha = 2$, the Rayleigh distribution results. Still from the Weibull distribution, the negative exponential distribution is obtained by setting $\alpha = 1$. The Nakagami- m distribution can be obtained from the α - μ distribution by setting $\alpha = 2$. From the Nakagami- m distribution, by setting $\mu = 1$, the Rayleigh distribution results. Still from the Nakagami- m distribution, the one-sided Gaussian distribution is obtained by setting $\mu = 1/2$.

Starting out from the α - η - κ - μ fading [13] and specializing its parameters as $\kappa \rightarrow 0$ and $\eta = 1$, it is possible to arrive at the corresponding α - μ phase-envelope joint PDF. From there, the in-phase-quadrature joint PDF can be found. On the other hand, as detailed in [13], the nonlinearity parameter does not affect the phase statistics, so that its phase PDF $f_\Theta(\theta)$ is that of Nakagami- m . Hence

$$f_\Theta(\theta) = \frac{\Gamma(\mu)}{2^\mu \Gamma(\mu)} \frac{|\sin(2\theta)|^{\mu-1}}{|\tan(\theta)|^{2\mu}}, \quad (3)$$

with $-\pi \leq \theta \leq \pi$ and $-1 \leq p \leq 1$ is a power (or clustering) imbalance parameter. This parameter is intrinsically connected to the multipath clustering effect as [5] (the definition

of the clustering imbalance parameter in this paper keeps that used in [5] and is different from that used in [13]; of course, one is related to the other as detailed in [13]). From [3], we know that the k th moment of the envelope-based α - μ random variable is given by $\mathbb{E}[R^k] = \hat{r}^k \Gamma(\mu + k/\alpha) / (\mu^{k/\alpha} \Gamma(\mu))$, which makes us able to set

$$\hat{r} = \sqrt{\frac{\mu^{2/\alpha} \Gamma(\mu) \mathbb{E}[R^2]}{\Gamma(\mu + 2/\alpha)}}. \quad (4)$$

Again, particularizing α - η - κ - μ fading model as required, the α - μ joint PDF $f_{R,\Theta}(r, \theta)$ is then found as

$$f_{R,\Theta}(r, \theta) = \frac{\alpha \mu^\mu \hat{r}^{\alpha\mu-1} \exp(-\mu(r^\alpha/\hat{r}^\alpha)) |\sin(2\theta)|^{\mu-1}}{2^\mu \hat{r}^{\alpha\mu} \Gamma(((1+p)/2)\mu) \Gamma(((1-p)/2)\mu) |\tan(\theta)|^{p\mu}}. \quad (5)$$

It can be seen from (5) that envelope and phase are independent variates. This is coherent with the complex Nakagami- m model [4, 5] in which the independence condition arose naturally out of the derivation of the model. As a particular case, the following are noted: (i) $p = 0$ denotes the power balance condition; (ii) $p = 1$ implies that the all signal power is concentrated in the in-phase component; (iii) $p = -1$ implies that all the signal power is concentrated in the quadrature component.

Given $f_{R,\Theta}(r, \theta)$, it is possible to find $f_{X,Y}(x, y)$ as $f_{X,Y}(x, y) = |J| f_{R,\Theta}(r, \theta)$, where $|J| = r$ is the Jacobian of the transformation $X = R \cos(\Theta)$ and $Y = R \sin(\Theta)$. Hence

$$f_{X,Y}(x, y) = \frac{\alpha \mu^\mu (x^2 + y^2)^{\mu(\alpha-2)/2} |x|^{\mu(1+p)-1} |y|^{\mu(1-p)-1}}{2^\mu \hat{r}^{\alpha\mu} \Gamma(((1+p)/2)\mu) \Gamma(((1-p)/2)\mu)} \times \exp\left(-\frac{\mu}{\hat{r}^\alpha} (x^2 + y^2)^{\alpha/2}\right) \quad (6)$$

with $-\infty < x < \infty$ and $-\infty < y < \infty$. The expression in (6) is general and, to the best of the authors' knowledge, new. Notice that, in general, the in-phase and quadrature components are not independent random variables. As a consequence, the joint PDF of X and Y can not be factorized as a product of the marginal PDFs. It is found that the random variables X and Y are independent if and only if $\alpha = 2$. In such a case

$$f_X(x)|_{\alpha=2} = \left(\frac{\mu}{\hat{r}^2}\right)^{((1+p)/2)\mu} \frac{|x|^{(1+p)\mu-1}}{\Gamma(((1+p)/2)\mu)} \exp\left(-\frac{\mu x^2}{\hat{r}^2}\right), \quad (7)$$

$$f_Y(y)|_{\alpha=2} = \left(\frac{\mu}{\hat{r}^2}\right)^{((1-p)/2)\mu} \frac{|y|^{(1-p)\mu-1}}{\Gamma(((1-p)/2)\mu)} \exp\left(-\frac{\mu y^2}{\hat{r}^2}\right). \quad (8)$$

Of course, $f_X(x)$ and $f_Y(y)$ given in (7) and (8) coincide, respectively, with those of (11) and (12) of [5].

The importance of (6) will become clear in Section 4 as it is used to compute the BER in a given subcarrier of the OFDM system. Another important aspect to be noticed about this joint PDF is that it does not provide the marginal PDFs of X and Y in a closed-form by integrating over y or x , respectively. However, in the next section, we present an efficient method for generating the complex α - μ without the knowledge of the marginal PDFs of X and Y .

3. Generating Complex α - μ Samples

This section presents the method used to generate the complex α - μ random variables for arbitrary values of its parameters. Bearing in mind that the nonlinearity parameter does not affect the phase statistics of the α - μ process, then its phase is given by that of the Nakagami- m process. Therefore, in order to generate α - μ complex variates, one can simply generate Nakagami- m complex variates and use the relation between the envelopes of the two processes. Assuming that Z_N and Z are, respectively, Nakagami- m and α - μ complex variates, then, $R = |Z| = |Z_N|^{2/\alpha}$ and $\Theta = \arg(Z) = \arg(Z_N)$. Now, from (7) and (8), it can be seen that the in-phase and quadrature components of the Nakagami- m have a Gamma PDF with symmetry around zero. Hence, the following can be written:

$$Z_N = S_X \sqrt{\frac{G_X}{\mu}} + j S_Y \sqrt{\frac{G_Y}{\mu}}, \quad (9)$$

where $G_X \sim \text{Gamma}((1+p)\mu/2, \hat{r}^2)$ and $G_Y \sim \text{Gamma}((1-p)\mu/2, \hat{r}^2)$ are independent Gamma random variables, μ accounts for the fading parameter, and $\hat{r}^2 = \mathbb{E}[|Z_N|^2]$. The multiplicative factors S_X and S_Y are independent discrete random variables assuming the values 1 and -1 with equal probabilities. Any mathematical software tool (e.g., Mathematica) that provides Gamma variate generator can be used here. Then to create the complex α - μ random variable, it suffices to make the transformation

$$Z = |Z_N|^{2/\alpha} \exp(j \arg(Z_N)). \quad (10)$$

It should be mentioned that the fact that the marginal PDFs for the in-phase and quadrature components of the α - μ process have not been obtained in closed-form did not affect the generation of the α - μ complex samples. The PDFs closed-form issue has been circumvented by generating complex samples for Nakagami- m variates, whose marginal PDFs are given in closed-form, and then applying the appropriate transformation of variables as in (10), from which the α - μ samples result.

When compared to other generation methods of complex Nakagami- m variates, such as the Acceptance-Rejection method used in [22], the proposed method here has a dramatically better efficiency.

In order to validate this new method, we show some plots comparing theoretical (solid lines) and simulated (symbols) curves. Each curve was generated using 5×10^5 samples with $\mu = 3$, where, without loss of generality, $\hat{r}^\alpha = 1$ was used. Figure 1 depicts various shapes of the α - μ envelope density.

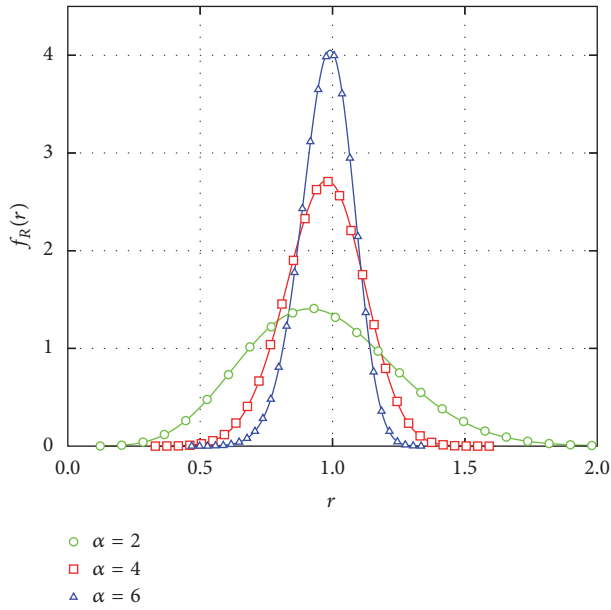


FIGURE 1: Empirical and theoretical α - μ envelope distribution with $\mu = 3$ and irrelevant p .

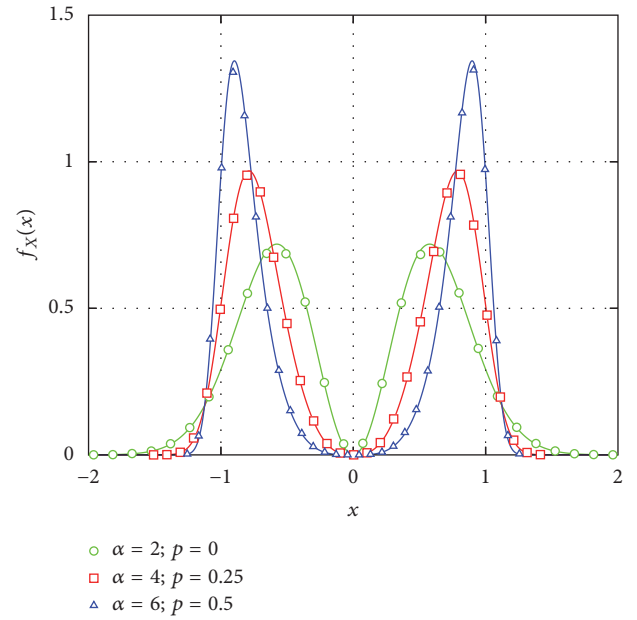


FIGURE 3: Empirical and theoretical $f_X(x)$ distribution with $\mu = 3$.

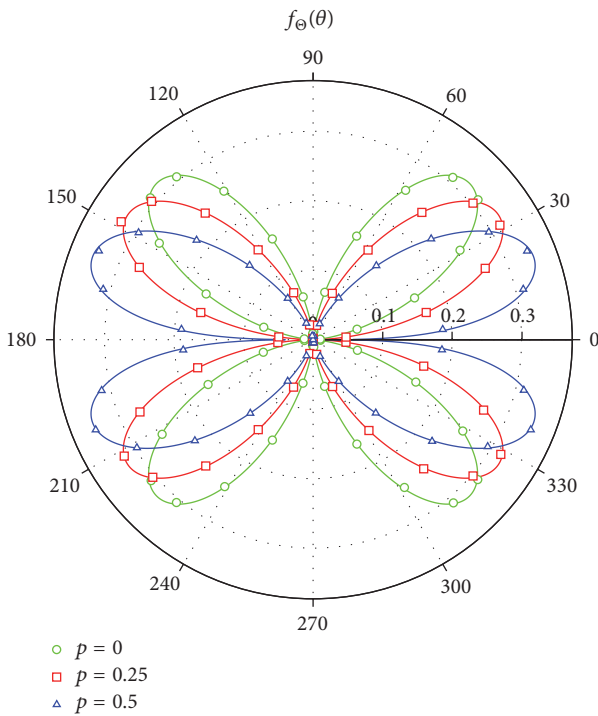


FIGURE 2: Empirical and theoretical α - μ phase distribution with $\mu = 3$ and irrelevant α .

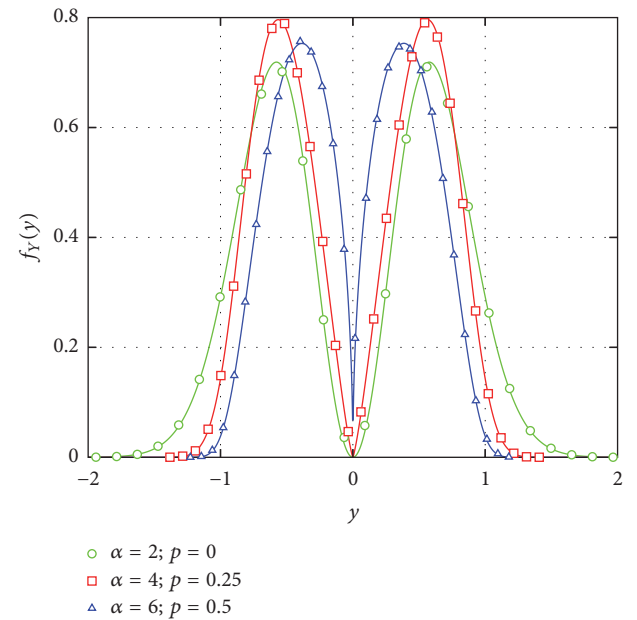


FIGURE 4: Empirical and theoretical $f_Y(y)$ distribution with $\mu = 3$.

Figure 2 shows the corresponding shapes of the α - μ phase PDF, plotted in polar coordinates.

In Figures 3 and 4, the PDFs of real and imaginary parts of the α - μ distribution are plotted, respectively. In all plots, we consider the parameter $\mu = 3$, and we vary the parameters α and p to verify the correctness of the proposed method to generate the α - μ complex density. We can notice the excellent

agreement between the simulation and the theoretical curves. It is worth mentioning that the theoretical curves of real and imaginary parts were calculated numerically, because they do not lend themselves into closed-form expressions.

4. OFDM System under the Complex α - μ Channel

4.1. Theoretical Expression for the BER. The OFDM system under investigation here is an idealized one, in which issues like channel estimation by training, cyclic prefix length,

equalization strategy, the presence of narrowband interference, impulse noise, and transceiver impairments, and others are overlooked. To accomplish the analysis of an OFDM system under the complex α - μ channel presented in this paper, a framework developed in [20] is used. In a simplified manner, the BER is computed combining three equations [20]:

- (1) The Characteristic Function:

$$\Phi_\ell(u, v) = \mathbb{E} \left[e^{-jX_\ell \{u \cos(2\pi(n/N)\ell) + v \sin(2\pi(n/N)\ell)\}} \right. \\ \left. \times e^{-jY_\ell \{u \sin(2\pi(n/N)\ell) - v \cos(2\pi(n/N)\ell)\}} \right], \quad (11)$$

where (i) the subscript ℓ denotes ℓ th path with $\ell = 0, 1, 2, \dots, L - 1$ in which L is the total number of multipath rays; (ii) X_ℓ and Y_ℓ are the real and imaginary part of the complex α - μ channel at the ℓ th path, respectively; (iii) N is the total number of subcarriers with $n = 0, 1, 2, \dots, N - 1$ being the index of the subcarrier.

- (2) The Moment Generating Function:

$$\mathcal{M}(z) = \mathbb{E} \left[e^{-z|H_n|^2} \right] \\ = \frac{1}{\pi} \int_{-\infty}^{\infty} \int_{-\infty}^{\infty} e^{-(u^2+v^2)} \\ \times \prod_{\ell=0}^{L-1} \Phi_\ell(2\sqrt{z}u, 2\sqrt{z}v) du dv, \quad (12)$$

where $H_n = \sum_{\ell=0}^{L-1} Z_\ell e^{-j2\pi n\ell/N}$ is the frequency-domain channel impulse response and Z_ℓ , $\ell = 0, 1, 2, \dots, L - 1$, are independent complex α - μ random variables given by (1) with the appropriate subscript.

- (3) The BER of BPSK ((13) is slightly different from that of [20, eqn. (24)] due to typo found there):

$$P_b = \frac{1}{\pi} \int_0^{\pi/2} \mathcal{M}^D \left(\frac{\text{SNR}}{2 \sin^2(\theta)} \right) d\theta, \quad (13)$$

where D is the order of diversity of the maximum ratio combiner (MRC) and SNR is the signal-to-noise ratio.

For the α - μ channel, however, (11) has to be computed numerically as

$$\Phi_\ell(u, v) \\ = \int_{-\infty}^{\infty} \int_{-\infty}^{\infty} f_{X_\ell, Y_\ell}(x_\ell, y_\ell) e^{-j(x_\ell w_{x_\ell} + y_\ell w_{y_\ell})} dx_\ell dy_\ell, \quad (14)$$

where $f_{X_\ell, Y_\ell}(x_\ell, y_\ell)$ is the joint PDF of the in-phase and quadrature components of the channel at the ℓ th path given by (6), $w_{x_\ell} = \{u \cos(2\pi(n/N)\ell) + v \sin(2\pi(n/N)\ell)\}$, and $w_{y_\ell} = \{u \sin(2\pi(n/N)\ell) - v \cos(2\pi(n/N)\ell)\}$.

It is worth mentioning that (13) can be easily generalized to other modulations schemes such as the M -PSK [1, eq. (5.67)] and M -QAM modulations [1, eq. (8.110)].

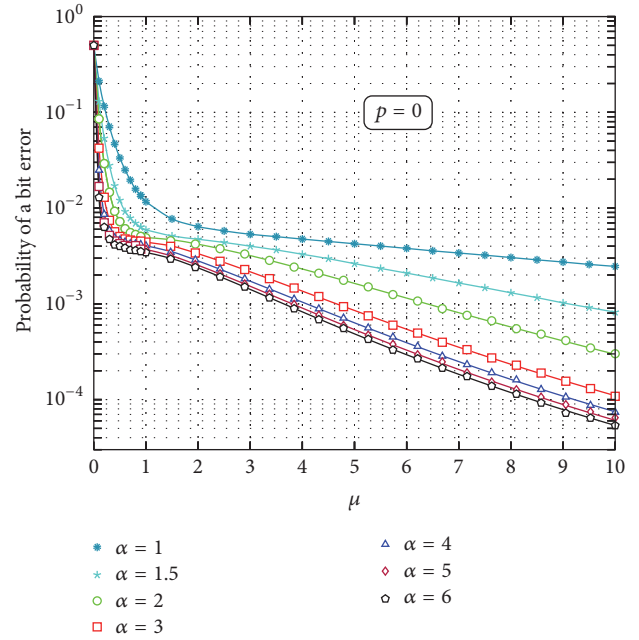


FIGURE 5: Average BER against the fading parameter μ under α - μ fading channel with SNR = 20 dB, $L = 3$, and $p = 0$.

4.2. Numerical Examples. This section assesses the performance of the BPSK-based OFDM system in terms of BER concerning the influence of the main system parameters. All experiments depicted here consider $n = N/2$, as also used in [20], and $\sum_{\ell=0}^{L-1} \mathbb{E}[R_\ell^2] = 1$. The theoretical results are calculated numerically using (13). Independent simulations have been performed so as to validate the theoretical expressions. MATLAB was used to implement the code according to the models described throughout the paper. For each point we generate at least 2×10^7 samples using the Monte Carlo approach.

In Figure 5, the theoretical probability error of a bit (solid lines) and the estimated through simulation bit error rate (symbols) are plotted against the parameter μ . The nonlinearity parameter α varies as $\{1; 1.5; 2; 3; 4; 5; 6\}$ and $L = 3$ for a fixed value of $p = 0$ (balanced scenario). Note the excellent agreement between theoretical and simulated curves showing the usefulness and correctness of the analytical procedure. It is worth mentioning that for $\alpha = 2$, that is, the Nakagami- m case, the result is the same as the one obtained in [20], as expected. It is possible to conclude that the increase of the clustering parameter μ diminishes the BER for a fixed value of α . This is an expected result, since the parameter μ accounts for the number of multipath clusters. In other words, the higher the value of μ is, the less severe the fading is. Hence the performance in terms of probability of error is improved. In the same way, the increase of the parameter α also improves the BER performance. Of course, the higher the values of α are, the more deterministic the channel is and, therefore, the less vulnerable to variation the channel is.

In order to assess the impact of the phase parameter, Figure 6 depicts the same set of curves of Figure 5 but now with $p = 1/3$, corresponding to a case in which the power

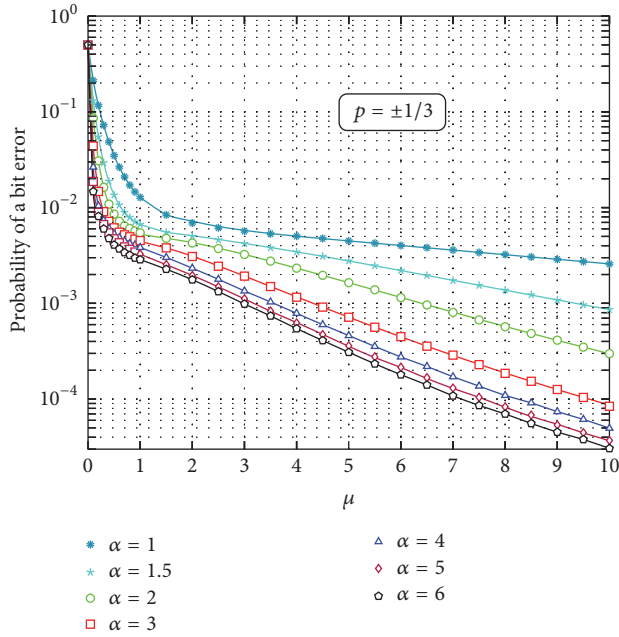


FIGURE 6: Average BER against the fading parameter μ under α - μ fading channel with SNR = 20 dB, $L = 3$, and $p = 1/3$.

(or the number of clusters) of the in-phase component is the double as that of the quadrature component. In addition to the conclusions already drawn from Figure 5, by comparing the curves for the same nonlinearity parameter α , for $\alpha > 2$, the increase in the phase parameter leads to a lower BER. Furthermore, the performance obtained for $p = 0$ (balanced) and $p = 1/3$ (imbalanced) scenarios improves as α increases. However, for $\alpha \leq 2$ the performance under the variation of the phase parameter p is practically the same for any value of α . This means that the power imbalance between in-phase and quadrature components has very little effect on the system performance in terms of BER. Moreover, the impact of phase imbalance on the system performance is greater for high values of α .

With the objective of clarifying even more the impact of phase imbalance, Figure 7 depicts the same set of curves of Figure 5 but now against the absolute value of the parameter p for fixed $\mu = 3$. Firstly, all the previous conclusions are corroborated by this new graph. Additionally, for $\alpha \leq 2$ the impact of phase imbalance on the system performance is greater for high values of $|p|$ increasing slightly the BER. In contrast, for $\alpha > 2$, for high value of the power imbalance between in-phase and quadrature components, the effect on the system performance in terms of BER is higher. It is desirable to have an intuitive explanation for such a behavior. Unfortunately, the problem is rather intricate and nonlinear, so further investigation is due.

In Figure 8, the BER is plotted against the SNR for fixed $\mu = 3$ and $L = 3$ using the balanced ($p = 0$) and imbalanced ($p = 1/3$) scenarios for single ($D = 1$) and dual ($D = 2$) channel diversity reception. In this figure the influence of α and the diversity parameter D is clearly noticed. As expected,

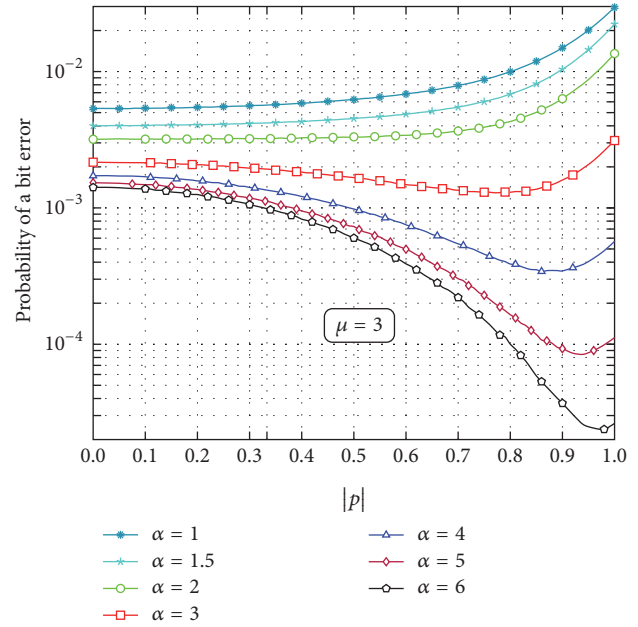


FIGURE 7: Average BER against the phase parameter p under α - μ fading channel with SNR = 20 dB, $L = 3$, and $\mu = 3$.

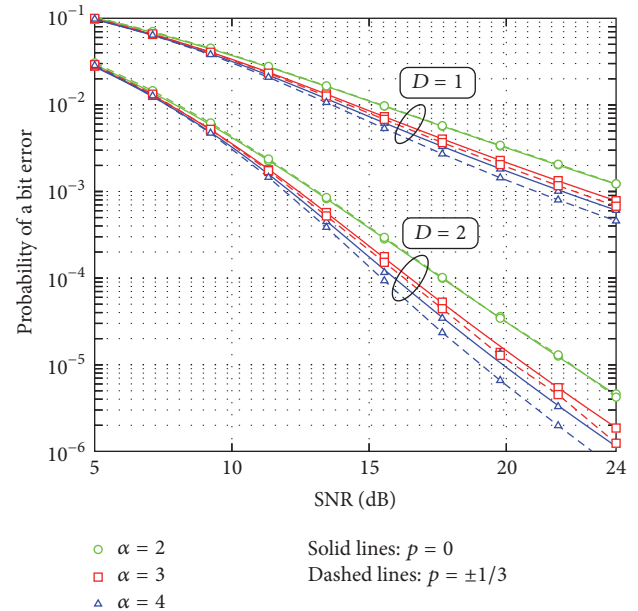


FIGURE 8: Average BER against SNR for single and dual channel diversity reception with $\mu = 3$ and $L = 3$ for balanced and imbalanced scenarios.

for higher diversity system order, the performance in terms of probability of error is improved. The difference between the BER of the single and dual channel diversity reception increases at higher SNR values. Again, phase imbalance impacts positively on the system performance, especially for high values of SNR.

5. Conclusions

In this paper, a model for the complex α - μ channel was presented. From such a model, the joint probability density function of in-phase and quadrature components was found. This was then used within an analytical framework to assess the bit error rate performance of an OFDM system. As a by-product of the main results, an efficient, simple, and general complex α - μ variates generator was proposed. It was found that an increase of the value of the nonlinearity parameter as well as of the number of clusters improves the system performance in terms of its bit error rate. In the same way, the imbalance of power (or clustering) between in-phase and quadrature components also has a positive impact on such performance.

Conflicts of Interest

The authors declare that there are no conflicts of interest regarding the publication of this paper.

Acknowledgments

This work was partially supported by Finep, with resources from Funttel, Grant no. 01.14.0231.00, under the Radio-communication Reference Center (*Centro de Referência em Radiocomunicações*, CRR) project of the National Institute of Telecommunications (*Instituto Nacional de Telecomunicações*, Inatel), Brazil.

References

- [1] M. K. Simon and M. Alouini, *Digital Communication Over Fading Channels*, John Wiley & Sons, Inc., New York, USA, 2000.
- [2] P. M. Shankar, "Statistical models for fading and shadowed fading channels in wireless systems: A pedagogical perspective," *Wireless Personal Communications*, vol. 60, no. 2, pp. 191–213, 2011.
- [3] M. D. Yacoub, "The α - μ distribution: a physical fading model for the Stacy distribution," *IEEE Transactions on Vehicular Technology*, vol. 56, no. 1, pp. 27–34, 2007.
- [4] M. D. Yacoub, G. Fraidenraich, and J. C. S. Santos Filho, "Nakagami-m phase-envelope joint distribution," *Electronics Letters*, vol. 41, no. 5, pp. 259–261, 2005.
- [5] M. D. Yacoub, "Nakagami-m phase-envelope joint distribution: A new model," *IEEE Transactions on Vehicular Technology*, vol. 59, no. 3, pp. 1552–1557, 2010.
- [6] I. B. G. Porto, M. D. Yacoub, J. C. S. Santos Filho, S. L. Cotton, and W. G. Scanlon, "Nakagami-m phase model: Further results and validation," *IEEE Wireless Communications Letters*, vol. 2, no. 5, pp. 523–526, 2013.
- [7] L. Rayleigh, "On the resultant of a large number of vibrations of same pitch and of arbitrary phase," *Philosophical Magazine*, vol. 10, no. 60, pp. 73–78, 1880.
- [8] R. S. Hoyt, "Probability functions for the modulus and angle of the normal complex variate," *The Bell System Technical Journal*, vol. 26, pp. 318–359, 1947.
- [9] S. O. Rice, "Statistical Properties of Random Noise Currents," in *Statistical Properties of Random Noise Currents*, N. Wax, Ed., NY, USA: Dover, 1954.
- [10] *Statistical Methods in Radio Wave Propagation*, Elsevier, 1960.
- [11] W. Weibull, "A statistical distribution function of wide applicability," *Journal of Applied Mechanics*, vol. 18, pp. 293–297, 1951.
- [12] J. Reig, M.-T. Martínez-Inglés, L. Rubio, V.-M. Rodrigo-Peñarrocha, and J. Molina-García-Pardo, "Fading evaluation in the 60 GHz band in line-of-sight conditions," *International Journal of Antennas and Propagation*, vol. 2014, Article ID 984102, 12 pages, 2014.
- [13] M. D. Yacoub, "The α - η - κ - μ fading model," *IEEE Transactions on Antennas and Propagation*, vol. 64, no. 8, pp. 3597–3610, 2016.
- [14] G. Berardinelli, K. I. Pedersen, T. B. Sørensen, and P. Mogensen, "Generalized DFT-Spread-OFDM as 5G Waveform," *IEEE Communications Magazine*, vol. 54, no. 11, pp. 99–105, 2016.
- [15] G. Berardinelli, F. M. L. Tavares, T. B. Sørensen, P. Mogensen, and K. Pajukoski, "Zero-tail DFT-spread-OFDM signals," in *Proceedings of the 2013 IEEE Globecom Workshops, GC Wkshps 2013*, pp. 229–234, usa, December 2013.
- [16] A. Sahin, R. Yang, M. Ghosh, and R. L. Olesen, "An improved unique word DFT-spread OFDM scheme for 5G systems," in *Proceedings of the IEEE Globecom Workshops, GC Wkshps 2015*, USA, December 2015.
- [17] N. Michailow, M. Matthe, I. S. Gaspar et al., "Generalized frequency division multiplexing for 5th generation cellular networks," *IEEE Transactions on Communications*, vol. 62, no. 9, pp. 3045–3061, 2014.
- [18] B. Farhang-Boroujeny and H. Moradi, "OFDM Inspired Waveforms for 5G," *IEEE Communications Surveys and Tutorials*, vol. 18, no. 4, pp. 2474–2492, 2016.
- [19] X. Zhang, L. Chen, J. Qiu, and J. Abdoli, "On the Waveform for 5G," *IEEE Communications Magazine*, vol. 54, no. 11, pp. 74–80, 2016.
- [20] K. A. Hamdi, "Analysis of OFDM over Nakagami-m fading with nonuniform phase distributions," *IEEE Transactions on Wireless Communications*, vol. 11, no. 2, pp. 488–492, 2012.
- [21] M. Abramowitz and I. A. Stegun, *Handbook of Mathematical Functions*, 1965.
- [22] R. A. A. de Souza, R. Cogliatti, and M. D. Yacoub, "Efficient acceptance-rejection method for Nakagami-m complex samples," *IEEE Wireless Communications Letters*, vol. 3, no. 1, pp. 94–96, 2014.

Research Article

Performance Analysis of 5G Transmission over Fading Channels with Random IG Distributed LOS Components

Dejan Jaksic,¹ Risto Bojovic,² Petar Spalevic,¹ Dusan Stefanovic,³ and Slavisa Trajkovic⁴

¹Faculty of Technical Science, Singidunum University, Belgrade, Serbia

²Faculty of Technical Science, University of Pristina, Kosovska Mitrovica, Serbia

³High Technical College, University of Niš, Niš, Serbia

⁴Faculty of Economics, University of Pristina, Kosovska Mitrovica, Serbia

Correspondence should be addressed to Petar Spalevic; petarspalevic@yahoo.com

Received 6 January 2017; Accepted 21 May 2017; Published 13 July 2017

Academic Editor: Rausley A. A. De Souza

Copyright © 2017 Dejan Jaksic et al. This is an open access article distributed under the Creative Commons Attribution License, which permits unrestricted use, distribution, and reproduction in any medium, provided the original work is properly cited.

Mathematical modelling of the behavior of the radio propagation at mmWave bands is crucial to the development of transmission and reception algorithms of new 5G systems. In this study we will model 5G propagation in nondeterministic line-of-sight (LOS) conditions, when the random nature of LOS component ratio will be observed as Inverse Gamma (IG) distributed process. Closed-form expressions will be presented for the probability density function (PDF) and cumulative distribution function (CDF) of such random process. Further, closed-form expressions will be provided for important performance measures such as level crossing rate (LCR) and average fade duration (AFD). Capitalizing on proposed expressions, LCR and AFD will be discussed in the function of transmission parameters.

1. Introduction

Keeping pace with the insatiable demand of wireless data transmission growth has resulted in occurrence of novel 5G technologies that can offer significant increase in cellular capacity and overcoming of the wireless spectrum shortage [1, 2]. Consequently, research on modelling channel propagation characteristics for wireless 5G networks in urban environments at mmWave bands carrier frequencies has been intense recently [3–6].

Stochastic channel models for mmWave communications in both indoor and outdoor environments have been mostly characterized with a Rician distribution in line-of-sight (LOS) environments where a dominant path is present and with Rayleigh distribution for NLOS environment scenarios [7]. In [7], it has been shown that the voltage path amplitudes are following a Rician distribution, with K -factor ranging within defined set of values for observed (LOS) and (NLOS) conditions in vertical-to-vertical (V-V) copolarized antenna scenario and corresponding set of values for observed (LOS) and (NLOS) conditions vertical-to-horizontal (V-H) cross-polarized antenna scenario.

However, despite the fact shown in [7] that Rician distribution provides the best fit to the measurement data, results of [7] imply that conventional fading models often fall short in accurately modelling the random fluctuations of 5G wireless channel signal. In [8], it has been concluded that, for accurate 5G systems channel modelling, proposed model should ensure that the channel LOS and NLOS states, the second-order statistics of the channel, and the channel realizations should change smoothly in the function of time, antenna position, and/or frequency. Ricean K -factor has already been observed as a random variable with determined PDF over the distance in 5G communication in [9]. The Ricean K -factor, ratio of powers dominant and scatter components, has been already treated as log-normal random process in [10], but for the narrow-band fixed wireless channels. In [11] it has been shown that log-normal random process, in the mathematical form which is hard for analytically tracking wireless performances, could be efficiently approximated with slowly varying Inverse Gamma (IG) distributed random process.

In this paper we will obtain novel characterization of propagation in LOS conditions, by observing Ricean K -factor

as Inverse Gamma (IG) distributed random process. Standard first-order statistical characterization for this model will be determined; that is, probability density function (PDF) and cumulative distribution function (CDF) of random envelope process will be obtained in closed representation that is convenient to handle both analytically and numerically. Further, important second-order statistical measures as level crossing rate (LCR) and average fade duration (AFD) will be presented in closed form. Capitalizing on their performances of proposed channel will be discussed in function of the system parameters.

2. System Model

Rician distributed random process with conditional PDF, conditioned over Rician K -factor, which is observed as random variable, can be expressed as [12]

$$p_{x|K}(x|K) = \frac{2(1+K)x}{\Omega} \exp\left(-K - \frac{(1+K)x^2}{\Omega}\right) \cdot I_0\left(2x\sqrt{\frac{K(K+1)}{\Omega}}\right), \quad (1)$$

where $I_0(x)$ denotes the modified Bessel function of the first kind and zero order [12, Eq. 8.445], and Ω is defined as $\Omega = E(x^2)$, being average signal power.

In [11, 13], it has been shown that the PDF of the Inverse Gamma random variable can be expressed as

$$p_K(K) = \frac{\kappa^c}{K^{c-1}\Gamma(c)} \exp\left(-\frac{\kappa}{K}\right), \quad (2)$$

where $\Gamma(x)$ is the Gamma function [12, Eq. 8.310.1], $c > 0$ is the shape parameter, and $\kappa > 0$ is scale parameter.

Now, novel random process envelope PDF can now be obtained by averaging over IG distributed process of K -factor change as

$$p_x(x) = \int_0^\infty dK p_{x|K}(x|K) p_K(K). \quad (3)$$

Now after substituting (2) into (3), by performing some mathematical transformations with respect to [12, Equation 3.471.9], we obtain closed-form expression:

$$p_x(x) = \sum_{p=0}^{\infty} \sum_{n=0}^{p+1} \binom{p+1}{n} \frac{x^{2p+1} \kappa^c}{\Omega^{p+1} \Gamma(p+1) \Gamma(c) p!} \exp\left(-\frac{x^2}{\Omega}\right) \times 2 \left(\frac{\kappa \Omega}{\Omega + x^2}\right)^{(p-n+c)/2} K_{p-n+c} \left(2\sqrt{\frac{\kappa(\Omega + x^2)}{\Omega}}\right), \quad (4)$$

where $K_\nu(x)$ denotes the modified Bessel function of the second kind and ν th order. Infinite-series from above rapidly converge with only 10–15 terms needed to be summed in each sum in order to achieve accuracy at 5th significant digit.

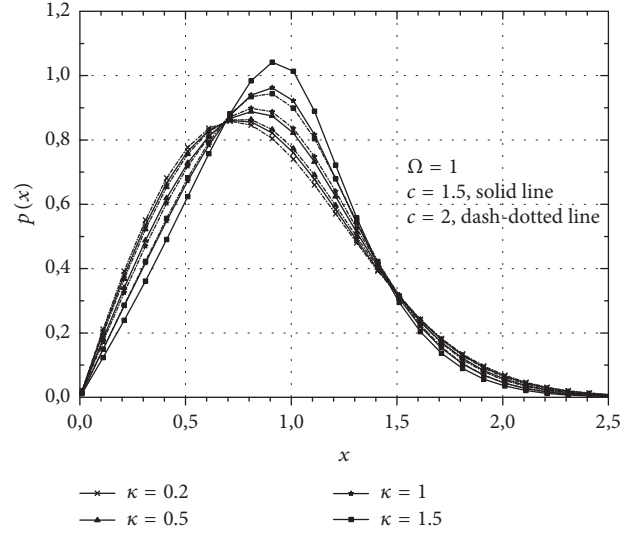


FIGURE 1: PDF of process for various values of system parameters.

In Figure 1, PDF of process is shown for some combination of system parameter values.

Now, by taking into account IG modelled randomness of LOS component, corresponding CDF could be obtained as

$$F_x(x) = \int_0^\infty dx p_x(x) = \int_0^\infty dx \int_0^\infty dK p_{x|K}(x|K) p_K(K). \quad (5)$$

After changing integration order, previous relation reduces to

$$F_x(x) = \int_0^\infty dK \sum_{p=0}^{\infty} \frac{K^p \exp(-K)}{\Gamma(p+1) p!} \gamma\left(p+1, \frac{(1+K)x}{\Omega}\right) \cdot p_K(K), \quad (6)$$

where $\gamma(a, x)$ stands for the incomplete Gamma function [12, Equation 8.443]. Further, with respect to [12, Equation 3.471.9], we can obtain closed-form expression:

$$F_x(x) = \sum_{p=0}^{\infty} \sum_{n=0}^{\infty} \sum_{s=0}^{p+n+1} \binom{p+n+1}{s} \frac{x^{p+n+1} \kappa^c}{\Omega^{p+n+1} \Gamma(p+n+2) \Gamma(c) p!} \exp\left(-\frac{x}{\Omega}\right) \times 2 \left(\frac{\kappa \Omega}{\Omega + x}\right)^{(p+s-c)/2} K_{p+s-c} \left(2\sqrt{\frac{\kappa(\Omega + x)}{\Omega}}\right). \quad (7)$$

Similarly, as in (4), infinite-series from above rapidly converge with only 10–15 terms needed to be summed in each sum in order to achieve accuracy at 5th significant digit.

The average LCR at the determined threshold x is defined as the rate at which the envelope ratio crosses the threshold x

in a positive or a negative direction and is analytically defined by [14]

$$N_x(x) = \int_0^\infty \dot{x} p_{\dot{x}x}(\dot{x}, x) d\dot{x}, \quad (8)$$

where joint probability density function (JPDF) of the observed random process, x , and its derivative with respect to time, \dot{x} , denoted by $p_{\dot{x}x}(\dot{x}, x)$, can be evaluated as

$$p_{\dot{x}x}(\dot{x}, x) = \int_0^\infty dK p_{\dot{x}x|K}(\dot{x}, x | K) p_K(K), \quad (9)$$

with $p_{\dot{x}x|K}(\dot{x}, x | K)$ being JPDF conditioned over random LOS component which is IG distributed.

Conditioned JPDF of the observed random process and its derivative with respect to time can be further presented as

$$p_{\dot{x}x|K}(\dot{x}, x | K) = p_{\dot{x}|x,K}(\dot{x} | x, K) p_{x|K}(x | K), \quad (10)$$

where

$$\begin{aligned} p_{\dot{x}|x,K}(\dot{x} | x, K) &= \frac{1}{\sqrt{2\pi}\sigma_x} \exp\left(-\frac{\dot{x}^2}{2\sigma_x^2}\right) \\ &= \frac{1}{\sqrt{2\pi}(\pi f_d \sqrt{\Omega/(K+1)})} \\ &\cdot \exp\left(-\frac{\dot{x}^2}{2\pi^2 f_d^2 (\Omega/(K+1))}\right) \end{aligned} \quad (11)$$

since $\sigma_x^2 = \pi^2 f_d^2 (\Omega/(K+1))$ for Rician fading channels and f_d is the maximum Doppler frequency [15].

After substituting (9), (10), and (11) into (8), expression for average LCR can be presented in the form of

$$\begin{aligned} N_x(x) &= \int_0^\infty \dot{x} d\dot{x} \int_0^\infty dK \\ &\cdot \frac{\exp\left(-\dot{x}^2/2\pi^2 f_d^2 (\Omega/(K+1))\right)}{\sqrt{2\pi}(\pi f_d \sqrt{\Omega/(K+1)})} \\ &\cdot p_{x|K}(x | K) p_K(K) \end{aligned} \quad (12)$$

which after changing order of integration reduces to

$$\begin{aligned} N_x(x) &= \int_0^\infty dK \frac{(\pi f_d \sqrt{\Omega/(K+1)})}{\sqrt{2\pi}} p_{x|K}(x | K) p_K(K). \end{aligned} \quad (13)$$

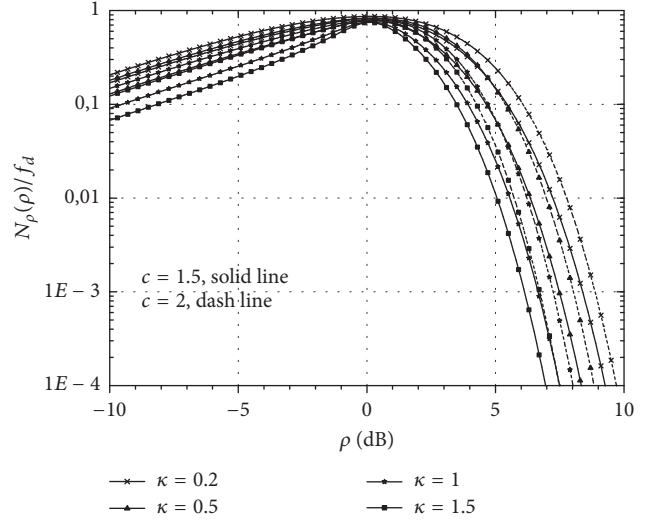


FIGURE 2: Normalized LCR for observed fading channel.

Now by substituting (1) and (2) into (13) with respect to [12, Equation 3.471.9], we can obtain closed-form LCR expression as

$$\begin{aligned} \frac{N_x(x)}{f_d} &= \sum_{p=0}^{\infty} \sum_{n=0}^{p+1} \binom{p+\frac{1}{2}}{n} \\ &\cdot \frac{2\sqrt{2}\sqrt{\pi}x^{2p+1}\kappa^c}{\Omega^{p+1/2}\Gamma(p+1)\Gamma(c)p!} \exp\left(-\frac{x^2}{\Omega}\right) \\ &\times \left(\frac{\kappa\Omega}{\Omega+x^2}\right)^{(p-n+c)/2} K_{p-n+c}\left(2\sqrt{\frac{\kappa(\Omega+x^2)}{\Omega}}\right). \end{aligned} \quad (14)$$

Infinite-series from above rapidly converge with only 10–15 terms needed to be summed in each sum in order to achieve accuracy at 5th significant digit.

3. Numerical Results

After introducing ρ as $\rho = x^2/\Omega$, LCR expression can be given in the form of

$$\begin{aligned} \frac{N_\rho(\rho)}{f_d} &= \sum_{p=0}^{\infty} \sum_{n=0}^{p+1} \binom{p+\frac{1}{2}}{n} \frac{2\sqrt{2}\sqrt{\pi}\rho^{p+1/2}\kappa^c}{\Gamma(p+1)\Gamma(c)p!} \exp(-\rho) \\ &\times \left(\frac{\kappa}{1+\rho}\right)^{(p-n+c)/2} K_{p-n+c}\left(2\sqrt{\kappa(1+\rho)}\right). \end{aligned} \quad (15)$$

Figure 2 illustrates the LCR, normalized to f_d in the function of parameters κ and c . As expected, the presence of a stronger LOS component generally causes lower LCR values, while higher values of severity parameters c provide smaller LCR values.

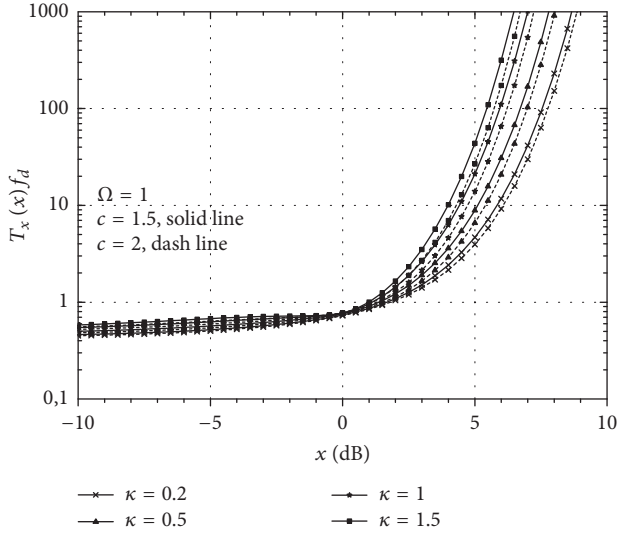


FIGURE 3: Normalized AFD for observed fading channel.

Average time during (AFD) defines time in which the envelope ratio remains below the specified threshold x after crossing that level in a downward direction [14]. AFD can be determined as

$$T_x(x) = \frac{F_x(x)}{N_x(x)}. \quad (16)$$

After substituting (14) and (7) into (16) AFD of observed process can be efficiently evaluated. In Figure 3, AFD values are presented, normalized to f_d in the function of parameters κ and c . As expected, higher values of severity parameters c provide smaller AFD values.

4. Conclusion

Change of Rician K -factor as random IG process in LOS conditioned 5G wireless communications has been considered in this paper, instead of considering Rician K -factor as a deterministic variable with constant value defined by 5G communication system properties. Rapidly converging closed-form expressions have been derived for the PDF and CDF of observed propagation signal. Further, based on these expressions, LCR and AFD have been efficiently evaluated and analyzed for observed case in the function of system parameters.

Conflicts of Interest

The authors declare that there are no conflicts of interest regarding the publication of this paper.

Acknowledgments

This research was partly funded by Project TR 32023 of Ministry of Science, Serbia.

References

- [1] T. Rappaport, S. Sun, R. Mayzus et al., "Millimeter wave mobile communications for 5G cellular: it will work!," *IEEE Access*, vol. 1, pp. 335–349, 2013.
- [2] T. S. Rappaport, G. R. MacCartney, M. K. Samimi, and S. Sun, "Wideband millimeter-wave propagation measurements and channel models for future wireless communication system design," *IEEE Transactions on Communications*, vol. 63, no. 9, pp. 3029–3056, 2015.
- [3] M. R. Akdeniz, Y. Liu, M. K. Samimi et al., "Millimeter wave channel modeling and cellular capacity evaluation," *IEEE Journal on Selected Areas in Communications*, vol. 32, no. 6, pp. 1164–1179, 2014.
- [4] S. Hur, S. Baek, B. Kim et al., "Proposal on millimeter-wave channel modeling for 5G cellular system," *IEEE Journal on Selected Topics in Signal Processing*, vol. 10, no. 3, pp. 454–469, 2016.
- [5] J. Kyrolainen, P. Kyosti, J. Meinila et al., "Channel modelling for the fifth generation mobile communications," in *Proceedings of the 8th European Conference on Antennas and Propagation (EuCAP '14)*, pp. 219–223, IEEE, The Hague, The Netherlands, April 2014.
- [6] J. M. Romero-Jerez, F. J. Lopez-Martinez, J. F. Paris, and A. Goldsmith, "The fluctuating two-ray fading model for mmWave communications," in *Proceedings of the 2016 IEEE Globecom Workshops (GC Wkshps)*, pp. 1–6, Washington, DC, USA, December 2016.
- [7] M. K. Samimi, G. R. Maccartney, S. Sun, and T. S. Rappaport, "28 GHz millimeter-wave ultrawideband small-scale fading models in wireless channels," in *Proceedings of the 83rd IEEE Vehicular Technology Conference, VTC Spring 2016*, May 2016.
- [8] K. Haneda, L. Tan, Y. Zheng et al., "5G 3GPP-like channel models for outdoor urban microcellular and macrocellular environments," in *Proceedings of the 2016 IEEE 83rd Vehicular Technology Conference (VTC Spring)*, pp. 1–7, Nanjing, China, May 2016.
- [9] A. Rauch, J. Lianghai, A. Klein, and H. D. Schotten, "Fast algorithm for radio propagation modeling in realistic 3-D urban environment," *Advances in Radio Science*, vol. 13, pp. 169–173, 2015.
- [10] L. J. Greenstein, S. S. Ghassemzadeh, V. Erceg, and D. G. Michelson, "Rician κ -factors in narrow-band fixed wireless channels: theory, experiments, and statistical models," *IEEE Transactions on Vehicular Technology*, vol. 58, no. 8, pp. 4000–4012, 2009.
- [11] S. K. Yoo, P. C. Sofotasios, S. L. Cotton, M. Matthaiou, M. Valkama, and G. K. Karagiannidis, "The Kappa - mu/inverse gamma composite fading model," in *Proceedings of the 2015 IEEE 26th Annual International Symposium on Personal, Indoor, and Mobile Radio Communications (PIMRC)*, pp. 166–170, Hong Kong, China, August 2015.
- [12] I. Gradshteyn and I. Ryzhik, *Tables of Integrals, Series, and Products*, Academic Press, New York, NY, USA, 1980.
- [13] V. Witkovský, "Computing the distribution of a linear combination of inverted gamma variables," *Kybernetika*, vol. 37, no. 1, pp. 79–90, 2001.
- [14] X. Dong and N. C. Beaulieu, "Average level crossing rate and average fade duration of selection diversity," *IEEE Communications Letters*, vol. 5, no. 10, pp. 396–398, 2001.
- [15] Z. Hadzi-Velkov, "Level crossing rate and average fade duration of selection diversity with Rician-faded cochannel interferers," *IEEE Communications Letters*, vol. 10, no. 9, pp. 649–651, 2006.

Research Article

60 GHz Modular Antenna Array Link Budget Estimation with WiGig Baseband and Millimeter-Wave Specific Attenuation

Joongheon Kim,¹ Liang Xian,² and Ali S. Sadri²

¹Chung-Ang University, Seoul, Republic of Korea

²mmWave Standards and Advanced Technology (mSAT) Team, Intel Corporation, San Diego, CA, USA

Correspondence should be addressed to Joongheon Kim; joongheon@gmail.com

Received 10 December 2016; Accepted 14 May 2017; Published 15 June 2017

Academic Editor: María Elena de Cos Gómez

Copyright © 2017 Joongheon Kim et al. This is an open access article distributed under the Creative Commons Attribution License, which permits unrestricted use, distribution, and reproduction in any medium, provided the original work is properly cited.

This paper provides practical 60 GHz link budget estimation results with IEEE 802.11ad standard-defined parameters and 60 GHz specific attenuation factors. In addition, the parameters from currently developing modular antenna arrays (MAAs) are adopted for estimating the actual link budgets of our 60 GHz integrated MAA platforms. Based on the practical link budget analysis results, we can estimate fundamental limits in terms of achievable data rates over 60 GHz millimeter-wave wireless links.

1. Introduction

Among the various requirements for next-generation wireless systems (for both cellular and access), achieving multigigabit/s data rates is one of key requirements, and millimeter-wave (mmWave) wireless technologies have been mainly considered to achieve this goal where the considering mmWave frequencies are 28 GHz [1], 38 GHz (or 39 GHz) [2, 3], 60 GHz [4], and 73 GHz [5] bands. The use of mmWave bands for next-generation wireless systems could offer ultra-wideband spectrum availability and increased channel capacity. All these benefits come at the expense of potentially greater system complexity particularly in terms of radio frequency (RF) front end and antenna design, but the recent advancements around mmWave wireless systems development have produced cost effective solutions that can be leveraged to overcome these challenges. Among the potential candidates in mmWave bands for future wireless systems, 60 GHz frequency is considered here because it is only one mmWave band which has its own standardized protocol, that is, the Wireless Gigabit Alliance (WiGig) standard which is equivalent to IEEE 802.11ad.

In this paper, practical link budget estimation is performed based on WiGig/IEEE 802.11ad standard-defined modulation and coding scheme (MCS) modes and 60 GHz mmWave specific path-loss and auxiliary attenuation factors.

The considered systems parameters for this link budget estimation are obtained from real-world hardware prototype which is now actively conducting research for next-generation mmWave mesh backhaul networks in industry.

The remainder of this paper is organized as follows: Section 2 introduces our real-world prototype for 60 GHz mmWave backhaul networks. Section 3 presents the details of link budget estimation procedure. Section 4 shows link budget estimation results and Section 5 concludes this paper.

2. 60 GHz Integrated MAA Platform

Traditional antenna system architectures are generally not capable of combining wide-angles with high directionality. To achieve the necessary wide directionality, the phased antenna arrays should consist of a large number of antenna elements. Nowadays, the phased antenna array architectures are widely used for mass production and intended for personal mobile devices comprising a single module containing RF integrated circuits (RFIC) chip that includes controlled analogue phase shifters capable of providing several phase shifting levels. The antenna elements are connected to the RFIC via feeding lines. According to the loss on the feeding lines, this approach allows implementing antenna arrays with limited dimensions of up to 8-by-8, thus achieving gains of about 15–20 dB.

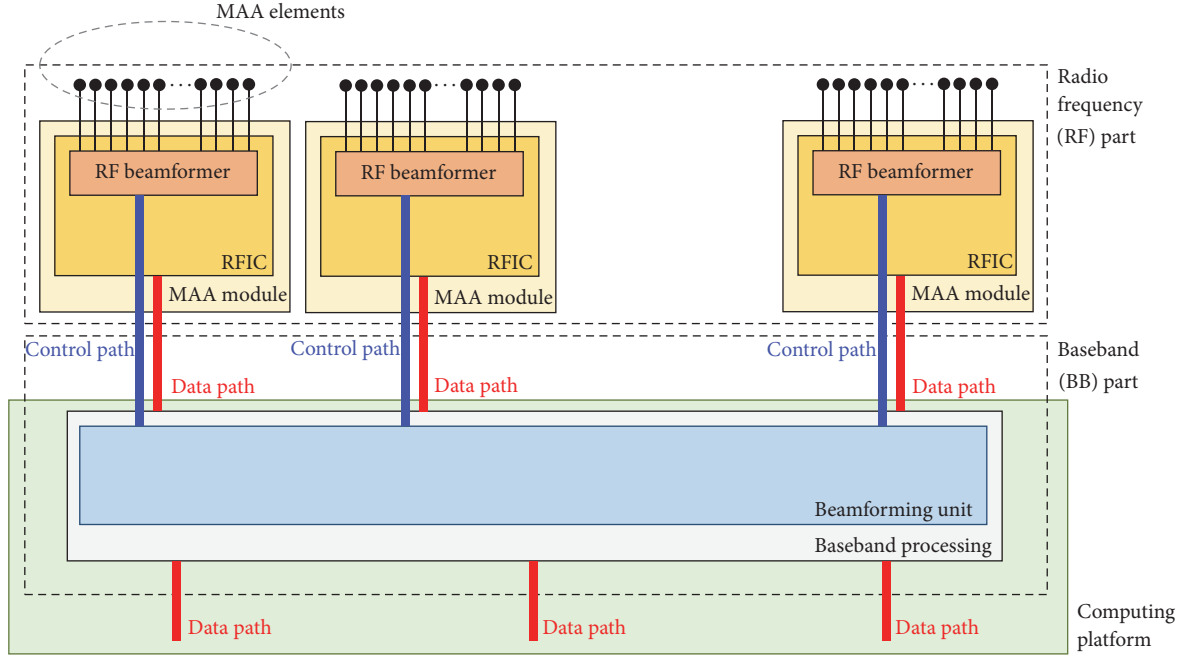


FIGURE 1: High level block diagram of the proposed modular antenna array (MAA) architecture.

One of novel antenna array architectures for the 60 GHz band that provides simultaneous flexibility in form factor choice, beam steering, and high array gain in a conceivably more cost-efficient manner is to construct modular antenna arrays (MAAs). As shown in Figure 1, the MAA architecture consists of baseband part and RF part. The baseband part is embedded in a computing platform. The data from the computing platform will be delivered to the baseband. The baseband part has baseband processing (which is for data processing and also for sending the data to RFIC) and beamforming unit (which is for forming beams toward one dedicated direction and also for setting phase shifting values for the RF beamformers in connected MAA modules). The phase shifting values for the RF beamformers in MAA modules are transmitted through interconnection control paths from baseband beamforming unit to MAA modules. Each module is implemented in a traditional way with dedicated RFIC serving 16 (i.e., 8-by-2) MAA elements through an RF beamformer. The RFIC receives data from baseband processing unit and sends the information to its own RF beamformer in order to transmit over 60 GHz mmWave wireless channels.

The aperture of MAA and total transmitted power may exceed that of an individual MAA module proportionally to the number of the MAA modules used. Therefore, much narrower beams may be created and, thus, much greater antenna gains may be achieved with the MAA as opposed to individual subarrays. It is also possible that sectors of different subarrays may be configured in such a way as to vary the coverage angle of the composite array, thereby creating several coverage angles. Each MAA module has an 8-by-2 elements where the transmit power and the transmit antenna gain are determined as 10 dBm and 15 dBi. In Figure 2,

currently developing integrated 8-module MAA prototype is presented.

More various usage scenarios and details of the proposed MAA architectures are presented in [6].

3. Link Budget Estimation

The link budget estimation procedure is illustrated in Figure 3. As shown in Figure 3, the transmitted signal from a transmitter MAA (Tx-MAA) toward a receiver MAA (Rx-MAA) over 60 GHz mmWave channels will be attenuated by path-loss, oxygen absorption, and rain effects depending on the distance between the Tx-MAA and the Rx-MAA. When the signal arrives at the Rx-MAA after experiencing attenuation effects, a receiver antenna gain will be added on top of the received signal strength. This procedure can be formulated as follows:

$$P_{dBm}^{Rx}(d) = EIRP_{dBm} - PL(d) - O(d) - R(d) + G_{dBi}^{Rx}, \quad (1)$$

where $P_{dBm}^{Rx}(d)$ is a received signal strength at an Rx-MAA, $EIRP_{dBm}$ is equivalent isotropically radiated power (EIRP), the limit in USA is 43 dBm (peak) [7–9], $PL(d)$ is path-loss depending on the separation distance between a Tx-MAA and an Rx-MAA d , $O(d)$ is oxygen attenuation depending on the separation distance, $R(d)$ is rain attenuation depending on the separation distance, and G_{dBi}^{Rx} is a receive antenna gain at an Rx-MAA, respectively.

In WiGig/IEEE 802.11ad [10], supportable MCS indices and their corresponding data rates depending on receiver sensitivity values are defined in Tables 21-3. The given Tables 21-3 in WiGig/IEEE 802.11ad can be reproduced as

TABLE 1: WiGig/IEEE 802.11ad MCS Index Table (regenerated from Table 21-3 in WiGig/IEEE 802.11ad [10]), assuming that (i) 5 dB implementation loss, (ii) 10 dB noise factor (Noise Figure), and (iii) packet error rate (PER) shall be less than 1% when the payload length is 4000 bytes.

Receiver Sensitivity	MCS index (Achievable rates, unit: Mbps)	SC-based MCS (Mandatory SC)	Full MCS (Including optional OFDM)
-78 dBm	MCS0 (27.5)	MCS0 ($i_{MCS} = 1$)	MCS0 ($i_{MCS} = 1$)
-68 dBm	MCS1 (385)	MCS1 ($i_{MCS} = 2$)	MCS1 ($i_{MCS} = 2$)
-66 dBm	MCS2 (770), MCS13 (693)	MCS2 ($i_{MCS} = 3$)	MCS2 ($i_{MCS} = 3$)
-65 dBm	MCS3 (962.5)	MCS3 ($i_{MCS} = 4$)	MCS3 ($i_{MCS} = 4$)
-64 dBm	MCS4 (1155), MCS14 (866.25), MCS25 (626)	MCS4 ($i_{MCS} = 5$)	MCS4 ($i_{MCS} = 5$)
-63 dBm	MCS6 (1540), MCS15 (1386)	MCS6 ($i_{MCS} = 6$)	MCS6 ($i_{MCS} = 6$)
-62 dBm	MCS5 (1251.25), MCS7 (1925), MCS16 (1732.5)	MCS7 ($i_{MCS} = 7$)	MCS7 ($i_{MCS} = 7$)
-61 dBm	MCS8 (2310)	MCS8 ($i_{MCS} = 8$)	MCS8 ($i_{MCS} = 8$)
-60 dBm	MCS17 (2079), MCS26 (834)	—	—
-59 dBm	MCS9 (2502.5)	MCS9 ($i_{MCS} = 9$)	MCS9 ($i_{MCS} = 9$)
-58 dBm	MCS18 (2772)	—	MCS18 ($i_{MCS} = 10$)
-57 dBm	MCS27 (1112), MCS28 (1251), MCS29 (1668), MCS30 (2224), MCS31 (2503)	—	—
-56 dBm	MCS19 (3465)	—	MCS19 ($i_{MCS} = 11$)
-55 dBm	MCS10 (3080)	MCS10 ($i_{MCS} = 10$)	—
-54 dBm	MCS11 (3850), MCS20 (4158)	MCS11 ($i_{MCS} = 11$)	MCS20 ($i_{MCS} = 12$)
-53 dBm	MCS12 (4620), MCS21 (4504.5)	MCS12 ($i_{MCS} = 12$)	MCS12 ($i_{MCS} = 13$)
-51 dBm	MCS22 (5197.5)	—	MCS22 ($i_{MCS} = 14$)
-49 dBm	MCS23 (6237)	—	MCS23 ($i_{MCS} = 15$)
-47 dBm	MCS24 (6756.75)	—	MCS24 ($i_{MCS} = 16$)

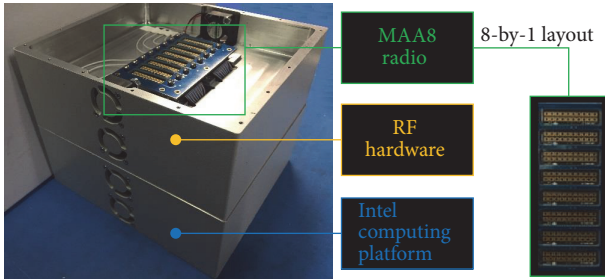


FIGURE 2: Integrated 60 GHz mmWave MAA architectures and snapshots.

Table 1 by reordering MCS values in terms of receiver sensitivity values. Moreover, if multiple MCS values are supportable in a specific receiver sensitivity value, the MCS value which can provide the highest achievable rate will be obviously used. Note that the reproduced Table 1 includes MCS Table Index values denoted as i_{MCS} . In addition, single carrier (SC) based MCS features are mandatory (from MCS0 to MCS12) and orthogonal frequency division multiplexing (OFDM) based MCS features (from MCS13 to MCS24) and low-power SC-based MCS features (from MCS25 to MCS31) are optional in WiGig/IEEE 802.11ad [10].

If the calculated received signal strength at an Rx-MAA by (1) is higher than the receiver sensitivity of an MCS Table Index i_{MCS} and lower than the receiver sensitivity of MCS Table Index $i_{MCS} + 1$, the 60 GHz WiGig/IEEE 802.11ad wireless communication link should use MCS Table Index i_{MCS} . Therefore, if the distance of the wireless communication link

is getting longer, $P_{dBm}^{Rx}(d)$ becomes lower due to attenuation factors (i.e., path-loss, oxygen, and rain) as shown in Figure 3; then the index of supportable MCS becomes lower as well. This lower MCS introduces more robust modulation and coding schemes; however, it also introduces lower physical data rates. This calculation procedure is summarized in Algorithm 1. In addition, the following sections include the detailed calculation procedures of EIRP (refer to Section 3.1), path-loss (refer to Section 3.2), mmWave specific attenuation (refer to Section 3.3), and receiver antenna gain (refer to Section 3.4).

3.1. EIRP. In (1), $EIRP_{dBm}$ can be calculated as follows:

$$EIRP_{dBm} = G_{dBi}^{Tx} + P_{dBm}^{Tx}, \quad (2)$$

where G_{dBi}^{Tx} and P_{dBm}^{Tx} are a transmit antenna gain and a transmit power at a Tx-MAA. In 1-module Tx-MAA (Tx-MAA1), G_{dBi}^{Tx} and P_{dBm}^{Tx} are 15 dBi and 10 dBm. In addition, G_{dBi}^{Tx} in 8-module MAA (Tx-MAA8) and P_{dBm}^{Tx} in Tx-MAA8 are 24 dBi and 19 dBm, respectively.

3.2. 60 GHz mmWave Path-Loss Models. Two different 60 GHz path-loss models are considered in this link budget estimation study: (i) LoS scenario and (ii) street canyon scenario.

The 60 GHz LoS path-loss is [11, 12]

$$PL(d) = 92.44 + 20 \log_{10}(f) + 10n \log_{10}(d) \quad (3)$$

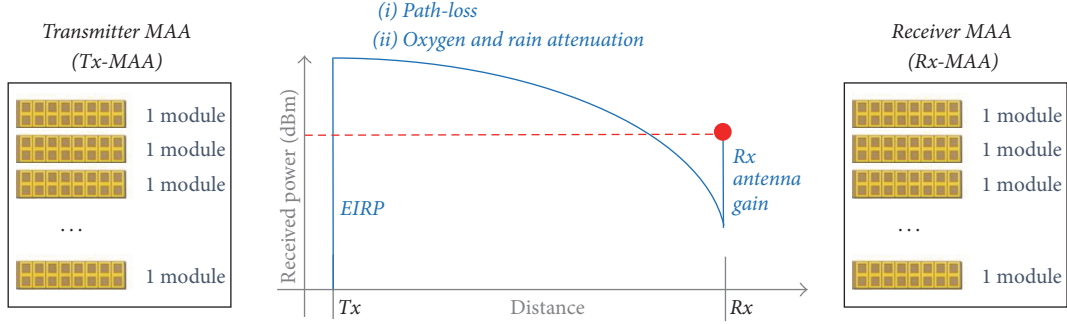
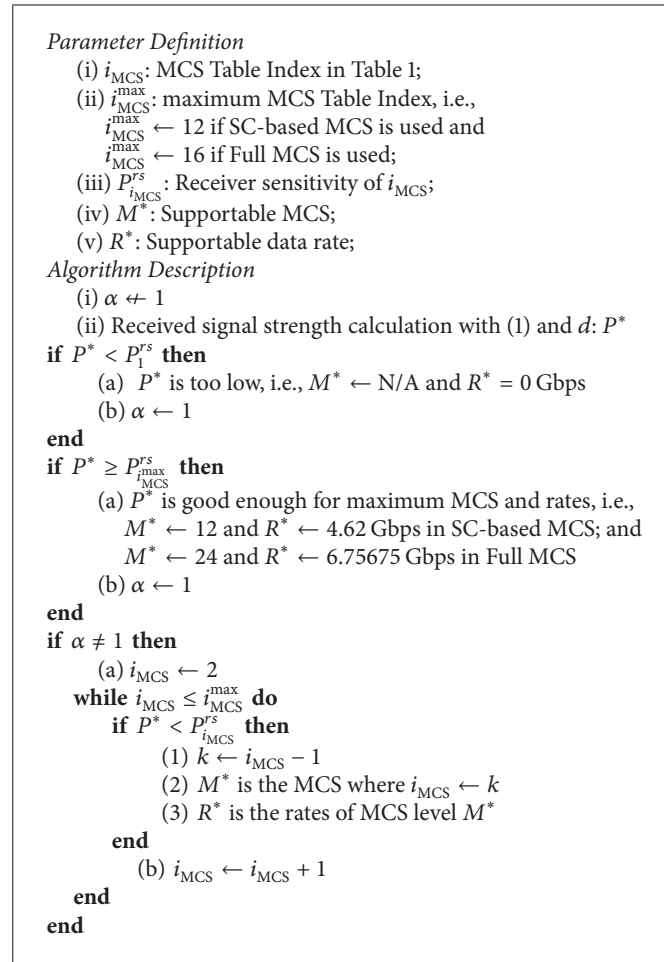


FIGURE 3: Link budget calculation procedure.

ALGORITHM 1: Link budget estimation when the distance between Tx-MAA and Rx-MAA is d m.

and the 60 GHz *street canyon* (illustrated in Figure 4) path-loss is as follows [11]:

$$PL(d) = 82.02 + 10n \log_{10} \left(\frac{d}{d_0} \right) \Bigg|_{d_0=5}, \quad (4)$$

where d is a distance between Tx-MAA and Rx-MAA (unit: meter); f is a carrier frequency in a GHz scale; n is a path-loss coefficient, where

$$n = \begin{cases} 2.00, & \text{in an LoS scenario [11, 12],} \\ 2.36, & \text{in a street canyon scenario [11].} \end{cases} \quad (5)$$

TABLE 2: Rain rates (unit: mm/h, i.e., millimeter per hour) and their corresponding attenuation factors (unit: dB/Km, i.e., decibel per kilometer) at 60 GHz depending on rain climatic zones (especially for ITU Regions D, P, and Q) [14].

ITU region	99.0% availability	99.9% availability
ITU Region D (Northern CA, OR, WA)	2.1 mm/h (1.2 dB/Km)	8 mm/h (3.5 dB/Km)
ITU Region P [heavy rain areas] (Brazil and so on)	12 mm/h (5 dB/Km)	65 mm/h (21 dB/Km)
ITU Region Q [heavy rain areas] (Middle Africa and so on)	24 mm/h (9 dB/Km)	72 mm/h (25 dB/Km)

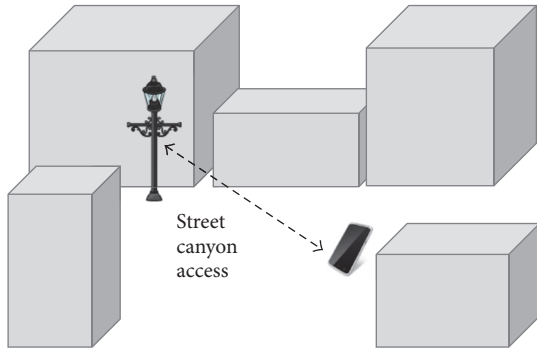


FIGURE 4: Illustration of street canyon access [11].

3.3. *mmWave Specific Attenuation Factors.* As explained in [12], attenuation by atmospheric gases (i.e., oxygen attenuation) and by rain must be considered in millimeter-wave propagation.

The oxygen attenuation $O(d)$ is observed as 16 dB/Km [13]; that is, $O(d) = 16 \cdot d/1000$, where d is a distance between Tx-MAA and Rx-MAA in a meter scale.

The rain attenuation factors depend on the rain climatic zones that are segmented and measured by the International Telecommunication Union (ITU) [14]. Table 1 in [14] presents rain rates depending on the segmented areas (from ITU Region A to ITU Region Q). In this paper, ITU Region D (Northern California (CA), Oregon (OR), and Washington (WA)), ITU Region P (heavy rain areas such as Brazil), and ITU Region Q (heavy rain areas such as Middle Africa) are of interest. Table 2 presents the rain rates of ITU regions D, P, and Q (unit: mm/h) and their corresponding rate attenuation factors (unit: dB/Km) based on [15] and Figure 5.

3.4. *Receiver Antenna Gain.* The receiver antenna gain $G_{\text{dBi}}^{\text{Rx}}$ is equal to $G_{\text{dBi}}^{\text{Tx}}$ in Section 3.1 because equivalent MAA antenna systems are used for both Tx-MAA and Rx-MAA. Therefore,

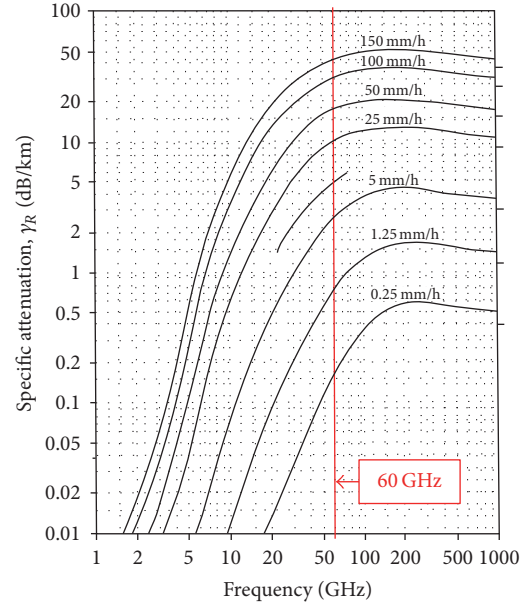


FIGURE 5: Rain attenuation factor estimation from FCC measurement results [15].

$G_{\text{dBi}}^{\text{Rx}}$ values are 15 dBi and 24 dBi in Rx-MAA1 and Rx-MAA8, respectively.

4. Link Budget Estimation Results

The link budget estimation performs with three different network scenarios as illustrated in Figure 6, that is, (i) peer-to-peer (P2P) links where each peer has MAA1 (i.e., MAA1-MAA1 link); (ii) AP-to-DEV (device) links where each AP and each DEV have MAA8 and MAA1 (i.e., MAA8-MAA1 link); and (iii) backhaul links where each backhaul base station (BS) has MAA8 (i.e., MAA8-MAA8 link). Note that the scenario of AP-to-DEV links is equivalent with the scenario of cellular links where a BS has MAA8 and a mobile user has MAA1.

4.1. *Link Budget Estimation.* With the given three scenarios, link budget estimation performs depending on two different path-loss models, different ITU regional segments (no rain case, ITU Region D, ITU Region P, and ITU Region Q), and different availability probabilities in each regional segments (99.0% or 99.9%). After performing all possible combinations of link budget estimation, various achievable distances depending on various target data rates (1 Gbps, 2 Gbps, 3 Gbps, and 4 Gbps for mandatory SC-based MCS; and 1 Gbps, 2 Gbps, 3 Gbps, 4 Gbps, 5 Gbps, and 6 Gbps for full MCS) are calculated as presented in Table 3. From Table 3, some remarkable facts are as follows:

- (i) In an MAA1-MAA1 link, 1 Gbps rates are achievable up to maximum 56.80 m (in LoS scenario and no rain) and minimum 36.84 m (in a street canyon scenario and ITU Region Q with 99% availability).

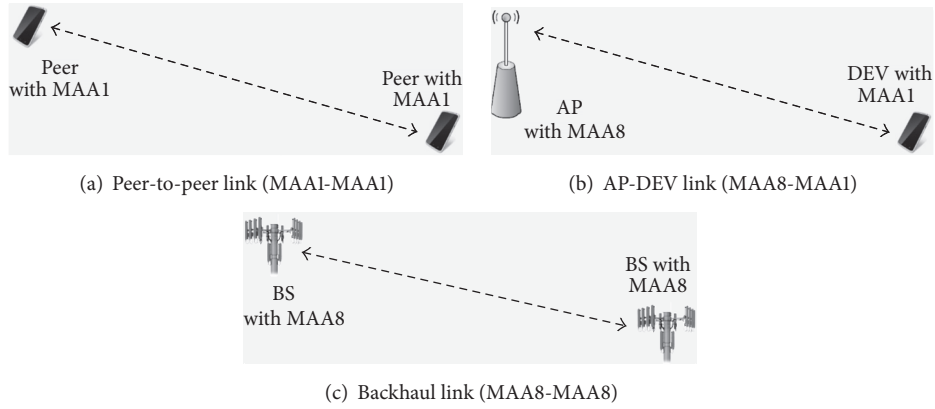


FIGURE 6: Link budget analysis scenarios with MAA.

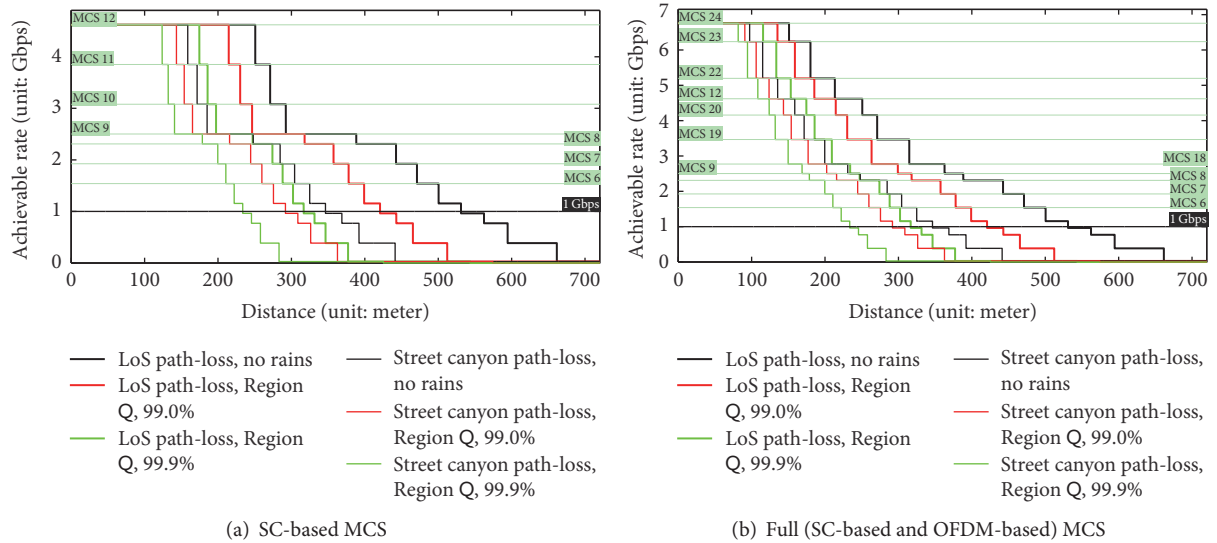


FIGURE 7: Link budget estimation for backhaul link (MAA8-MAA8, as illustrated in Figure 6(c)) with various path-loss models and rain rates.

- (ii) In an MAA8-MAA1 link, 1 Gbps rates are achievable up to maximum 292.37 m (in LoS scenario and no rain) and minimum 140.76 m (in a street canyon scenario and ITU Region Q with 99% availability).
- (iii) In an MAA8-MAA8 backhaul link, 1 Gbps rates are achievable up to maximum 530.97 m (in LoS scenario and no rain) and minimum 233.62 m (in a street canyon scenario and ITU Region Q with 99% availability).

4.2. *Performance Reduction due to Various Rain Attenuation Factors.* Table 4 presents the performance degradation ratio due to various rain attenuation factors. The data in Table 4 can be calculated as follows:

$$\gamma = \frac{\delta_{\text{no-rain}} - \delta^*}{\delta_{\text{no-rain}}} \times 100, \quad (6)$$

where $\delta_{\text{no-rain}}$ stands for the achievable distance (from Table 3) when there is no rain and δ^* stands for the achievable

distance (from Table 3) for specific thresholds, regions, and availability probabilities. By calculating γ (presented in Table 4), we can determine how much rain attenuation affects the achievable distance reduction.

As shown in Table 4, the performance degradation is mainly observed in LoS scenario and the ITU Region Q with 99.9% availability. The most significant performance degradation can be observed in the MAA8-MAA8 link when its target rate is 1 Gbps in an LoS scenario and the ITU Region Q with 99.9% availability, that is, about 40.36%.

4.3. *Case Study for Backhaul Link Budget Estimation in Heavy Rain Areas (ITU Region Q).* The presented 60 GHz MAA platform is originally designed for wireless backhaul networks, that is, MAA8-MAA8 link. Therefore, the link budget estimation for MAA8-MAA8 link is performed and plotted as shown in Figure 7. If service providers want to deploy these MAA boxes for constructing ad hoc mesh backhaul networks with the threshold of 1 Gbps, the following distances

TABLE 3: Achievable distances (unit: meter) for target data rates.

Scenario	Path-loss	ITU region	SC-based MCS				Full (SC-based and OFDM-based) MCS					
			4 Gbps	3 Gbps	2 Gbps	1 Gbps	6 Gbps	5 Gbps	4 Gbps	3 Gbps	2 Gbps	1 Gbps
MAA1-MAA1 (Figure 6(a))	LoS	No rains	17.22	21.51	41.37	56.80	10.99	13.76	19.25	24.02	41.37	56.80
		D (99.0%)	17.17	21.44	41.15	56.40	10.98	13.74	19.20	23.94	41.15	56.40
		P (99.0%)	17.05	21.25	40.48	55.19	10.92	13.66	19.04	23.71	40.48	55.19
		Q (99.0%)	16.93	21.06	39.81	53.99	10.87	13.57	18.89	23.46	39.81	53.99
		D (99.9%)	17.10	21.33	40.74	55.66	10.94	13.69	19.10	23.80	40.74	55.66
		P (99.9%)	16.56	20.50	37.98	50.80	10.71	13.34	18.43	22.78	37.98	50.80
	Street canyon	Q (99.9%)	16.44	20.33	37.42	49.84	10.66	13.26	18.29	22.57	37.42	49.84
		No rains	14.27	17.26	30.38	40.09	9.73	11.78	15.70	18.98	30.38	40.09
		D (99.0%)	14.25	17.23	30.27	39.92	9.71	11.77	15.67	18.94	30.27	39.92
		P (99.0%)	14.17	17.12	29.96	39.38	9.68	11.72	15.58	18.81	29.96	39.38
		Q (99.0%)	14.10	17.01	29.63	38.83	9.64	11.67	15.49	18.68	29.63	38.83
		D (99.9%)	14.20	17.17	30.08	39.59	9.69	11.74	15.62	18.86	30.08	39.59
MAA8-MAA1 (Figure 6(b))	LoS	P (99.9%)	13.88	16.70	28.71	37.31	9.54	11.51	15.23	18.30	28.71	37.31
		Q (99.9%)	13.81	16.60	28.43	36.84	9.51	11.46	15.14	18.18	28.43	36.84
		No rains	114.37	137.89	231.53	292.37	77.27	94.28	125.68	151.01	231.53	292.37
		D (99.0%)	112.91	135.83	226.49	284.95	76.56	93.25	123.95	148.60	226.49	284.95
		P (99.0%)	108.59	129.86	212.29	264.38	74.42	90.18	118.86	141.62	212.29	264.38
		Q (99.0%)	104.51	124.30	199.65	246.46	72.34	87.25	114.08	135.17	199.65	246.46
	Street canyon	D (99.9%)	110.24	132.13	217.61	272.03	75.24	91.36	120.80	144.27	217.61	272.03
		P (99.9%)	94.43	110.85	171.11	207.23	66.97	79.82	102.41	119.75	171.11	207.23
		Q (99.9%)	91.62	107.18	163.74	197.36	65.42	77.71	99.19	115.58	163.74	197.36
		No rains	75.17	89.36	146.70	185.14	52.68	63.01	81.98	97.29	146.70	185.14
		D (99.0%)	74.58	88.55	144.69	182.10	52.39	62.59	81.29	96.34	144.69	182.10
		P (99.0%)	72.80	86.11	138.80	173.30	51.47	61.32	79.21	93.50	138.80	173.30
MAA8-MAA8 (Figure 6(c))	LoS	Q (99.0%)	71.06	83.74	133.27	165.20	50.56	60.05	77.18	90.76	133.27	165.20
		D (99.9%)	73.48	87.04	141.05	176.63	51.83	61.81	80.01	94.59	141.05	176.63
		P (99.9%)	66.48	77.62	119.73	145.95	48.08	56.66	71.88	83.71	119.73	145.95
		Q (99.9%)	65.13	75.84	115.98	140.76	47.33	55.65	70.32	81.68	115.98	140.76
		No rains	250.75	292.37	442.46	530.97	180.17	213.37	271.03	314.78	442.46	530.97
		D (99.0%)	244.99	284.95	428.17	512.15	176.89	208.98	264.48	306.42	428.17	512.15
	Street canyon	P (99.0%)	228.85	264.38	389.66	462.05	167.48	196.54	246.21	283.35	389.66	462.05
		Q (99.0%)	214.59	246.46	357.37	420.70	158.92	185.39	230.19	263.39	357.37	420.70
		D (99.9%)	234.87	272.03	403.78	480.32	171.03	201.21	253.01	291.90	403.78	480.32
		P (99.9%)	182.72	207.23	290.28	336.60	138.93	159.94	194.77	220.11	290.28	336.60
		Q (99.9%)	174.57	197.36	274.10	316.68	133.63	153.30	185.78	209.30	274.10	316.68
		No rains	158.73	185.14	284.64	346.38	115.03	135.43	171.54	199.57	284.64	346.38
Street canyon	D (99.0%)	156.41	182.10	278.27	337.57	113.73	133.69	168.88	196.10	278.27	337.57	
	P (99.0%)	149.66	173.30	260.36	313.14	109.90	128.57	161.16	186.12	260.36	313.14	
	Q (99.0%)	143.35	165.20	244.49	291.87	106.23	123.73	154.00	176.98	244.49	291.87	
	D (99.9%)	152.23	176.63	267.06	322.22	111.37	130.52	164.08	189.89	267.06	322.22	
	P (99.9%)	128.08	145.95	208.85	245.33	96.99	111.76	136.82	155.47	208.85	245.33	
	Q (99.9%)	123.89	140.76	199.68	233.62	94.37	108.43	132.15	149.72	199.68	233.62	

TABLE 4: Performance reduction depending on various regions and rain rates (calculated based on the data from Table 3).

Scenario	Path-loss	ITU region	SC-based MCS			Full (SC-based and OFDM-based) MCS						
			4 Gbps	3 Gbps	2 Gbps	1 Gbps	6 Gbps	5 Gbps	4 Gbps	3 Gbps	2 Gbps	1 Gbps
MAA1-MAA1 (Figure 6(a))	LoS	D (99.0%)	0.29%	0.33%	0.53%	0.70%	0.09%	0.15%	0.26%	0.33%	0.53%	0.70%
		P (99.0%)	0.99%	1.21%	2.15%	2.83%	0.64%	0.73%	1.09%	1.29%	2.15%	2.83%
		Q (99.0%)	1.68%	2.09%	3.77%	4.95%	1.09%	1.38%	1.87%	2.33%	3.77%	4.95%
		D (99.9%)	0.70%	0.84%	1.52%	2.01%	0.45%	0.51%	0.78%	0.92%	1.52%	2.01%
		P (99.9%)	3.83%	4.70%	8.19%	10.56%	2.55%	3.05%	4.26%	5.16%	8.19%	10.56%
	Street canyon	Q (99.9%)	4.53%	5.49%	9.55%	12.25%	3.00%	3.63%	4.99%	6.04%	9.55%	12.25%
		D (99.0%)	0.14%	0.17%	0.36%	0.42%	0.21%	0.08%	0.19%	0.21%	0.36%	0.42%
		P (99.0%)	0.70%	0.81%	1.38%	1.77%	0.51%	0.51%	0.76%	0.90%	1.38%	1.77%
		Q (99.0%)	1.19%	1.44%	2.47%	3.14%	0.92%	0.93%	1.34%	1.58%	2.47%	3.14%
		P (99.9%)	0.49%	0.52%	0.99%	1.25%	0.41%	0.34%	0.51%	0.63%	0.99%	1.25%
MAA8-MAA1 (Figure 6(b))	LoS	D (99.9%)	2.73%	3.24%	5.50%	6.93%	1.95%	2.29%	2.99%	3.58%	5.50%	6.93%
		P (99.9%)	3.22%	3.82%	6.42%	8.11%	2.26%	2.72%	3.57%	4.21%	6.42%	8.11%
		D (99.0%)	1.27%	1.49%	2.18%	2.54%	0.92%	1.09%	1.38%	1.60%	2.18%	2.54%
		P (99.0%)	5.05%	5.82%	8.31%	9.57%	3.69%	4.35%	5.43%	6.22%	8.31%	9.57%
		Q (99.0%)	8.62%	9.86%	13.77%	15.70%	6.38%	7.46%	9.23%	10.49%	13.77%	15.70%
	Street canyon	D (99.9%)	3.61%	4.18%	6.01%	6.96%	2.63%	3.10%	3.88%	4.46%	6.01%	6.96%
		P (99.9%)	17.43%	19.61%	26.10%	29.12%	13.33%	15.34%	18.52%	20.70%	26.10%	29.12%
		Q (99.9%)	19.89%	22.27%	29.28%	32.50%	15.34%	17.58%	21.08%	23.46%	29.28%	32.50%
		D (99.0%)	0.78%	0.91%	1.37%	1.64%	0.55%	0.67%	0.84%	0.98%	1.37%	1.64%
		P (99.0%)	3.15%	3.64%	5.39%	6.40%	2.30%	2.68%	3.38%	3.90%	5.39%	6.40%
MAA8-MAA8 (Figure 6(c))	LoS	D (99.9%)	5.47%	6.29%	9.15%	10.77%	4.02%	4.70%	5.86%	6.71%	9.15%	10.77%
		P (99.9%)	2.25%	2.60%	3.85%	4.60%	1.61%	1.90%	2.40%	2.78%	3.85%	4.60%
		Q (99.9%)	11.56%	13.14%	18.38%	21.17%	8.73%	10.08%	12.32%	13.96%	18.38%	21.17%
		D (99.0%)	13.36%	15.13%	20.94%	23.97%	10.16%	11.68%	14.22%	16.04%	20.94%	23.97%
		P (99.0%)	2.30%	2.54%	3.23%	3.54%	1.82%	2.06%	2.42%	2.66%	3.23%	3.54%
	Street canyon	Q (99.0%)	8.73%	9.57%	11.93%	12.98%	7.04%	7.89%	9.16%	9.98%	11.93%	12.98%
		D (99.9%)	14.42%	15.70%	19.23%	20.77%	11.79%	13.11%	15.07%	16.33%	19.23%	20.77%
		P (99.9%)	6.33%	6.96%	8.74%	9.54%	5.07%	5.70%	6.65%	7.27%	8.74%	9.54%
		Q (99.9%)	29.12%	34.39%	36.61%	36.61%	22.89%	25.04%	28.14%	30.07%	34.39%	36.61%
		D (99.0%)	30.38%	32.50%	38.05%	40.36%	25.83%	28.15%	31.45%	33.51%	38.05%	40.36%
Street canyon	P (99.0%)	1.46%	1.64%	2.24%	2.54%	1.13%	1.28%	1.55%	1.74%	2.24%	2.54%	
	D (99.0%)	5.71%	6.40%	8.53%	9.60%	4.46%	5.07%	6.05%	6.74%	8.53%	9.60%	
	Q (99.0%)	9.69%	10.77%	14.11%	15.74%	7.65%	8.64%	10.23%	11.32%	14.11%	15.74%	
	D (99.9%)	4.10%	4.60%	6.18%	6.97%	3.18%	3.63%	4.35%	4.85%	6.18%	6.97%	
	P (99.9%)	19.31%	21.17%	26.63%	29.17%	15.68%	17.48%	20.24%	22.10%	26.63%	29.17%	
Q (99.9%)	21.95%	23.97%	29.85%	32.55%	17.96%	19.94%	22.96%	24.98%	29.85%	32.55%		

should be maintained: that is, 530.97 m (no rains), 420.70 m (ITU Region Q with 99.0% availability), and 316.68 m (ITU Region Q with 99.9% availability).

5. Conclusions and Future Work

This paper presents practical link budget estimation results with IEEE 802.11ad standard-defined parameters and 60 GHz mmWave specific attenuation factors. In addition, the used system parameters are obtained from the real-world prototype which is currently developing for 60 GHz wireless backhaul networking. Based on the link budget estimation results, achievable distances between a transmitter and a receiver are determined depending on various thresholds of data rates in various regions, availability probabilities, and path-loss models.

For future research direction, the link budget estimation with the other mmWave frequencies can be considerable for next-generation cellular and access systems.

Additional Points

More details about path-loss and radio propagation measurements are presented in [11]. The presented MAA radio platform in Section 2 and Figure 2 is the real-world prototype developed by Intel Corporation and was demonstrated at Mobile World Congress (MWC), 2015.

Conflicts of Interest

The authors declare that they have no conflicts of interest.

Acknowledgments

Joongheon Kim is the corresponding author. This work was supported by Intel Next Generation and Standards (NGS) funds and also by National Research Foundation of Korea (NRF Korea) under Grant 2016R1C1B1015406 and also supported by Institute of Information and Communications Technology Promotion (IITP) grant funded by the Korea government (MSIP) (2017-0-00804, "Feasibility Study of 60 GHz IEEE 802.11ad for Virtual Reality (VR) Platforms").

References

- [1] W. Roh, J.-Y. Seol, J. Park et al., "Millimeter-wave beamforming as an enabling technology for 5G cellular communications: theoretical feasibility and prototype results," *IEEE Communications Magazine*, vol. 52, no. 2, pp. 106–113, 2014.
- [2] T. S. Rappaport, F. Gutierrez, E. Ben-Dor, J. N. Murdock, Y. Qiao, and J. I. Tamir, "Broadband millimeter-wave propagation measurements and models using adaptive-beam antennas for outdoor Urban cellular communications," *IEEE Transactions on Antennas and Propagation*, vol. 61, no. 4, pp. 1850–1859, 2013.
- [3] J. Kim, L. Xian, A. Maltsev, R. Arefi, and A. S. Sadri, "Study of coexistence between 5G small-cell systems and systems of the fixed service at 39 GHz band," in *Proceedings of the IEEE MTT-S International Microwave Symposium (IMS '15)*, IEEE, May 2015.
- [4] T. S. Rappaport, J. N. Murdock, and F. Gutierrez, "State of the art in 60-GHz integrated circuits and systems for wireless communications," *Proceedings of the IEEE*, vol. 99, no. 8, pp. 1390–1436, 2011.
- [5] S. Nie, G. R. MacCartney, S. Sun, and T. S. Rappaport, "28 GHz and 73 GHz signal outage study for millimeter wave cellular and backhaul communications," in *Proceedings of the 1st IEEE International Conference on Communications, (ICC '14)*, pp. 4856–4861, June 2014.
- [6] J. Kim, L. Xian, and A. S. Sadri, "Numerical simulation study for frequency sharing between micro-cellular systems and fixed service systems in millimeter-wave bands," *IEEE Access*, vol. 4, pp. 9847–9859, 2016.
- [7] J. Kim, Y. Tian, S. Mangold, and A. F. Molisch, "Joint scalable coding and routing for 60 GHz real-time live HD video streaming applications," *IEEE Transactions on Broadcasting*, vol. 59, no. 3, pp. 500–512, 2013.
- [8] J. Kim, Y. Tian, S. Mangold, and A. F. Molisch, "Quality-aware coding and relaying for 60 GHz real-time wireless video broadcasting," in *Proceedings of the IEEE International Conference on Communications (ICC '13)*, pp. 5148–5152, Budapest, Hungary, June 2013.
- [9] J. Kim and A. F. Molisch, "Enabling Gigabit services for IEEE 802.11ad-capable high-speed train networks," in *Proceedings of the 2013 IEEE Radio and Wireless Symposium (RSW '13)*, pp. 145–147, January 2013.
- [10] IEEE, *IEEE 802.11ad Specification*, IEEE, December 2012.
- [11] A. Maltsev, A. Puduev, I. Bolotin et al., "Millimetre-wave evolution for backhaul and access (MiWEBA) WP5 D5.1: channel modeling and characterization," *MiWEBA Project Document, EU Contract No. FP7-ICT-608637*, 2014.
- [12] ITU, "Propagation data and prediction methods for the planning of short-range outdoor radiocommunication systems and radio local area networks in the frequency range 300 MHz to 100 GHz," *ITU-R P.1411-7*, September 2013.
- [13] S. Singh, R. Mudumbai, and U. Madhow, "Interference analysis for highly directional 60-GHz mesh networks: the case for rethinking medium access control," *IEEE/ACM Transactions on Networking*, vol. 19, no. 5, pp. 1513–1527, 2011.
- [14] ITU, "Characteristics of Precipitation for Propagation Modelling," *ITU-R PN.837-1*, 1994.
- [15] FCC, "Bulletin Number 70," July 1997.

Research Article

Novel Method for 5G Systems NLOS Channels Parameter Estimation

Vladeta Milenkovic,¹ Stefan Panic,² Dragan Denic,¹ and Dragan Radenkovic¹

¹Faculty of Electrical Engineering, University of Niš, Niš, Serbia

²Faculty of Natural Science and Mathematics, University of Pristina, Pristina, Serbia

Correspondence should be addressed to Stefan Panic; stefanpnc@yahoo.com

Received 12 November 2016; Revised 4 February 2017; Accepted 12 April 2017; Published 11 May 2017

Academic Editor: Larbi Talbi

Copyright © 2017 Vladeta Milenkovic et al. This is an open access article distributed under the Creative Commons Attribution License, which permits unrestricted use, distribution, and reproduction in any medium, provided the original work is properly cited.

For the development of new 5G systems to operate in mm bands, there is a need for accurate radio propagation modelling at these bands. In this paper novel approach for NLOS channels parameter estimation will be presented. Estimation will be performed based on LCR performance measure, which will enable us to estimate propagation parameters in real time and to avoid weaknesses of ML and moment method estimation approaches.

1. Introduction

Exploitation of unused mm wave spectrum (spectrum between 6 and 300 GHz) is an efficient solution for meeting the standards for 5G networks enormous data demand growth explosion. Because of that characterization and modelling of such channel propagation in urban environments is one of most important tasks in developing novel 5G mobile access networks. Many propagation studies, performed at these bands, for these types of applications, consider line-of-sight (LOS) scenarios [1–3]. However, non-line-of-sight (NLOS) scenarios occur more often. They not only occur in cases when transmitting and receiving antenna are separated by obstructions and there is no clear optical path between the antennas, but also occur in cases when there is indeed clear optical path between the antennas, but antennas are not aligned or boresight [4]. Various outdoor propagation measurements conducted in urban environments have shown that, for reasonable level of signal-to-noise ratio (SNR), that is, higher than 5 dB, NLOS signals have stable first arriving signal levels, even if they are weaker than stronger, later-arriving multipath components, counter to LOS signals with strongest first arriving component at the reception. Measurements provided at 38 GHz (base station-to-mobile access

scenario [5] and Peer-to-Peer Scenario [6]), 60 GHz (Peer-to-Peer Scenario and vehicular scenario [7]), and 73 GHz [8] have clearly identified existence of NLOS conditions.

One of the most intensively used statistical models for characterizing the complex behavior and random nature of NLOS fading envelope is the Nakagami- m distribution. Nakagami- m fading model closely approximates data values that are obtained by providing real-time measurements in indoor and outdoor wireless environments and is often used in analyzing propagation performances in 5G systems [9–14]. In [15–17] for the purpose of modelling observed 5G system propagation properties the Nakagami m parameter is directly computed from the measured data. As a general fading distribution, Nakagami- m fading model includes in itself other distributions and its simple family form allows obtaining closed-form analytical results for wireless communication link standard performance criterion measures. Namely, Nakagami- m fading model can also be transformed into Ricean fading model, by expressing m parameter in the function of Ricean K factor, as $m = (1 + K)^2 / (1 + 2K)$ [18]. In that manner characterizing of the behavior of LOS fading envelope could be also performed. The Nakagami- m fading exploits Nakagami probability density function (PDF) for the random envelope of received signal which is

written in the function of two parameters: scale parameter and shape parameter, called the fading severity parameter or m -parameter. Determining m is a problem in Nakagami PDF estimation. For observed set of empirical fading signal data, the value of distribution parameter m should be estimated from it, in order to use the Nakagami- m distribution to model a given set of values. Acquaintance of the m parameter is mandatory for the optimal reception of signals in Nakagami- m fading environment [19], and in such case parameter m should be determined very accurately and very fast. Acquaintance of the m parameter is also necessary in the transmitter adaptation process, where its value could be feedback with respect to the channel information. Two most well-known procedures used for the estimation of the Nakagami- m fading parameter, m , are (1) maximum likelihood (ML) estimation and (2) moment-based estimation. ML-based m parameter estimation problem reduces to the problem of solving some transcendental equations written in the form of logarithmic and digamma functions. During the process of Gamma shape parameter estimation authors of [20] have developed most famous ML-based estimator of m parameter. Recently, another two approximate ML-based estimators have been proposed in [21], where estimation is carried out by observing approximations of digamma function, that is, first-order approximation and second-order approximation. Opposite approach to the ML estimation of m parameter is the moment-based estimation. Observing the second and the fourth Nakagami- m sample moments, estimation of parameter m was carried out in [22]. An improvement of proposed method can be found in [23] where parameter m estimation is carried on capitalizing on the first and the third sample moments. Group of new moment estimators form based on noninteger sample moments (estimators based on integer sample moment are their special cases), along with simulation study, was proposed in [24]. The generalized method of moments (GMM) is introduced for the estimation of the Nakagami- m fading parameter in [25]. However, it is known that sample moments are often subjected to the effects of outliers (even a small portion of extreme values, outliers, can affect the Gaussian parameters, especially the higher order moments). Moreover, occurrence of outliers is especially problematic when higher order sample moments are used for estimation, since estimation inaccuracy arises in such cases. Providing the best moment-based estimator is still major issue that should be addressed. Specifically, the level crossing rate (LCR), which provides us with a measure of the average number of crossings per second at which the envelope crosses a specified signal level in positive or negative direction, is an important second-order statistical quantity that characterizes the rate of occurrence of fade [18]. However, analytical solution for the LCR often depends mainly on the envelope distribution of the considered process.

2. Estimation Methods

2.1. Estimation for Known Power Parameter Ω . Various power estimation techniques have been implemented over years with some advantages and disadvantages. Accurate estimation of the average power of received fading signal is

crucial for many reasons. Namely, power control and hand-off decisions in wireless communications are mainly based on the accurate estimation of the average signal power. Wireless communication link quality is also indicated through some system criterion measures, such as channel access, hand-off, and power control, that can be determined mainly based on the local mean signal levels. For example, the fading signal power could be estimated by using (38) from [26] without requiring any other parameter to be estimated.

Let z denote the random envelope of received Nakagami- m faded signal, and let \dot{z} denote first derivative of z with respect to time. The joint probability density function (JPDF) of z and \dot{z} is then denoted with $p_{z\dot{z}}(z, \dot{z})$. The level crossing rate (LCR) at the envelope z is defined as the rate at which a fading signal envelope crosses level z in a positive or a negative direction and is analytically expressed by formula [18]:

$$N_z(z) = \int_0^{\infty} \dot{z} p_{z\dot{z}}(\dot{z}, z) d\dot{z}. \quad (1)$$

JPDF can be expressed through the PDF of Nakagami- m faded signal envelope, $p_z(z)$, and conditioned PDF of envelope time derivative, $p_{\dot{z}|z}(\dot{z} | z)$, as $p_{z\dot{z}}(\dot{z}, z) = p_{\dot{z}|z}(\dot{z} | z) \times p_z(z)$. PDF expression for Nakagami- m faded signal envelope, written in terms of two fading parameters, m and Ω , is given with

$$p_z(z) = \frac{2m^m z^{2m-1}}{\Omega^m \Gamma(m)} \exp\left(-m \frac{z^2}{\Omega}\right), \quad (2)$$

where $\Gamma(a)$ denotes the Gamma function [27]. Common explanation of parameters m and Ω is that Ω defines average power of faded signal; that is, $\Omega = E(z^2)$, while parameter m describes severity of fading process. As seen from [18] envelope time derivative, $p_{\dot{z}|z}(\dot{z} | z)$, is zero-mean Gaussian random process, defined with

$$p_{\dot{z}|z}(\dot{z} | z) = \frac{1}{\sqrt{2\pi}\sigma_{\dot{z}}} \exp\left(-\frac{\dot{z}^2}{2\sigma_{\dot{z}}^2}\right) \quad (3)$$

and variance of $\sigma_{\dot{z}}^2 = \pi^2 f_m^2 \Omega / m$. Here f_m is denoted by maximal Doppler shift frequency.

After substituting (2) and (3) into (1), LCR expression can be presented as

$$N_z(z) = \frac{m^{m-1/2} \sqrt{2\pi} f_m}{\Omega^{m-1/2} \Gamma(m)} z^{2m-1} \exp\left(-m \frac{z^2}{\Omega}\right). \quad (4)$$

In order to determine value of parameter m as a function of received signal level and the number of times at which level is crossed, for known value of Ω , we only need to observe two signal levels, that is, z_1 and z_2 and rates at which Nakagami- m faded signal envelope has crossed those two levels, that is, N_{z_1} and N_{z_2} that can be determined as

$$\begin{aligned} N_{z_1} &= \frac{m^{m-1/2} \sqrt{2\pi} f_m}{\Omega^{m-1/2} \Gamma(m)} z_1^{2m-1} \exp\left(-m \frac{z_1^2}{\Omega}\right), \\ N_{z_2} &= \frac{m^{m-1/2} \sqrt{2\pi} f_m}{\Omega^{m-1/2} \Gamma(m)} z_2^{2m-1} \exp\left(-m \frac{z_2^2}{\Omega}\right). \end{aligned} \quad (5)$$

TABLE 1: Comparison between parameter m value obtained by Matlab simulation over $N = 100000$ samples of Nakagami- m vector z and value of m parameter estimated by using (6) from this letter ($z_1 = \text{mean}(z)$, $z_2 = \text{mean}(z) - \text{var}(z)$, and $\Omega = E(z^2)$).

m	1	1.25	1.5	1.75	2	2.25	2.5	2.75	3
$m_{\text{estimated}}$	1.071	1.2403	1.506	1.7507	2.009	2.2509	2.518	2.7712	3.0121

TABLE 2: Comparison between parameter m value obtained by Matlab simulation over $N = 1000000$ samples of Nakagami- m vector z and value of m parameter estimated by using (6) from this letter ($z_1 = \text{mean}(z)$, $z_2 = \text{mean}(z) - \text{var}(z)$, and $\Omega = E(z^2)$).

m	1	1.25	1.5	1.75	2	2.25	2.5	2.75	3
$m_{\text{estimated}}$	1.038	1.2462	1.5042	1.7503	2.003	2.2509	2.512	2.7683	3.0117

Now, from (5) parameter m could be expressed in terms of z_1 , z_2 , N_{z_1} , and N_{z_2} as

$$m = \frac{\ln(N_{z_1}/N_{z_2}) + \ln(z_1/z_2)}{2 \ln(z_1/z_2) + (z_2^2 - z_1^2)/\Omega}. \quad (6)$$

2.2. Real Time Parameter m Estimation for Unknown Ω . In order to determine value of parameter m as a function of received signal level and the number of times at which level is crossed, for known value of Ω , we now need to observe three signal levels, that is, z_1 , z_2 , and z_3 and rates at which Nakagami- m faded signal envelope has crossed those three levels, that is, N_{z_1} , N_{z_2} , and N_{z_3} . For envelope level z_3 , LCR N_{z_3} can be expressed as follows:

$$N_{z_3} = \frac{m^{m-1/2} \sqrt{2\pi} f_m}{\Omega^{m-1/2} \Gamma(m)} z_3^{2m-1} \exp\left(-m \frac{z_3^2}{\Omega}\right). \quad (7)$$

Now, in similar manner parameter m could be expressed in terms of z_1 , z_2 , z_3 , N_{z_1} , N_{z_2} , and N_{z_3} as

$$m = \frac{1}{2} \left(1 + \frac{(z_2^2 - z_1^2) \ln(N_{z_1}/N_{z_3}) - (z_3^2 - z_1^2) \ln(N_{z_1}/N_{z_2})}{(z_2^2 - z_1^2) \ln(z_1/z_3) - (z_3^2 - z_1^2) \ln(z_1/z_2)} \right) \quad (8)$$

while now

$$\Omega = \frac{m(z_1^2 - z_2^2)}{\ln(N_{z_2}/N_{z_1}) + (2m - 1) \ln(z_1/z_2)}. \quad (9)$$

3. Numerical Results

In Table 1 comparison between parameter m value obtained by Matlab simulation over $N = 100000$ samples of Nakagami- m vector z and value of m parameter estimated by using (6) from this paper has been shown. Nakagami- m random envelope vector z was obtained from Gaussian random processes by using its property that $z = \sqrt{\sum_{i=1}^m (X_i^2 + Y_i^2)}$, where X_i and Y_i are zero-mean normally distributed Gaussian random processes, $N(0, \sigma^2)$ [18]. LCR levels z_1 and z_2 can be selected

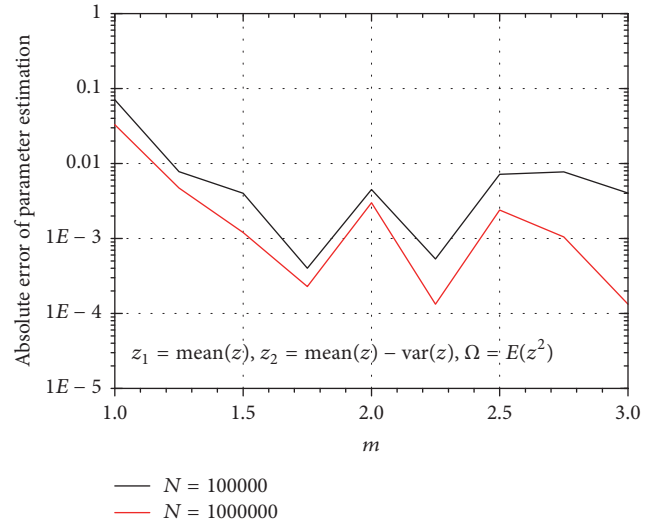


FIGURE 1: Absolute error of parameter estimation.

in a way that z_1 is level with highest number of crosses, while level z_2 is selected in the near environment of z_1 . Since it is known that envelope level z_1 for which N_{z_1} has maximal value is probably the one for each stand $z_1 = \text{mean}(z)$, level z_1 can be selected in that way, while z_2 level can be selected in the manner that $z_2 = \text{mean}(z) - \text{var}(z)$. We will observe m parameter values in the range of $m \in [1, 3]$, since in [15] it has been shown that values from this range of m parameter correspond to the case of measurements performed at 60 GHz over NLOS channel conditions, when the user was mobile in a range of different indoor and outdoor small cell scenarios. After generating Nakagami- m fading processes, characterized with $m \in [1, 3]$, and defining LCR levels for each as explained, by using proposed method based on number of level crosses, we have obtained $m_{\text{estimated}}$ for each of the generated process. As it can be seen from Table 1, shown results provide very good match and proposed method has good accuracy. In Table 2 comparison between parameter m value obtained by Matlab simulation over $N = 1000000$ samples of Nakagami- m vector z and value of m parameter estimated using (6) from this paper has been shown. Absolute error obtained for m parameter estimation for both cases has been presented in Figure 1.

By using proposed method Nakagami m parameter can be efficiently determined from various measurement, provided

for 5G channel characterization, as ones in [15–17], instead of parameter m computation by using moment-based model or the ML estimation. By using proposed method when expressing m parameter in the function of Ricean K factor, as $m = (1 + K)^2 / (1 + 2K)$, characterization of the behavior of LOS fading scenarios could be also performed.

4. Conclusion

Novel approach for Nakagami m parameter estimation based on LCR has been proposed in this paper. It has been shown that the proposed method not only avoids weaknesses of ML and moment method estimation approaches, but also is quite accurate, simple for realization, and can be used in real time. This interesting approach could also be used for fading parameters estimation of various NLOS channels in real time by using channel emulators for short, subwavelength distances in 5G multielement antenna realizations.

Conflicts of Interest

The authors declare that they have no conflicts of interest.

Acknowledgments

This work has been supported by Project III44406.

References

- [1] M. Kyro, V. Kolmonen, and P. Vainikainen, "Experimental propagation channel characterization of mm-wave radio links in urban scenarios," *IEEE Antennas and Wireless Propagation Letters*, vol. 11, pp. 865–868, 2012.
- [2] J. C. Liberti and T. S. Rappaport, "A geometrically based model for line-of-sight multipath radio channels," in *Mobile Technology for the Human Race*, vol. 2, pp. 844–848, IEEE, Atlanta, Ga, USA, April-May 1996, Proceedings of the 46th IEEE Vehicular Technology Conference.
- [3] P. Petrus, J. H. Reed, and T. S. Rappaport, "Geometrical-based statistical macrocell channel model for mobile environments," *IEEE Transactions on Communications*, vol. 50, no. 3, pp. 495–502, 2002.
- [4] T. S. Rappaport, G. R. MacCartney, M. K. Samimi, and S. Sun, "Wideband millimeter-wave propagation measurements and channel models for future wireless communication system design," *IEEE Transactions on Communications*, vol. 63, no. 9, pp. 3029–3056, 2015.
- [5] T. S. Rappaport, E. Ben-Dor, J. N. Murdock, and Y. Qiao, "Proceeding of the 38 GHz and 60 GHz angle-dependent propagation for cellular & peer-to-peer wireless communications," in *IEEE International Conference on Communications (ICC '12)*, pp. 4568–4573, Ottawa, ON, Canada, June 2012.
- [6] T. S. Rappaport, F. Gutierrez, E. Ben-Dor, J. N. Murdock, Y. Qiao, and J. I. Tamir, "Broadband millimeter-wave propagation measurements and models using adaptive-beam antennas for outdoor Urban cellular communications," *IEEE Transactions on Antennas and Propagation*, vol. 61, no. 4, pp. 1850–1859, 2013.
- [7] E. Ben-Dor, T. S. Rappaport, Y. Qiao, and S. J. Lauffenburger, "Millimeter-wave 60 GHz outdoor and vehicle AOA propagation measurements using a broadband channel sounder," in *Proceedings of the 54th Annual IEEE Global Telecommunications Conference: "Energizing Global Communications" (GLOBECOM '11)*, Kathmandu, Nepal, December 2011.
- [8] G. R. Maccartney Jr. and T. S. Rappaport, "73 GHz millimeter wave propagation measurements for outdoor urban mobile and backhaul communications in New York City," in *Proceedings of the 1st IEEE International Conference on Communications (ICC '14)*, pp. 4862–4867, Sydney, Australia, June 2014.
- [9] Z. Zhang, X. Chai, K. Long, A. V. Vasilakos, and L. Hanzo, "Full duplex techniques for 5G networks: self-interference cancellation, protocol design, and relay selection," *IEEE Communications Magazine*, vol. 53, no. 5, pp. 128–137, 2015.
- [10] J. F. Schmidt, M. K. Atiq, U. Schilcher, and C. Bettstetter, "Underlay device-to-device communications in LTE-A: uplink or downlink?" in *Proceedings of the 26th IEEE Annual International Symposium on Personal, Indoor, and Mobile Radio Communications (PIMRC '15)*, pp. 1542–1546, Hong Kong, China, September 2015.
- [11] Y. Wang and J. P. Coon, "Outage probability of fixed-gain dual-hop relay selection channels with heterogeneous fading," *Eurasip Journal on Wireless Communications and Networking*, vol. 2015, article 195, 2015.
- [12] O. Bulakci, Z. Ren, C. Zhou et al., "Towards flexible network deployment in 5G: Nomadic node enhancement to heterogeneous networks," in *Proceedings of the IEEE International Conference on Communication Workshop (ICCW '15)*, pp. 2572–2577, London, UK, June 2015.
- [13] R. He, A. F. Molisch, F. Tufvesson, Z. Zhong, B. Ai, and T. Zhang, "Vehicle-to-vehicle propagation models with large vehicle obstructions," *IEEE Transactions on Intelligent Transportation Systems*, vol. 15, no. 5, pp. 2237–2248, 2014.
- [14] X. Yu, J. Zhang, and K. Letaief, "Coverage analysis for dense millimeter wave cellular networks: the impact of array size," in *Proceedings of the Wireless Communications and Networking Conference (WCNC '16)*, vol. 3, pp. 1–6, Doha, Qatar, April 2016.
- [15] S. Yoo, S. Cotton, R. Heath Jr., and Y. Chun, "Measurements of the 60 GHz UE to eNB Channel for small cell deployments," *IEEE Wireless Communications Letters*, no. 99, pp. 1–4, 2017.
- [16] D. Beauvarlet and K. L. Virga, "Measured characteristics of 30-GHz indoor propagation channels with low-profile directional antennas," *IEEE Antennas and Wireless Propagation Letters*, vol. 1, pp. 87–90, 2002.
- [17] J. Reig, M.-T. Martínez-Inglés, L. Rubio, V.-M. Rodrigo-Peñarocha, and J. Molina-García-Pardo, "Fading evaluation in the 60 GHz band in line-of-sight conditions," *International Journal of Antennas and Propagation*, vol. 2014, Article ID 984102, 12 pages, 2014.
- [18] S. Panic, M. Stefanovic, J. Anastasov, and P. Spalevic, *Fading and Interference Mitigation in Wireless Communications*, CRC Press, Boca Raton, Fla, USA, 1st edition, 2013.
- [19] E. Belding-Royer, A. Khalidoun, and G. Pujolle, *Mobile and Communication Networks*, Paris, France, 2005.
- [20] J. A. Greenwood and D. Durand, "Aids for fitting the gamma distribution by maximum likelihood," *Technometrics*, vol. 2, no. 1, pp. 55–65, 1960.
- [21] J. Cheng and N. C. Beaulieu, "Maximum-likelihood based estimation of the nakagami m parameter," *IEEE Communications Letters*, vol. 5, no. 3, pp. 101–103, 2001.
- [22] A. Abdi and M. Kaveh, "Performance comparison of three different estimators for the nakagami m parameter using monte carlo simulation," *IEEE Communications Letters*, vol. 4, no. 4, pp. 119–121, 2000.

- [23] Y. Chen and N. Beaulieu, "Estimation of Ricean and Nakagami distribution parameters using noisy samples," in *Proceeding of the IEEE International Conference on Communications (ICC '04)*, pp. 562–566, Paris, France, June 2004.
- [24] Y. Chen, N. C. Beaulieu, and C. Tellambura, "Novel Nakagami-m parameter estimator for noisy channel samples," *IEEE Communications Letters*, vol. 9, no. 5, pp. 417–419, 2005.
- [25] N. Wang, X. Song, and J. Cheng, "Generalized method of moments estimation of the nakagami-m fading parameter," *IEEE Transactions on Wireless Communications*, vol. 11, no. 9, pp. 3316–3325, 2012.
- [26] Y.-C. Ko and M.-S. Alouini, "Estimation of nakagami-m fading channel parameters with application to optimized transmitter diversity systems," *IEEE Transactions on Wireless Communications*, vol. 2, no. 2, pp. 250–259, 2003.
- [27] I. S. Gradshteyn and I. M. Ryzhik, *Table of Integrals, Series, and Products*, Academic Press, 2007.

Research Article

Validation of the Decomposition Method for Fast MIMO Over-the-Air Measurements

Bernhard Auinger,¹ Thomas Zemen,² Michael Gadringer,¹ Adam Tankielun,³ Christoph Gagern,³ and Wolfgang Bösch¹

¹Graz University of Technology, Graz, Austria

²Austrian Institute of Technology, Vienna, Austria

³Rohde and Schwarz, Munich, Germany

Correspondence should be addressed to Bernhard Auinger; bernhard.auinger@tugraz.at

Received 5 October 2016; Revised 26 February 2017; Accepted 6 March 2017; Published 18 April 2017

Academic Editor: Mihajlo Stefanovic

Copyright © 2017 Bernhard Auinger et al. This is an open access article distributed under the Creative Commons Attribution License, which permits unrestricted use, distribution, and reproduction in any medium, provided the original work is properly cited.

Over-the-air (OTA) throughput tests of wireless Multiple-Input Multiple-Output (MIMO) devices are an important tool for network operators and manufacturers. The user equipment (UE) is placed in an anechoic chamber and a random fading process is emulated by a base-station emulator (BSE). The antenna characteristic of the UE is taken into account by sampling the sphere around the UE with the BSE test antenna at a large number of positions. For low-variance throughput results, long measurement intervals over many fading realizations are required, leading to long and expensive measurement periods in an anechoic chamber. To speed up the OTA test, we analyze the Decomposition Method (DM). The DM splits the throughput measurement into two parts: (1) a receiver algorithm performance tests taking the fading process into account and (2) an antenna performance test without fading process emulation. Both results are combined into a single throughput estimate. The DM allows for a measurement time reduction of more than *one order of magnitude*. We provide an analytic and numerical analysis as well as measurements. Our detailed results show the validity of the DM in all practical settings.

1. Introduction

With the introduction of MIMO and receiver diversity fourth- and fifth-generation (4G, 5G) wireless devices allow for large gains in throughput performance. These gains are highly dependent on the performance of the receive-antenna system [1] and the receiving algorithm [2] and the propagation environment [2]. The devices can change the behavior of the antenna systems, for example, by using beamforming mechanisms [3]. They also can adapt software algorithms to suit the environment they are currently used in.

Wireless equipment manufacturers as well as network providers are pushing to have performance tests of the devices available at hand. Network providers want to recommend the user equipment (UE) with the best performance to their customers; manufacturers want to be able to compare the quality of their own UE to the one of the competitor. These comparisons should include the antenna systems, the

analog frontends, digital receiving algorithms, and baseband processing.

One of the methods proposed by 3GPP, yet a very promising one—the Decomposition Method (DM)—will be investigated further in this paper. The authors' scientific contributions described in this paper are as follows:

- (i) Analytical and numerical validation of the DM
- (ii) Validation of the method by measurement
- (iii) Detailed analysis of error sources and error bounds

Several other methods exist for performance testing of MIMO enabled UE [3–22]. A good overview is provided in [23]. Nevertheless, this paper focuses only on the DM, believing that this method can provide good and reliable results with limited effort, knowing there are limits of the method. Still, all other existing test methods also have strong sides and weaknesses too. These other performance test methods

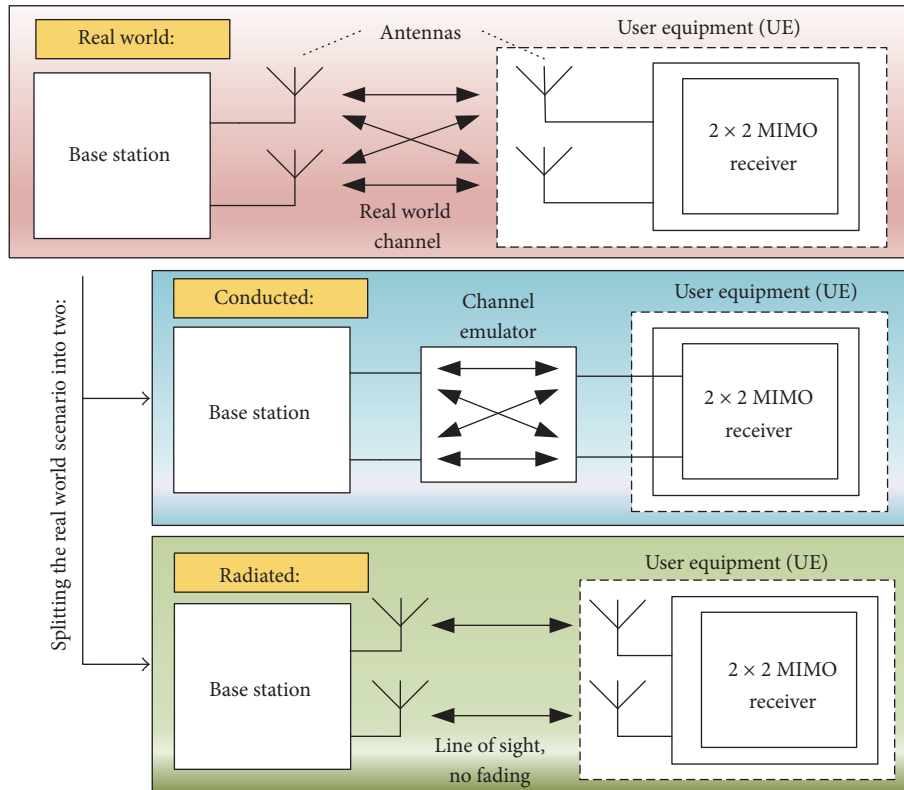


FIGURE 1: Splitting up the ideal “real world” scenario into two parts: a conducted and a radiated test setup for the downlink case of a 2×2 MIMO system [24].

will not be treated in this paper. The main advantage of the DM is that it delivers good and reliable results with limited measurement device effort and that the calibration effort of the setup is limited too.

2. Accelerated Testing of the UE by Employing the Decomposition Method

In a perfect test scenario, the performance of certain UE will be tested almost like it would be in the real world. The antenna performance and the algorithmic performance of the UE will be tested together in a single step (Figure 1, “real world”). The influence of the fading channel and the antennas performance are tested in one step. The test antennas have to be placed in many points to cover the whole test sphere (Figures 2 and 5(a)).

In every single point the test antennas are placed, the performance of the entire UE is tested. To get representative figures of merit of the UE performance on the propagation channel, lots of different channel realizations need to be examined. This results in a long measurement time, which is a big disadvantage in nowadays labs.

To accelerate the tests, the idea is to measure the time-consuming algorithmic performance tests only once (Figure 1, “conducted”). The antenna performance tests still have to be done in many positions, but if there is no fading channel, the wireless channel is static (Figure 1, “radiated”;

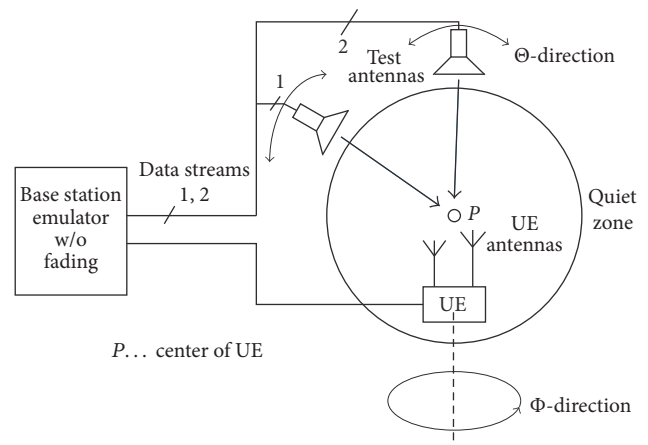


FIGURE 2: Measurement setup employing Two-Channel Method for the static radiated tests of the DM; BSE without channel emulator [25].

Figure 2) and the measurements can be done very fast, as no stochastic channel behavior has to be examined.

Later on the results of the antenna performance tests (“radiated” measurements) and the algorithmic performance tests (“conducted” measurements) are combined in a way that they are almost congruent with the “perfect” test method

(“real world” scenario), which tests all in one step. Later on the results will be combined to one single figure of merit.

This two-step approach is called Decomposition Method (DM), as it decomposes a single measurement into different single steps. The DM [24, 29] maps the “real world” test scenario (Figure 1) in a *conducted* and a *radiated* setup. The “real world” scenario is represented by the base station, its antenna system, the wireless propagation channel, and the UE antenna system. This scenario is split into two different measurement setups, which speeds up the measurement by my more than an order of magnitude. Both measurement results are used as a basis for calculating the throughput versus downlink power of the UE. The radiated measurements require an anechoic chamber with two moveable test antennas (Figures 2 and 5(a)).

2.1. Radiated and Conducted Setup. The *conducted setup* (Figure 1, “conducted”) consists of the Base-Station Emulator (BSE) connected to channel emulator, which is linked to the UE by wired connections. The conducted setup is employed for two measurements:

- (i) Using a fading channel (“channel” measurement): the channel emulator emulates the wireless propagation channel. It alters the signals transmitted by the BSE in a way a physical wireless propagation channel would do it, including multipath propagation (frequency dependent channels) and Doppler effects.
- (ii) Using an identity matrix as channel matrix—with no fading applied (“baseline” measurement): this measurement can be seen as if the UE would directly be connected to the BSE by wires. The results of the “baseline” measurement will deliver the lowest possible downlink power values for a certain data throughput rate.

These two measurements employing the conducted setup can be done in normal laboratory environment and do not require an anechoic chamber.

The *radiated setup* (Figure 1, “radiated”) employs the Two-Channel Method for the radiated over-the-air (OTA) tests [26]. It employs an anechoic chamber with two test antennas that are positionable in a Θ -plane and a turntable for UE placement that is turnable in the Φ -plane, as depicted in Figure 2. The UE is placed in the center of the anechoic chamber (quiet zone). The test antennas always have a constant distance to the UE and they are fed with signals from the BSE.

The radiated setup is static and does not contain any fading, and it is used for antenna performance tests. The two test antennas generate the EM field impinging on the UE for the radiated tests. The polarization of the test antennas can be switched independently between vertical (Θ) and horizontal (Φ) polarization. The “radiated” measurement is done with the radiated setup.

The name Two-Channel Method originates from the two downlink channels towards the UE enabled by the two test antennas (Figure 2).

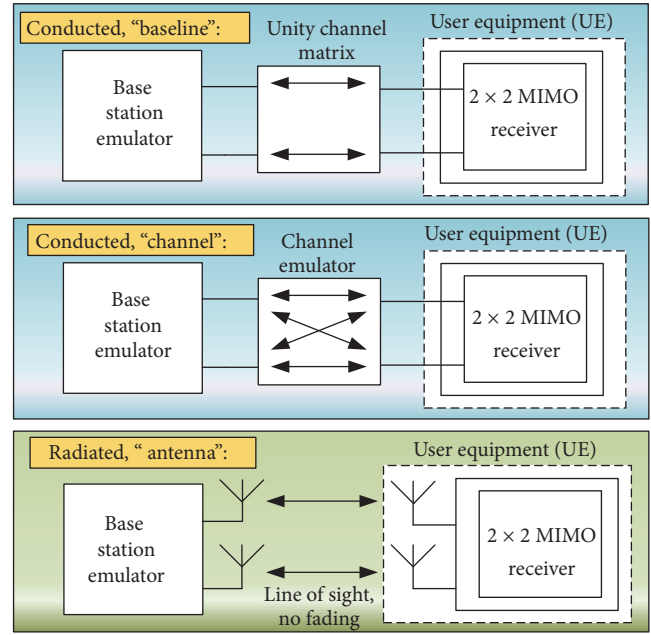


FIGURE 3: The split measurements: “baseline” and “channel” measurement have to be executed with the *conducted setup*, while “radiated” measurements employ the *radiated setup*.

2.2. The Split of the Measurements. The DM requires three performance test results of the UE: two using the “conducted” and one employing the “radiated” setup, as depicted in Figure 3:

- (1) “Baseline” measurement: *conducted* measurement without fading: the user equipment is connected to the base-station emulator by two coaxial cables, the channel matrix $\mathbf{H}_{\text{ch}} = \mathbf{I}$. The UE exhibits the best performance, it is only limited by the intrinsic UE noise. The result of the “baseline” measurement is the downlink power $P_{\text{bl}}(y)$ required for a certain relative throughput y ; see Figure 4.
- (2) “Channel” measurement: *conducted* measurement including fading: the signal is dynamically faded; Doppler shifts and spreads are applied. The ability of the device to cope with these circumstances without the UE antenna system influence is tested. The devices performance will be degraded in comparison to the “baseline” test, resulting in higher needed downlink power for a certain throughput.

The conducted faded result is $P_{\text{ch}}(y)$, where the subscript ch reflects the “channel” measurement (Figure 4).

- (3) “Antenna” measurement: *radiated* measurement without fading: the Two-Channel Method [26] is used to check the performance of the device antennas (including the receiving algorithms without its fading behavior). The radiated coupling between the test antennas and the UE is exhibited in Figure 5(a). The user has to choose a proper set of test antennas and UE positions, so-called *constellations*. These

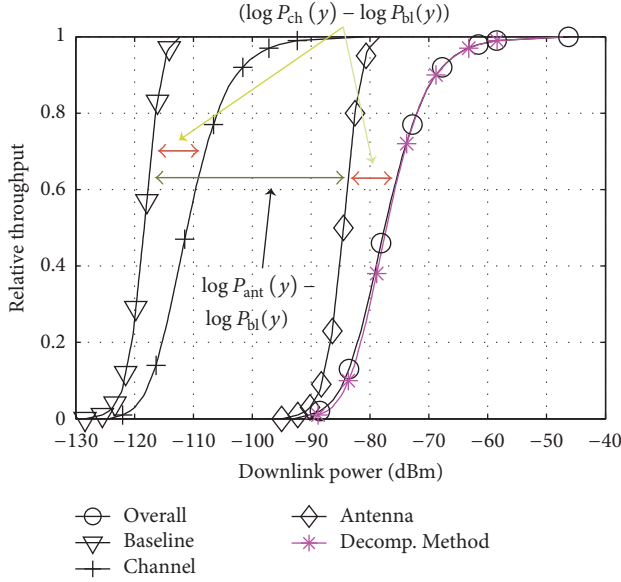


FIGURE 4: Result of the DM (relative throughput versus downlink power): adding up the logarithmic results of the “baseline”, “channel”, and “antenna” measurements. Multiply all formulas by 10 for results in dB.

constellations also include the test antenna polarization instances, which are used during the measurements [30].

The result of the measurement is $P_{\text{ant}}(y)$, where the subscript *ant* reflects the “antenna” measurement (Figure 4).

2.3. Combining the DM Results to One Figure of Merit. To get a single figure of merit, the results gathered using the DM (“baseline” result, “channel” result, and “antenna” result) have to be combined: measurement results of the DM and how to combine them [24] are shown graphically in Figure 4. Equation (2) explains itself by graphical summation and subtraction of the results:

$$10 \log P_{\text{dc}}(y) = 10 [(\log P_{\text{ant}}(y) - \log P_{\text{bl}}(y)) + (\log P_{\text{ch}}(y) - \log P_{\text{bl}}(y)) + \log P_{\text{bl}}(y)] \quad (1)$$

which leads to

$$10 \log P_{\text{dc}}(y) = 10 \log P_{\text{ant}}(y) + 10 \log P_{\text{ch}}(y) - 10 \log P_{\text{bl}}(y). \quad (2)$$

In a linear domain, the result $P_{\text{dc}}(y)$ is computed by

$$P_{\text{dc}}(y) = P_{\text{ant}}(y) \frac{P_{\text{ch}}(y)}{P_{\text{bl}}(y)}. \quad (3)$$

The DM result $P_{\text{dc}}(y)$ is ideally the same as the “real world” scenario result $P_{\text{oa}}(y)$ with the deviation d being as small as possible:

$$10 \log(d) = 10 \log(P_{\text{dc}}(y)) - 10 \log(P_{\text{oa}}(y)). \quad (4)$$

2.4. OTA Measurement Time Reduction Using the DM. The “overall” scenario (Figure 1, “real world”) with testing fading and radiated performance at once is the ideal setup for measuring the UE, delivering exact results. Using the “overall” setup for a measurement of $N = 128$ constellations takes the time t_{overall} . Measuring the UE’s behavior on the channel with block fading takes the time $t_{\text{bf_ch}}$, whether radiated for a single constellation or conducted. For the results of the static radiated “antenna” results, it takes the time $t_{\text{ant,st}}$. An example with reasonable time values from practical measurements is given:

$$t_{\text{overall}} = N \times t_{\text{bf_ch}} = 128 \times 20 \text{ sec} = 2560 \text{ sec}. \quad (5)$$

In comparison, if the measurements are split into conducted and radiated tests, the complete test time needed is t_{dc} :

$$\begin{aligned} t_{\text{dc}} &= 1 \times t_{\text{bf_ch}} + N \times t_{\text{ant,st}} \\ &= 1 \times 20 \text{ sec} + 128 \times 0.4 \text{ sec} = 71.2 \text{ sec} \end{aligned} \quad (6)$$

$$a = \frac{2560 \text{ sec}}{71.2 \text{ sec}} \approx 36.$$

This is an acceleration of the measurements of a factor $a \approx 36$! Therefore measuring the “overall” setup is impractical, and the DM with its splitted measurements shows its strengths. The author uses the “overall” results only for comparison to the DM results.

In the test, data payload is organized in subframes, for example, for the mobile communication standard LTE. The times t_{dc} and t_{overall} were measured with a data payload of 400 subframes for the static measurements and 20000 subframes for the faded measurements per measurement or constellation.

If the fading measurements require more subframes, the acceleration rate is even bigger than 36. This acceleration also reduces the anechoic chamber occupancy. The high side of the DM is that faded measurements have to be done only once, resulting in the mentioned acceleration of test speed.

3. Signal Model

The validation of the DM is the goal of this paper. We validate the hypothesis that radiated fading measurements can be split into conducted and radiated measurements and combined afterwards into a single figure of merit. The complete transmission chain is depicted in Figure 6. We can express the received signal vector for a single flat-fading subcarrier as

$$\mathbf{y} = \mathbf{C}(\mathbf{H}_{\text{ant}}\mathbf{H}_{\beta}\mathbf{H}_{\text{ch}}\mathbf{H}_{\alpha}\mathbf{s} + \mathbf{n}), \quad (7)$$

where \mathbf{s} contains the encoded random transmit symbols, $\mathbf{n} \sim \mathcal{C}\mathcal{N}\{0, \sigma_{\text{N}}^2\mathbf{I}\}$ denotes additive white symmetric complex Gaussian noise, and \mathbf{H}_{ant} is the antenna matrix, describing the angle dependent complex antenna gain. We assume linear processing employing whether ICD/ZF (inverse channel detector/zero forcing) detector with $\mathbf{C} = \mathbf{H}^{\text{P}}$ or Minimum Mean Square Error (MMSE) detector at the receiver side with $\mathbf{C} = (\mathbf{H}^{\text{H}}\mathbf{H} + \sigma_{\text{N}}^2\mathbf{I})^{-1}\mathbf{H}^{\text{H}}$, where P is the pseudoinverse and \mathbf{H} is

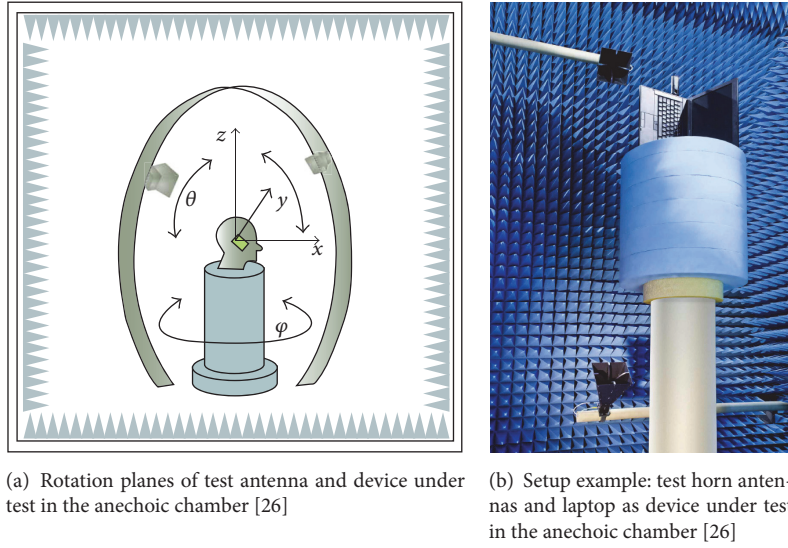


FIGURE 5: Test system setup, theoretical and practical.

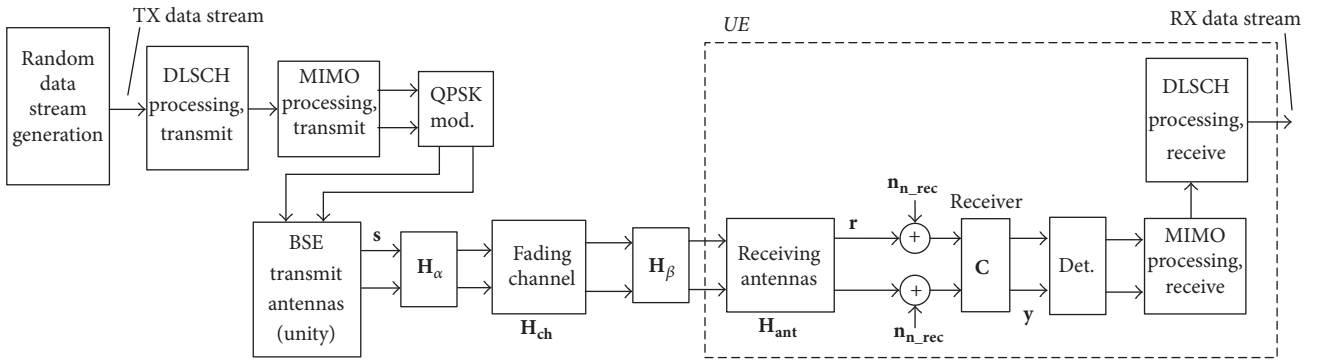


FIGURE 6: Wireless transmission system block diagram for the “overall” simulation including Downlink Shared Channel (DLSCH) processing.

the Hermitian transpose. A general channel matrix is denoted by

$$\mathbf{H} = \mathbf{H}_\beta \mathbf{H}_{ch} \mathbf{H}_\alpha \quad (8)$$

and σ_N^2 is the noise power density. The symbol estimates are demapped and decoded to the RX data stream, as depicted in Figure 6. For uncorrelated channels $\mathbf{H}_\alpha = \mathbf{H}_\beta = \mathbf{I}$ and $\mathbf{H} = \mathbf{H}_{ch}$.

3.1. Matrix Models for the Transmission Channels. In general, transmission channels with frequency flat fading have been applied. This results in 2×2 channel matrices, where each channel element h_{ij} simply represents the complex transmission gain. The authors employ an identity matrix as channel matrix for the “baseline” result

$$\mathbf{H}_{ch} = \mathbf{I}. \quad (9)$$

All channel power gains are average channel power gains. The channel power gain is represented by the expectation value of

the squared Frobenius norm of the channel matrix, which is denoted by $\|\cdot\|_F^2$ [31]

$$\begin{aligned} \mathcal{E} \left\{ \|\mathbf{H}_{ch}\|_F^2 \right\} &= \mathcal{E} \left\{ \sum_{i=1}^2 \sum_{j=1}^2 |h_{ch,i,j}|^2 \right\} \\ &= \sum_{i=1}^2 \sum_{j=1}^2 \mathcal{E} \left\{ |h_{ch,i,j}|^2 \right\}. \end{aligned} \quad (10)$$

The average power gain of the identity matrix is

$$\mathcal{E} \left\{ \left\| \begin{bmatrix} 1 & 0 \\ 0 & 1 \end{bmatrix} \right\|_F^2 \right\} = \left\| \begin{bmatrix} 1 & 0 \\ 0 & 1 \end{bmatrix} \right\|_F^2 = 2. \quad (11)$$

The average power gain of the Rayleigh fading channel has to be smaller than 2, which reflects the fact that the passive transmission channel has less power gain than the identity channel matrix. The identity channel matrix is physically represented by a wired connection between BSE and UE.

TABLE 1: Antenna matrices with different coupling and condition number.

\mathbf{H}_{ant}	κ_{\log}/dB	Coupling between signal paths
$\begin{bmatrix} 1 & 0 \\ 0 & 1 \end{bmatrix}$	0	No coupling
0.8874 $\begin{bmatrix} 1 & 0.51949 \\ 0.51949 & 1 \end{bmatrix}$	10	Light coupling
0.71414 $\begin{bmatrix} 1 & 0.9802 \\ 0.9802 & 1 \end{bmatrix}$	40	Strong coupling

The authors set the average power gain of the Rayleigh fading channel to ν :

$$\mathcal{E} \{ \|\mathbf{H}_{\text{ch}}\|_F^2 \} = \nu, \quad (12)$$

where the condition $\nu < 2$ has to be fulfilled. The authors choose $\nu = 0.4096$ arbitrarily, where arbitrary numbers do not necessarily need to be round numbers.

The condition of $\nu < 2$ gives credit to the fact that a transmission over a general channel matrix \mathbf{H}_{ch} has less energy than a transmission over coaxial cables, represented by $\mathbf{H}_{\text{ch}} = \mathbf{I}$. The second moment for a complex Gaussian distribution [32] is

$$\Sigma^2 = |h_{\text{ch},i,j}|^2 = 2\sigma^2, \quad (13)$$

where σ is the standard deviation of the complex Gaussian distributed channel parameters $h_{\text{ch},i,j}$ and the expectation value of the squared Frobenius norm of \mathbf{H}_{ch} is

$$\begin{aligned} \mathcal{E} \{ \|\mathbf{H}_{\text{ch}}\|_F^2 \} &= \sum_{i=1}^2 \sum_{j=1}^2 \mathcal{E} \{ |h_{\text{ch},i,j}|^2 \} = \sum_{i=1}^2 \sum_{j=1}^2 2\sigma^2 A^2 \\ &= N_{\text{TX}} N_{\text{RX}} 2\sigma^2 = \nu, \end{aligned} \quad (14)$$

where N_{TX} is the number of transmit antennas and N_{RX} is the number of receive antennas. With the standard deviation $\sigma = 1$, the introduced scaling factor is

$$A = \sqrt{\frac{\nu}{2\sigma^2}} = \sqrt{\frac{0.4096}{2}} = 0.2263. \quad (15)$$

All simulations in this paper employ \mathbf{H}_{ch} including the scaling factor $A = 0.2263$ and a complex Gaussian distributed channel with $\sigma = 1$.

3.1.1. Kronecker Channel Model. The general correlation matrix of a MIMO channel is defined as

$$\mathbf{R} = \mathcal{E} \{ \text{vec}(\mathbf{H}_{\text{ch}}) \text{vec}(\mathbf{H}_{\text{ch}})^H \}, \quad (16)$$

where $\text{vec}(\mathbf{H})$ stacks the matrix elements in a vector. In this work we use the simplified correlation based Kronecker channel model [33, 34]

$$\mathbf{R} = \mathbf{R}_{\alpha} \otimes \mathbf{R}_{\beta}, \quad (17)$$

where the receiver and transmitter correlation matrix [34] are denoted by

$$\mathbf{R}_{\alpha} = \begin{bmatrix} 1 & \alpha \\ \alpha & 1 \end{bmatrix}, \quad (18)$$

$$\mathbf{R}_{\beta} = \begin{bmatrix} 1 & \beta \\ \beta & 1 \end{bmatrix}, \quad (19)$$

respectively. The off-diagonal elements α and β define the cross coupling. We use the following parameterization of α and β as proposed in [33, 35]:

- (i) Uncorrelated: $\alpha = 0$ and $\beta = 0$.
- (ii) Medium correlation: $\alpha = 0.3$ and $\beta = 0.9$.
- (iii) High correlation: $\alpha = 0.9$ and $\beta = 0.9$.

Random correlated channel realizations are computed according to

$$\mathbf{H}_{\text{ch}} = \mathbf{R}_{\beta}^{1/2} \mathbf{H}_{\text{w}} \mathbf{R}_{\alpha}^{1/2}, \quad (20)$$

where \mathbf{H}_{w} denotes a MIMO matrix with independent and identically distributed (i.i.d.) complex Gaussian entries $\mathbb{C}\mathcal{N}\{0, 1\}$ with zero mean and variance one.

3.1.2. Antenna Matrices. We assume no coupling between the base-station antennas. The DUT antenna coupling is denoted by \mathbf{H}_{ant} . It is calculated using the complex E -field pattern [26]:

$$\mathbf{H}_{\text{ant}}(\Omega_1, \Omega_2, p, q) = \begin{bmatrix} E_{p1}(\Omega_1) & E_{q1}(\Omega_2) \\ E_{p2}(\Omega_1) & E_{q2}(\Omega_2) \end{bmatrix}, \quad (21)$$

$\{p, q \in \Theta, \Phi\}$,

where E denotes the complex E -field pattern of the receiving antenna 1 or 2. We denote the polarization instances of the test antennas with $\{p, q\}$. These polarization instances $\{p, q\}$ can be in Φ - or in the Θ -plane.

Matrix \mathbf{H}_{ant} is shown in Table 1 for three exemplary antennas with different condition numbers κ_{\log} , namely, for fully decoupled antennas ($\kappa = 0$ dB) to strongly coupled antennas ($\kappa = 40$ dB). The antenna matrix \mathbf{H}_{ant} is normalized to a squared Frobenius Norm (SQFN) of 2:

$$\|\mathbf{H}_{\text{ant}}\|_F^2 = \sum_{i=1}^2 \sum_{j=1}^2 |h_{\text{ant},ij}|^2 = 2, \quad (22)$$

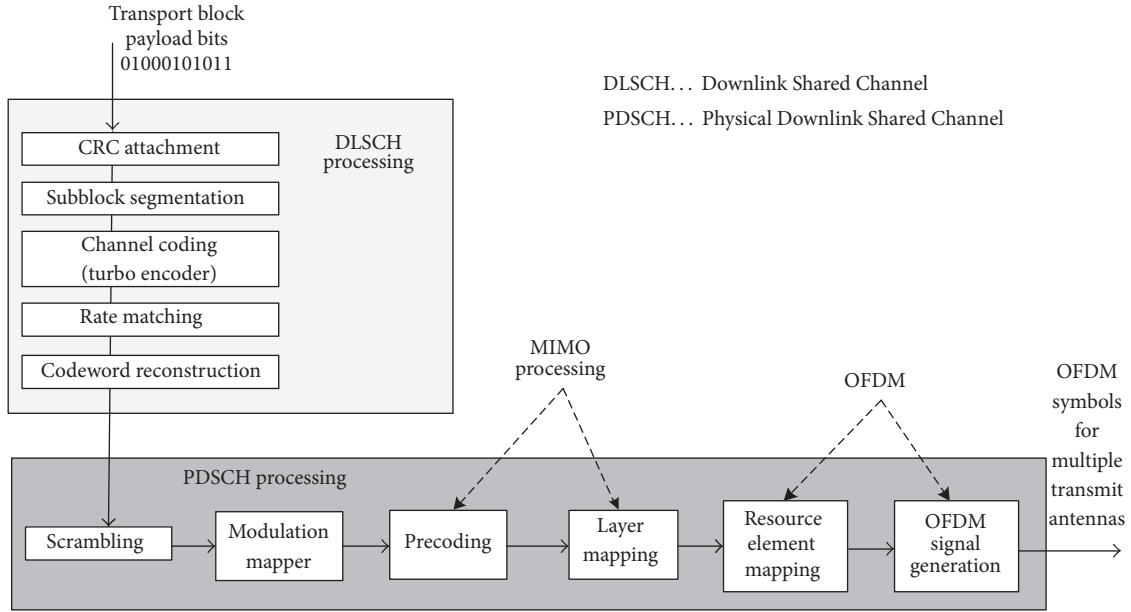


FIGURE 7: LTE signal processing block diagram for transmit diversity and spatial multiplexing (MIMO) [27] in the transmitter.

which corresponds to the power gain of an identity matrix, shown in (11). The reason is that results can be compared easily, if the power gain is the same for all \mathbf{H}_{ant} . The antenna condition number in linear terms

$$\kappa_{\text{lin}} = \frac{\sigma_{\text{max}}}{\sigma_{\text{min}}} \quad (23)$$

is the ratio of the largest to the smallest eigenvalue of the antenna matrix $\mathbf{H}_{\text{ant}}(\Omega_1, \Omega_2, p, q)$ (23).

The bigger κ_{lin} is, the worse the matrix conditioning is. For visualization purposes the authors define

$$\kappa_{\text{log}} = 20 \log_{10}(\kappa_{\text{lin}}). \quad (24)$$

The identity antenna matrix corresponds to fully decoupled antennas, with $\kappa_{\text{log}} = 0$ dB. Increasing coupling between the antennas provide antenna matrices with higher condition numbers.

3.2. LTE as a Showcase for MIMO Enabled Communication Standards. The wireless mobile communication standard Long Term Evolution (LTE) is a common use case for the application of the DM. Therefore main elements of the standard are used for the numerical validation.

3.2.1. Modeling of the Physical (PHY) Layer for Downlink/Transmitter Side. Figure 7 shows a block diagram of LTE transmitter [27]. User payload is segmented into blocks; then channel coding with *rate matching* is applied. LTE employs turbo coding for channel coding, and code blocks are concatenated to create codewords. The user data is *scrambled*, which is an operation where the user data is convolved with a pseudo random sequence resulting in the scrambled bit stream. In the *modulation mapper* the bit stream is mapped to a certain complex in *phase/quadrature phase* (I/Q) modulation scheme, like

- (i) QPSK (*Quadrature Phase Shift Keying*), mapping 2 bits to one symbol
- (ii) 16 QAM (*16-Quadrature Amplitude Modulation*), mapping 4 bits to one symbol
- (iii) 64 QAM (*64-Quadrature Amplitude Modulation*), mapping 8 bits to one symbol

In the *MIMO processing* the complex modulated data are shaped for the different MIMO subchannels according to the available antennas and the transmit mode. The *Orthogonal Frequency Division Multiplexing* (OFDM) processing takes care of the data placement in the domains frequency and time (*Resource Element (RE) Mapping* and *OFDM signal generation*). The data are amplified and transmitted by the multiple antennas.

3.2.2. Channel Estimation Errors. Another part of the investigations is to have a closer look on *channel estimation errors*. In consideration of receiver types like the ICD/ZF or the MMSE, it is assumed that the transmission channel is perfectly known. The following investigations also consider imperfect knowledge of the channel taking into account the length of the pilot signals that are used for channel estimation. Mengali proposed a method to compute the variance of the estimation error for QPSK. The error follows a normal distribution with a first moment equaling zero and variance [36]

$$\sigma_{\text{est_err}}^2 = \frac{1}{L} \frac{1}{P/N_0}, \quad (25)$$

where L is the length of the pilot sequence and $P/(BN_0)$ is the symbol energy to the noise energy (SNR). The channel estimation in LTE is executed over 19 OFDM subcarriers and

10 subframes, each containing 2 slots. Every slot contains one symbol for estimation. This results in

$$L = 19 \text{ subcarriers} \times 10 \text{ subframes} \times 2 \text{ slots} \times 1 \text{ symbol} = 380 \text{ symbols} \quad (26)$$

per estimation [3, 35]. With (25) and (26), the channel estimation error variance $\sigma_{\text{est_err}}^2$ can be calculated as

$$\sigma_{\text{est_err}}^2 = \frac{1}{380} \frac{1}{P/N_0}. \quad (27)$$

Equation (25) shows the dependency of the estimation error on the symbol energy to noise energy P/N_0 . The equation is valid for flat-fading and time invariant channels.

4. DM Validation: MIMO Channel Capacity Approach

4.1. Validation Procedure. As an additional step, the authors employ the MIMO channel capacity expression; therefore a generic view can be achieved in the investigations. This approach imposes the use of a receiver of general type working close to or at the Shannon bound. For the investigations a 2×2 MIMO transmission system with two uncorrelated data streams and symbol energy of P/N_T per stream is chosen. The symbol energy is equally distributed over the two transmission paths. The signal covariance matrix of the symbols

$$\mathbf{R}_{ss} = \frac{P}{N_T} \mathbf{I}_{N_T} \quad (28)$$

is a diagonal matrix in this case [37], where N_T is the number of transmit antennas. The sum of the main diagonal elements of \mathbf{R}_{ss} is the symbol energy [37]:

$$\text{trace}(\mathbf{R}_{ss}) = P. \quad (29)$$

Using these assumptions, the rate of the MIMO channel simplifies to [37]

$$C = \mathcal{E} \left\{ \log_2 \det \left(\mathbf{I}_{N_R} + \frac{P}{N_T N_0} \mathbf{H} \mathbf{H}^H \right) \right\}, \quad (30)$$

where N_R is the number of receiving antennas, \mathbf{H} is the channel matrix, the trace operator denotes the sum of the main diagonal elements of a matrix, \mathbf{I}_{N_R} is the identity matrix with dimension $N_R \times N_R$, \mathcal{E} is the expected value, and \det is the determinant, respectively. For the sake of simplicity, the validations in this section use the absolute throughput rate C and not the relative throughput rate γ as in Section 2.3. In both cases the validity of the Decomposition Method can be shown.

Equation (30) can also be expressed in terms of the eigenvalues of $\mathbf{H} \mathbf{H}^H$ employing the eigendecomposition [38]

$$C = \mathcal{E} \left\{ \log_2 \det \left(\mathbf{I}_{N_R} + \frac{P}{N_T N_0} \mathbf{Q} \mathbf{\Lambda} \mathbf{Q}^H \right) \right\} \quad (31)$$

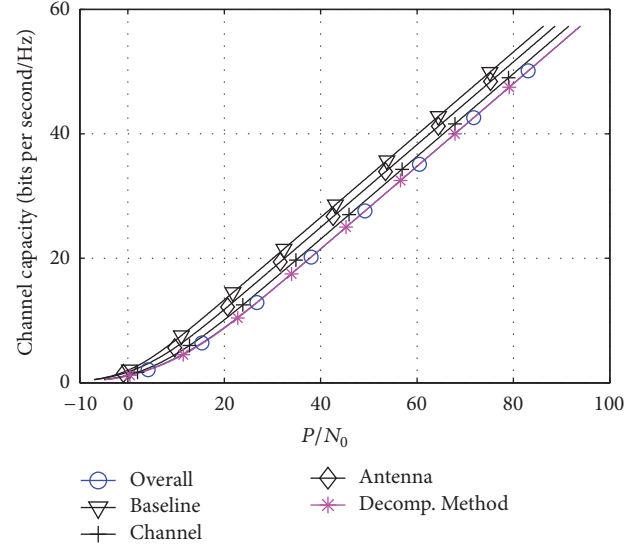


FIGURE 8: Absolute channel capacity per bandwidth versus P/N_0 using DM; $\kappa_{\text{Hant}} = 10$ dB. All measurements including the ideal and the real result are exhibited. “Overall” and DM results are almost overlapping.

reducing to

$$C = \mathcal{E} \left\{ \log_2 \det \left(\mathbf{I}_{N_R} + \frac{P}{N_T N_0} \mathbf{\Lambda} \right) \right\}, \quad (32)$$

where $\mathbf{\Lambda}$ contains the nonnegative eigenvalues on its main diagonal [37, 39].

Using the eigenvalue matrix $\mathbf{\Lambda}$ and its elements λ_i , the expected (ergodic) rate can also be written as [39]

$$C = \mathcal{E} \left\{ \sum_{i=1}^{N_R} \log_2 \left(1 + \frac{P}{N_T N_0} \lambda_i \right) \right\}. \quad (33)$$

We use (30) to calculate the ergodic rate for the three DM scenarios and the overall scenario numerically. The channel matrix is modified according to the different steps of the DM as follows:

- (i) “Overall” transmission scenario (oa): $\mathbf{H} = \mathbf{H}_{\text{ant}} \mathbf{H}_{\text{ch}}$.
- (ii) “Antenna” transmission scenario (ant): $\mathbf{H} = \mathbf{H}_{\text{ant}}$.
- (iii) “Channel” transmission scenario (ch): $\mathbf{H} = \mathbf{H}_{\text{ch}}$.
- (iv) “Baseline” transmission scenario (bl): $\mathbf{H} = \mathbf{I}$.

The required transmit energy P is a function of the channel rate C (for fixed noise power spectral density N_0) for a given set of channel matrices, providing $P_{\text{oa}}(C)$, $P_{\text{ant}}(C)$, $P_{\text{ch}}(C)$, and $P_{\text{bl}}(C)$. Inserting these results in (2) and (4) we can compute the deviation d .

Figure 8 exhibits the absolute throughput rate C versus P/N_0 for different antenna correlation condition numbers ($\kappa = 10$ dB). In theory, the channel rate C does not have a limit, as long as P/N_0 is rising. In practical systems the throughput will always saturate at the maximum data rate related to the chosen modulation and coding scheme of a

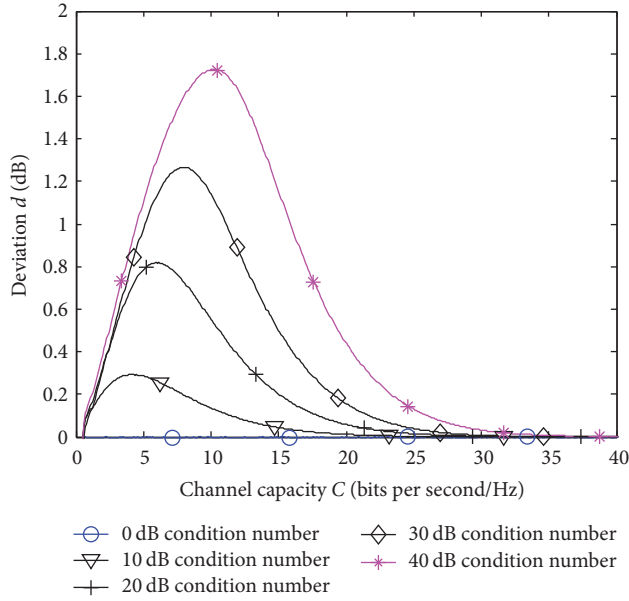


FIGURE 9: Deviation d versus absolute channel capacity C using DM for $\kappa_{H_{\text{ant}}} = \{0 \text{ dB}, 10 \text{ dB}, 20 \text{ dB}, 30 \text{ dB}, 40 \text{ dB}\}$.

wireless transmission. Figure 8 also shows that the DM result does not deviate at $\kappa = 0$ dB. The deviation d , as defined in (4), is increasing with rising κ and is also depending on P/N_0 .

The deviation d versus the channel capacity C is depicted in Figure 9. The plots show d over C for $\kappa \in \{0 \text{ dB}, 10 \text{ dB}, 20 \text{ dB}, 30 \text{ dB}, 40 \text{ dB}\}$. For $\kappa_{\log} = 0$ dB, the deviation d is zero, and the DM works perfectly. For rising κ , d is increasing and the maximum of d shifts towards bigger P/N_0 and decreases slower than at lower values of κ . Nevertheless, even at a very bad conditioned antenna matrix with = 40 dB, the maximum deviation d is below 1.72 dB.

4.2. Conclusion on the Channel Capacity Approach. The authors validate the DM by using the MIMO channel capacity formula. MIMO channel capacity curves are simulated and overlaid using the DM. This section compares the “overall” results to the “DM” results by showing the occurring deviations d . For the given antenna condition numbers the DM works within the error margin given in Figure 9. This error margin of d lies within the error margin given by measurement uncertainties in practical OTA measurements [40]. Dozens of measurement uncertainty sources are listed in [41, 42]: mismatch of transmitter chain, insertion loss of transmitter chain, influence of the probe antenna, uncertainty of BSE power level, statistical uncertainty of throughput measurement, fading flatness within the LTE band, uncertainty of the network analyzer, and instability of cable connections just to name a few.

5. DM Validation: Numerical Analysis Approach

5.1. Introduction. To validate the DM from another perspective, the authors choose the numerical link level simulation

of a wireless MIMO transmission system. The DM is intended for testing general UE employing MIMO antenna technology. An important point is to investigate the validity of the DM for the use with LTE devices. It will be a main application of the method. As the number of employed signal processing elements for LTE is high, this paper focuses on the most important blocks of the transmission in the PHY layer for the simulation and numerical validation.

The authors again realize a transmission using the block diagrams in Figure 6 for the numerical simulation of the transmission. They discuss the results of this transmission system and present the validation of the DM under the given conditions.

5.2. Concept of the Numerical Simulations. As LTE is a complex transmission protocol containing a lot of different functionality blocks, it is necessary to focus on the blocks that might be influential on the DM. All investigations are done with flat-fading wireless transmission channels. If problems show up already with the simple model of flat-fading channels, all scenarios containing more complex transmission models including tapped delay channel models and OFDM schemes will also have a problem.

A wireless system, employing an OFDM scheme, splits the complete channel bandwidth of the frequency dependent channel in many narrow-band channels that are assumed to be of flat-fading nature. In the following investigations, the authors deal with one of these small flat-fading OFDM channels. This has the consequence that it is not necessary to simulate all the OFDM channels. All steps in the DL-SCH block (Figure 7) are implemented, as well as the *modulation mapper* and the *MIMO processing blocks*. The elements in the *Physical Downlink Shared Channel* (PDSCH) like scrambling, RE mapping, and OFDM processing have been omitted, as the authors expect minor influence on the results when employing frequency flat transmission channels.

5.3. Simulation Setup Configuration and Figures of Merit. The parameters for the simulation setup and the necessary figures of merit (FOMs) are introduced in this section, as well as how they can be calculated. The block diagram of the transmission systems in Figure 6 eases the understanding of the parameters and the FOMs.

5.3.1. Transmission Data Block Size and Subframe Error Rate (SFER). The transmitted data streams have a length of 2^8 bits per realization of the channel matrix \mathbf{H}_{ant} . The transmitted (TX) bit stream is compared to the received bit stream (RX). This is done with a test window size of 2^4 bits, so-called *subframes* (SFs). If the RX subframe completely matches the TX subframe, it is recognized as correct. If there are one or more bits wrong, the complete subframe is rated to be incorrect. The mathematical formulation of the Subframe Error Rate (SFER) is

$$\text{SFER} = \frac{\text{number of correctly received SFs}}{\text{number of all transmitted SFs}}, \quad (34)$$

and it ranges from 1 (no subframe (SF) transmitted correctly) to 0 (all SFs transmitted correctly).

5.3.2. *Relative Throughput (RTP)*. The relative throughput is

$$\text{RTP} = 1 - \text{SFER}. \quad (35)$$

It ranges from 0 (no SF transferred correctly) to 1 (all SFs transferred correctly).

Downlink Power, Bandwidth, and Noise. The downlink power used for the simulation ranges from -130 dBm to -50 dBm. It is always related to a subcarrier bandwidth of $B = 15$ kHz. The noise energy is

$$\begin{aligned} N_0 &= -174 \text{ dBm} + 10 \log_{10}(B) + N_f \\ &= -174 \text{ dBm} + 10 \cdot \log_{10}(15 \text{ kHz}) + 5.2 \text{ dB} \\ &= -127 \text{ dBm}, \end{aligned} \quad (36)$$

where $N_f = 5.2$ dB is the noise figure of the UE employed for the measurements in this paper; white noise is assumed.

5.3.3. *Simulation Parameters and Number of Realizations*. The numerical simulations employ a variation of settings:

- (i) Detector type: ICD/ZF or MMSE
- (ii) Ideal or nonideal channel estimation
- (iii) DLSCH processing enabled/disabled
- (iv) Low, medium, or high correlation matrices \mathbf{H}_α and \mathbf{H}_β
- (v) Receive-antenna condition number κ

The authors implemented the transmission chain following the block diagram in Figure 6 for the simulations with DLSCH processing without DLSCH processing.

A *realization* is a certain transmission system instance employing one set of stochastic parameters, like channel parameters or channel estimation errors. The authors executed all simulations with 5000 realizations of the channel matrix \mathbf{H}_{ch} . They averaged the throughput of all realizations linearly for each downlink power value throughout this paper. This averaged throughput is displayed in the result throughput versus downlink power curves. Every realization employs a new set of transmission data blocks.

5.4. Results

5.4.1. *Relative Throughput versus Downlink Power Curves*. Figure 10 exhibits an example for a set of simulation result curves with relative throughput over downlink power. The mentioned result figure employs an antenna condition number of $\kappa = 40$ dB and other different transmission parameters, as mentioned in the caption of the figures.

The exemplarily taken graph shows all three necessary curves to calculate the DM result: the “baseline”; “channel”; and “antenna” curves. The DM result and the “overall” result are also depicted. If the DM works well within the given parameters, the DM result and the “overall” result overlap, as it is the case in Figure 10. The quantitative measure of how well the DM works is the deviation d . It shows the

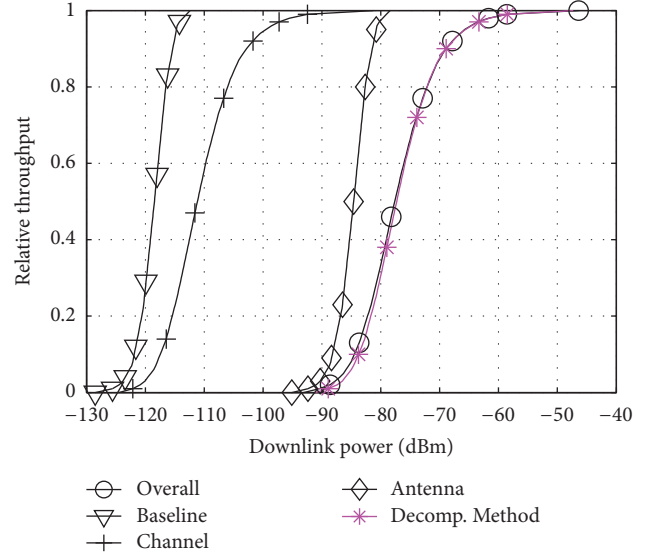


FIGURE 10: Simulation result example: downlink power versus relative throughput; ICD/ZF receiver, DLSCH processing on, ideal channel estimation, correlation low, and antenna condition number 40 dB.

difference between the actual value (DM result) and the ideal value (“overall” result), as depicted in (4). The authors simulated the different transmission scenarios for a wide range of parameters.

All downlink power values versus RTP show the same “baseline” result curve, which exhibits the best performance a transmission system can reach. The higher the performance is, the more a certain throughput can be received with less downlink power. The BSE is directly connected to the receiver: $\mathbf{H}_\beta \mathbf{H}_{\text{ch}} \mathbf{H}_\alpha = \mathbf{I}$.

The slope of the “channel” curve is less steep in comparison to the “baseline” curve, because of the complex normal distribution of the channel parameters in a general \mathbf{H}_{ch} matrix.

In the case that the receiving antenna matrix is an identity matrix and uncorrelated ($\kappa = 0$ dB), the “antenna” result overlaps with the “baseline” result. The “antenna” simulations employ $\mathbf{H}_\beta \mathbf{H}_{\text{ch}} \mathbf{H}_\alpha = \mathbf{I}$. The overlapping of the “overall” curve and the DM curve is the ideal case, and in this case the DM works perfectly.

As the antenna elements start to be correlated (condition number κ of the antenna matrix $\mathbf{H}_{\text{ant}} > 0$ dB), the receiver performance is degraded. This degradation leads to a result curve (the “antenna” result curve) that is a right shifted version of the “baseline” result curve, as shown in Figure 10. This right-shift means that the receiver needs more signal downlink power to reach the same throughput as with an uncorrelated channel. The reason for this behavior is that the receiver cancels the influence of the channel, but it also enhances the existing intrinsic noise, generated by the RF front-end of the UE.

The more the receiving antennas are coupled, the worse the conditioning of the antenna matrix is (indicated by κ). Looking at Figure 10, the antenna matrix condition number

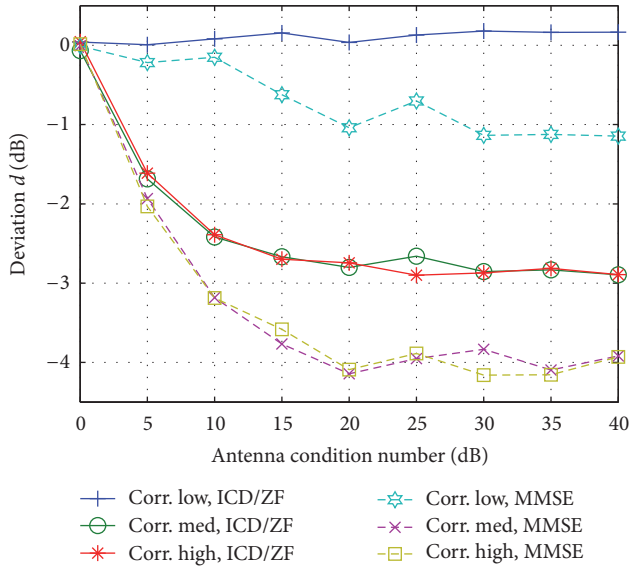


FIGURE 11: Deviation d versus antenna condition number for DLSCH processing on, nonideal channel estimation; low, medium, and high channel correlation; ICD/ZF and MMSE receiver.

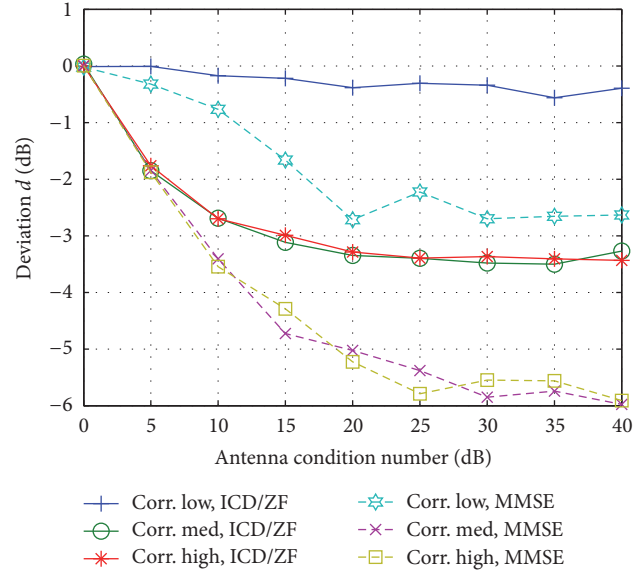


FIGURE 12: Deviation d versus antenna condition number for DLSCH processing off, nonideal channel estimation; low, medium, and high channel correlation; ICD/ZF and MMSE receiver.

= 40 dB. For a relative throughput of 0.7, the “baseline” setup needs a downlink power of -117 dBm, while the “antenna” setup needs -83 dBm, which is a difference of 34 dB.

So to say, the degradation through the correlation of the receiving antennas results in a degraded performance of the whole transmission system. The influence of the different simulation parameters will be discussed in the following section.

5.4.2. Influence of the Transmission System Parameters on the Deviation d . The authors show the influence of the simulation parameters on the deviation d . These results are exhibited in Figures 11–16 and the authors will discuss them elaborately. The different simulation parameters are

- (i) DLSCH processing on/off
- (ii) ideal/nonideal channel estimation
- (iii) low, medium, and highly correlated channel parameters

These figures show the investigation of the deviation d versus the antenna condition number κ for this set of parameters. They are arranged in different ways to highlight certain ways of behavior. Certain curves are exemplarily taken to explain a certain way of behavior. Some facts are mentioned twice, to ease understandability. Please note that the depicted deviations d are *maximum* values that will not be reached in practice, when a real antenna system is employed.

Influence of the Condition Number κ . Generally speaking, the absolute deviation $|d|$ rises with rising antenna condition number κ . Figure 11 is taken exemplarily to show this behavior, which appears in all simulations. The absolute deviation starts to grow rapidly and settles more or less at = 20 dB. The employed simulation parameters for the deviation

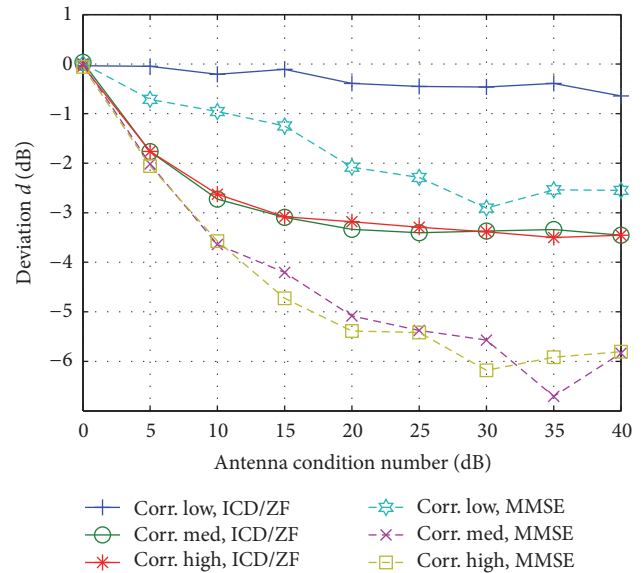


FIGURE 13: Deviation d versus antenna condition number for DLSCH processing off, ideal channel estimation; low, medium, and high channel correlation; ICD/ZF and MMSE receiver.

results in Figure 11 are as follows: DLSCH processing on, nonideal channel estimation; low, medium, and high channel correlation; ICD/ZF and MMSE receiver.

It is interesting to see that the DM works almost perfectly for low correlation and the ICD/ZF receiver. In comparison, the MMSE receiver causes an approximate maximum deviation $d = -1$ dB at low correlation. With rising correlation, both receiver types, MMSE and ICD/ZF, cause bigger absolute deviation $|d|$. The value of $|d|$ is greater for MMSE than for ICD/ZF in general.

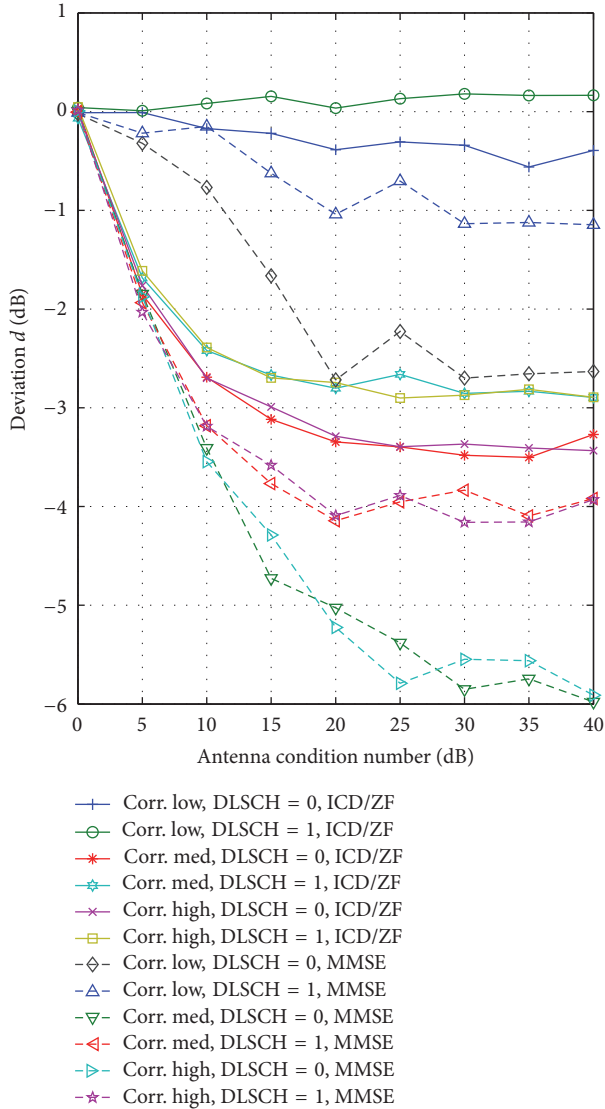


FIGURE 14: Deviation d versus antenna condition number for DLSCH processing on/off, nonideal channel estimation; low, medium, and high channel correlation; ICD/ZF and MMSE receiver.

Influence of the Channel Correlation. Figure 11 also points out the differences of the different channel correlations *low*, *medium*, and *high*. DLSCH processing is applied and the channel estimation is nonideal. The DM works almost perfectly for ICD/ZF receivers at low correlations.

In contrast, the receiver type MMSE delivers mentionable deviations already at low channel correlations. As soon as channel correlation becomes medium or high, the absolute deviation $|d|$ increases. The deviation $|d|$ is always bigger for the MMSE receiver than for the ICD/ZF receiver. Figure 12 shows the same trends but with higher absolute deviation $|d|$ (no DLSCH processing is applied).

Influence of DLSCH Processing on/DLSCH Processing off. Figure 16 depicts the differences of the deviation d , between

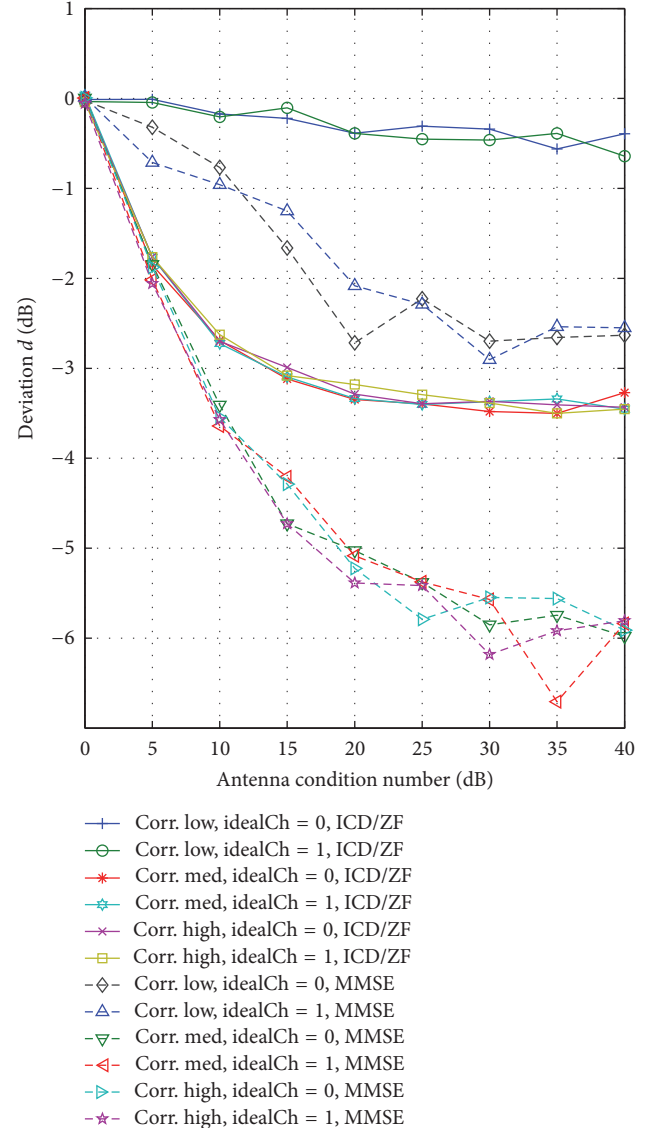


FIGURE 15: Deviation d versus antenna condition number for DLSCH processing off, nonideal/ideal channel estimation; low, medium, and high channel correlation; ICD/ZF and MMSE receiver.

DLSCH processing being turned on and off for ideal channel estimation. The channel correlations are again low, medium, and high.

In contrast, Figure 14 exhibits the results for DLSCH processing being turned on and off for nonideal channel estimations. The main message of both graphs is that if DLSCH processing is turned on, the abs. deviation $|d|$ becomes smaller for all three correlation types and two receiver types (MMSE and ICD/ZF), in comparison to DLSCH processing turned off.

This is true for all channel correlation types: low, medium, and high. This is the reason why the DM is very suitable for LTE performance tests, as LTE *always* uses DLSCH processing. The influence of the channel estimation on the results of d is very small.

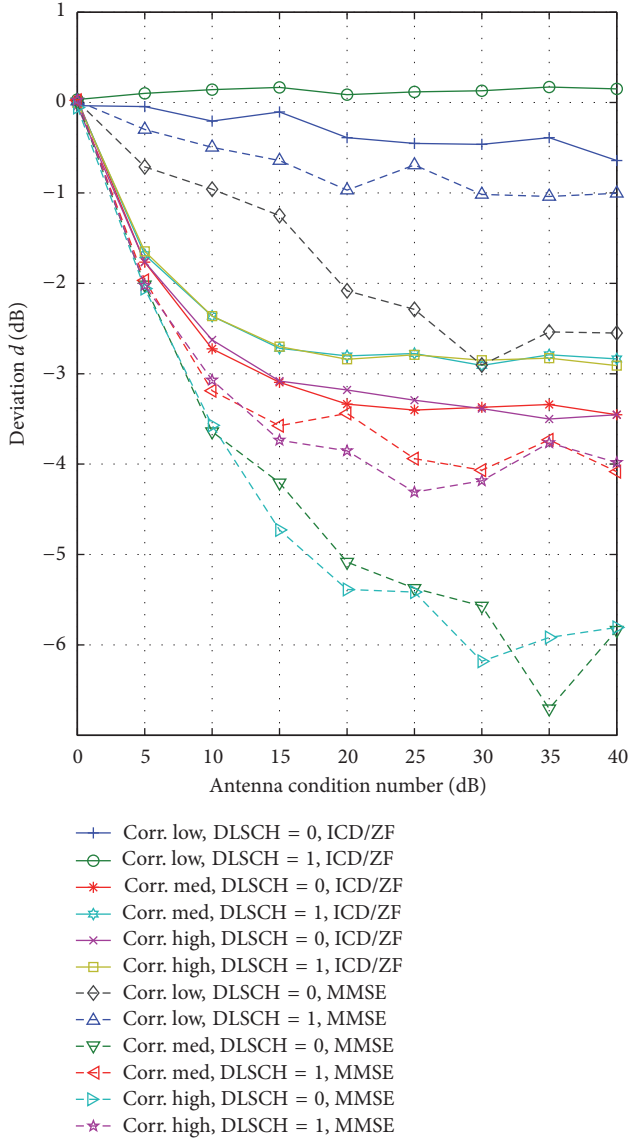


FIGURE 16: Deviation d versus antenna condition number for DLSCH processing on/off, ideal channel estimation; low, medium, and high channel correlation; ICD/ZF and MMSE receiver.

Summarizing, the following facts can be pointed out:

- (i) The DM suits well its purpose, the performance testing of MIMO enabled wireless UE, especially for low correlation channels, and it delivers small deviations d for both receiver types: ICD/ZF and MMSE.
- (ii) In general, if the antenna condition number κ is rising, the absolute deviation $|d|$ rises.
- (iii) If channels correlations are medium or high, the absolute deviation $|d|$ is bigger than that for low correlation channels.
- (iv) The DM delivers better results with the ICD/ZF receiver in comparison to the MMSE receiver for all channel correlations.

- (v) The influence of the channel estimation error is negligible in the case of LTE pilot sequence length as a reference example.
- (vi) If a transmission system employs DLSCH processing, the DM performs better compared to being without it. This behavior makes it very suitable for performance tests with LTE, as it always uses DLSCH processing.
- (vii) Rising deviation occurs for antennas with very poor behavior, but manufacturers will strongly avoid such poor designs as it results in a significantly reduced MIMO system performance.

All diagrams with deviation d versus antenna condition number κ show *maximum* errors, which will not occur in practice. The reason is that the condition number of the antenna matrix \mathbf{H}_{ant} is different for every constellation. Therefore the authors execute investigations with a practical antenna set and the mean deviation \bar{d} in the following chapter.

5.4.3. *Investigating the Deviation d Employing LTE Reference Antennas.* The deviation d versus condition number κ graphs tend to overestimate practically arising deviations, as UE manufacturers do not intentionally build very poor performing antenna systems. For the reason of better visualization the authors investigated the distribution of the deviation d with LTE reference antennas with designated performances.

The company *Motorola Mobility* designed LTE reference antennas for the purpose of interlaboratory measurement campaigns executed in the COST 1004 actions [28]. The printed circuit board contains the antennas and a metal housing. Different UE can be placed inside the metal cavity. The UE can be connected to the external reference antenna elements with coaxial cables, and the internal antennas are deactivated. A picture of the reference antenna is exhibited in Figure 17.

It is available in three different performance types:

- (i) “Good” performance
- (ii) “Nominal” performance
- (iii) “Bad” performance

The performance naming refers to the coupling of the antenna elements in the different reference antenna versions. This coupling is expressed with condition number κ , which is different for every constellation. A constellation contains test antenna positions and polarization, as well as UE placement.

The authors use the 128 constellations [30] for statistical investigations on the logarithmic antenna condition numbers κ . Every single constellation delivers a certain κ , which can be calculated employing the E -field antenna pattern as shown in Section 3.1.2. Figure 18 shows the distribution of κ for the 128 constellations for all three antenna types. Also the mean logarithmic value of the condition number

$$\bar{\kappa} = \frac{\sum_{i=1}^N \kappa_i}{N} \quad (37)$$

is shown in the graphs, where N is the number of constellations (e.g., $N = 128$) and κ_i is the logarithmic antenna condition number of a constellation i .

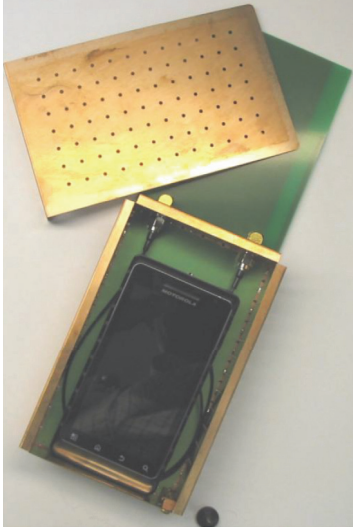


FIGURE 17: LTE reference antenna for UE with two antennas designed by Motorola Mobility for band 13 (751 MHz), with a printed circuit board carrying a closed metal cavity for the UE, two printed antennas, and connection cables [28].

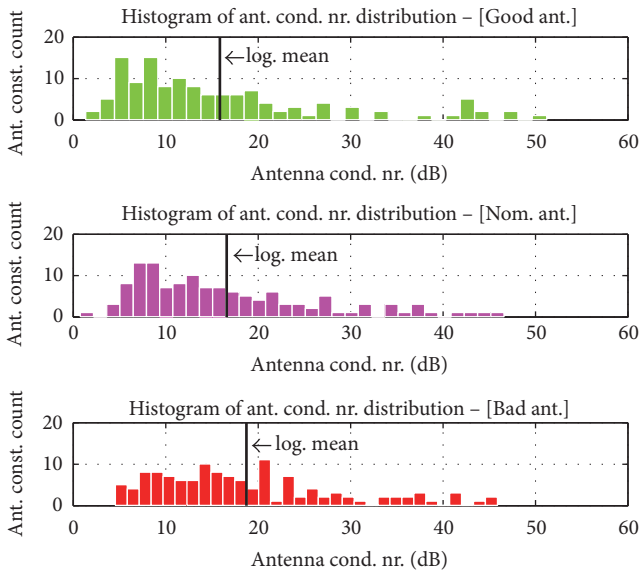


FIGURE 18: Distribution of the antenna condition number and mean logarithmic condition number of the “Good”; “Nominal”; and “Bad” reference antennas.

The reference antennas behave as they are named. Going from “Good” to “Bad”, $\bar{\kappa}$ rises:

- (i) “Good” antenna: 15.86 dB
- (ii) “Nominal” antenna: 16.6 dB
- (iii) “Bad” antenna: 18.72 dB

Table 2 summarizes the *mean logarithmic deviations* \bar{d} for the same parameter variation as in Section 5.4.2 for a relative throughput of 70%:

- (i) DLSCH processing on/off

- (ii) Ideal/nonideal channel estimation
- (iii) Low, medium, and high channel correlations

The mean logarithmic deviation is

$$\bar{d} = \frac{\sum_{i=1}^N d_i}{N}, \quad (38)$$

where N again is the total number of constellations and d_i is the deviation at the constellation i . The DM can be validated for all three types of antennas within a $|\bar{d}|$ of 4.69 dB. This maximum of the averaged values of \bar{d} lies below the peak value of $|d|$, as shown in Figure 15. In the case UE employs LTE, DLSCH processing is always applied. In this case the absolute mean logarithmic deviation $|\bar{d}|$ will always be below 3.57 dB for all antenna condition numbers. If LTE UE is tested only with low correlation of channels, the method works almost perfectly with $|\bar{d}|$ below 0.29 dB.

Finally, the following can be pointed out:

- (i) The mean deviation $|\bar{d}|$ is *always* below the maximum of the absolute deviations $|d|$. In the case of ICD/ZF receiver, low correlated channel, DLSCH processing, and nonideal channel measurement even for the “Bad” antenna it will be only 0.1 dB.
- (ii) In the practical case of rather well conditioned antenna matrices and DLSCH processing applied, the method works very well.
- (iii) Comparing the receiver types, the MMSE receiver causes higher mean deviations \bar{d} than the ICD/ZF receiver.
- (iv) The investigations exhibit that the mean deviation \bar{d} decreases when going from antenna type “Bad” to antenna type “Good.”
- (v) If a very poor antenna system is measured, there is a possibility of calibrating the system, as the deviation d is static.
- (vi) The DM is an innovative method to deliver fast and reliable performance test results.

6. Validation of the DM by OTA Measurements of UE

6.1. Measurements. The authors conducted measurements with a commercial LTE device, namely, the *Sony Xperia* smartphone, for a round-robin campaign for *radio area network group 4* (RAN4) of 3GPP. They tested the UE in an anechoic chamber using the “Good” antenna, employing the setup in Figure 2 at 128 constellations [30]. The authors measured the “DM” results and the “overall” results of the *Sony Xperia* smartphone with different transmission channel models than in the simulation to calculate the deviation d .

Figure 19 shows the experimental results of the distribution of the deviation d . The authors determined the deviation d for the different transmission channel models for all 128 constellations. The results of d for the different channel models are color coded in the diagram.

TABLE 2: Mean logarithmic deviations \bar{d} at 70% relative throughput using LTE reference antennas “Good”; “Nominal”; and “Bad” with parameters: channel correlation type, DLSCH processing, and channel estimation.

Receiver type	Corr.	DLSCH proc.	ch. est.	Deviation \bar{d} for ref. ant./dB		
				“Good”	“Nominal”	“Bad”
ICD/ZF	Low	Off	Ideal	-0.26	-0.26	-0.29
ICD/ZF	Low	Off	Nonideal	-0.19	-0.23	-0.26
ICD/ZF	Low	On	Ideal	0.12	0.13	0.13
ICD/ZF	Low	On	Nonideal	0.09	0.10	0.10
ICD/ZF	Med	Off	Ideal	-2.73	-2.86	-3.02
ICD/ZF	Med	Off	Nonideal	-2.71	-2.86	-3.02
ICD/ZF	Med	On	Ideal	-2.37	-2.47	-2.59
ICD/ZF	Med	On	Nonideal	-2.38	-2.47	-2.58
ICD/ZF	High	Off	Ideal	-2.67	-2.81	-2.96
ICD/ZF	High	Off	Nonideal	-2.69	-2.82	-2.98
ICD/ZF	High	On	Ideal	-2.37	-2.47	-2.59
ICD/ZF	High	On	Nonideal	-2.36	-2.47	-2.59
MMSE	Low	Off	Ideal	-1.39	-1.49	-1.65
MMSE	Low	Off	Nonideal	-1.39	-1.52	-1.77
MMSE	Low	On	Ideal	-0.61	-0.64	-0.71
MMSE	Low	On	Nonideal	-0.53	-0.56	-0.66
MMSE	Med	Off	Ideal	-3.82	-4.14	-4.46
MMSE	Med	Off	Nonideal	-3.90	-4.14	-4.51
MMSE	Med	On	Ideal	-3.13	-3.26	-3.43
MMSE	Med	On	Nonideal	-3.18	-3.37	-3.58
MMSE	High	Off	Ideal	-4.00	-4.27	-4.63
MMSE	High	Off	Nonideal	-3.9	-4.14	-4.49
MMSE	High	On	Ideal	-3.2	-3.36	-3.57
MMSE	High	On	Nonideal	-3.17	-3.36	-3.55

The measurement setup employs a full LTE transmission containing tapped delay channel models, OFDM, and resource block allocation [7]. These tapped delay models were used: Urban Micro (Umi), Urban Micro (Umi) with all tap correlations $\alpha = 0$, and Urban Macro (Uma). These models are proposed for OTA testing of UE by 3rd-Generation Partnership Project (3GPP) [43].

In comparison to the measurements, the simulations in Section 5 use a simplified setup. Nevertheless, a comparison is valid, as the DM is validated by simulation for a single OFDM subcarrier that has a bandwidth of 15 kHz, in the LTE case. This narrow bandwidth allows a treatment of the channel as frequency flat-fading ones. The DM is validated for the smallest element, the single OFDM channel. Therefore it is also valid for the complete fading channel, which consists of many small OFDM carriers.

Figure 19 points out that the deviations d between the measured “overall” and DM results are distributed around mean values from -0.16 dB to 0.34 dB for all employed channel models, which is very low regarding all other uncertainty sources [41, 42]. The approximately Gaussian shaped distribution of the deviation d is resulting from the mentioned measurement uncertainties.

6.2. Comparison of Measurements to the Simulations. The measurements in Section 6.1 were conducted with a slightly different set of parameters as proposed by 3GPP [33, 35]. The authors present another set of simulations, as close as possible to the measurements. The channel models employ tapped delay models, and they were used in the measurements. The taps have different correlation values α , while β is always zero. To be able to use the different correlations of the taps for the simplified model, the authors employ a linear power related averaging of α . This averaging results in these values of α :

- (i) Channel model Uma: $\alpha = 0.1172$ (light correlation).
- (ii) Channel model Umi with ($\alpha = 0$): the mean value also is $\alpha = 0$ (all taps are zero; uncorrelated).
- (iii) Channel model Umi: $\alpha = 0.9474$ (strong correlation).

Results are summarized in Table 3. The mean deviation \bar{d} is given for the measurements and the closest possible simulations for several channel models. The mean deviation \bar{d} is very close to zero. *So to say, all validations with theoretical results, simulation results, and measurement results (Table 2) point in the same direction: the validity of the DM. The mean value of the deviation \bar{d} is within the given limits for all employed channel models.*

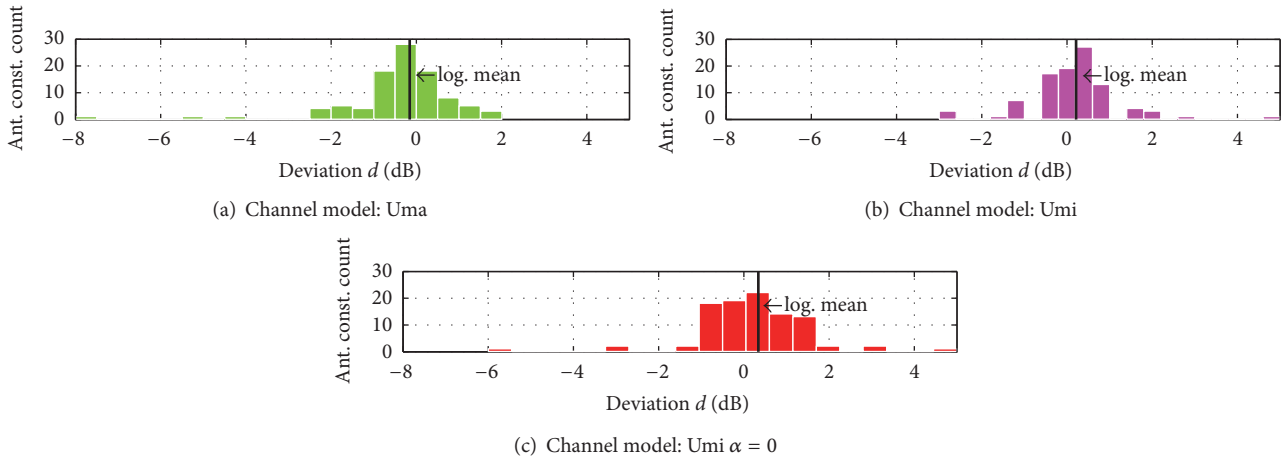


FIGURE 19: Distribution of the log. deviations d between the DM and “overall” measurement results for different channel models (Uma; Umi; Umi_alpha = 0) and different base-station correlation coefficient for the smartphone *Sony Xperia* as UE with “Good” reference antenna.

TABLE 3: Comparison of the deviation \bar{d} between measurement and simulations.

Channel model	Deviation \bar{d} in dB for		
	Measurement, Sony Xperia	Simulation ICD/ZF	Simulation MMSE
Uma	-0.16	0.1	-0.57
Umi	0.21	0.05	-0.43
Umi $\alpha = 0$	0.34	-0.42	-0.52

7. Conclusion

This paper covers performance testing of Multiple-Input Multiple-Output (MIMO) enabled wireless user equipment. It deals with over-the-air (OTA) performance tests for complete MIMO enabled user equipment (UE), including antennas and front-end and algorithmic performance. The authors investigate a very promising method, the Decomposition Method (DM). It does not compare the DM to other test procedures.

The best way to test UE would be to check the algorithmic and the antenna performance at the same time. Unfortunately, this is very slow. To speed up the measurement procedure, the Decomposition Method splits the performance tests into two parts: a static test for the antenna performance and a fading test for the algorithmic performance. The results from the separated measurements are combined and deliver accurate and repeatable results. By applying this split, the measurements can be speeded up by a factor of 36 in comparison to the combined measurements.

This paper introduces the Decomposition Method and deals with the validation of the split of the measurements. The authors validate the Decomposition Method by theoretical investigations and by numerical simulation as well as by measurement.

As many MIMO enabled devices also use Orthogonal Frequency Division Multiplexing (OFDM), the single orthogonal frequency bands have small bandwidths. The paper exploits this fact by simplifying the employed models

from generic tapped delay channel models to frequency flat response channels, without losing validity.

The authors validate the method by theoretical means using the MIMO channel capacity. They also validate it by numerical means, simulating a complete transmission system with Kronecker channel models with frequency flat fading. They show that the applicability of the Decomposition Method is given for most use cases. Low correlated channels deliver an absolute deviation of the Decomposition Method result lower than 0.7 dB.

To round up the picture, the validity of the method is shown by measurement results for the *Sony Xperia* smartphone. The mean deviation \bar{d} is within the interval $\{-0.16$ dB to 0.34 dB $\}$.

The authors provide a thorough scientific investigation of the Decomposition Method, demonstrating that this powerful and quick method to rate the performance of a MIMO enabled wireless UE is valid in most use cases. The method is able to speed up tests and still delivers accurate and reliable results with reasonable equipment effort.

Conflicts of Interest

The authors declare that they have no conflicts of interest.

References

- [1] Third Generation Partnership Project (3GPP), *Universal Terrestrial Radio Access (UTRA) and Evolved Universal Terrestrial Radio Access; Verification of Radiated Multi-Antenna Reception*

- Performance of User Equipment (UE)*, 2014.
- [2] M. D. Foegelle, "Creating a complex multipath environment simulation in an anechoic chamber," *Microwave Journal*, vol. 53, no. 8, pp. 56–64, 2010.
 - [3] M. Rumney, *LTE and the Evolution to 4G Wireless-Design and Measurement Challenges*, John Wiley & Sons, New York, NY, USA, 2013.
 - [4] I. Cartón Llorente, W. Fan, and G. F. Pedersen, "Mimo ota testing in small multiprobe anechoic chamber setups," *IEEE Antennas and Wireless Propagation Letters*, vol. 15, pp. 1167–1170, 2016.
 - [5] W. Fan, X. Carreño, P. Kyösti, J. Ø. Nielsen, and G. F. Pedersen, "Over-the-air testing of MIMO-capable terminals: evaluation of multiple-antenna systems in realistic multipath propagation environments using an OTA method," *IEEE Vehicular Technology Magazine*, vol. 10, no. 2, pp. 38–46, 2015.
 - [6] M. D. Foegelle, "The future of MIMO over-the-air testing," *IEEE Communications Magazine*, vol. 52, no. 9, pp. 134–142, 2014.
 - [7] P.-S. Kildal, C. Orlenius, and J. Carlsson, "OTA testing in multipath of antennas and wireless devices with MIMO and OFDM," *Proceedings of the IEEE*, vol. 100, no. 7, pp. 2145–2157, 2012.
 - [8] W. Fan, P. Kyösti, L. Hentilä, J. Ø. Nielsen, and G. F. Pedersen, "Rician channel modeling for multiprobe anechoic chamber setups," *IEEE Antennas and Wireless Propagation Letters*, vol. 13, pp. 1761–1764, 2014.
 - [9] W. Fan, F. Sun, J. Ø. Nielsen et al., "Probe selection in multiprobe OTA setups," *IEEE Transactions on Antennas and Propagation*, vol. 62, no. 4, pp. 2109–2120, 2014.
 - [10] Q. Xu, Y. Huang, X. Zhu, S. S. Alja'afreh, and L. Xing, "A new antenna diversity gain measurement method using a reverberation chamber," *IEEE Antennas and Wireless Propagation Letters*, vol. 14, pp. 935–938, 2015.
 - [11] W. Yu, Y. Qi, K. Liu, Y. Xu, and J. Fan, "Radiated two-stage method for LTE MIMO user equipment performance evaluation," *IEEE Transactions on Electromagnetic Compatibility*, vol. 56, no. 6, pp. 1691–1696, 2014.
 - [12] W. Fan, X. Carren, J. O. Nielsen, K. Olesen, M. B. Knudsen, and G. F. Pedersen, "Measurement verification of plane wave synthesis technique based on multiprobe MIMO-OTA setup," in *Proceedings of the IEEE Vehicular Technology Conference (VTC Fall '12)*, pp. 1–5, September 2012.
 - [13] A. Khatun, V.-M. Kolmonen, T. Laitinen, and K. Nikoskinen, "Clarification of uncertainties in MIMO over-the-air multiprobe test systems," in *Proceedings of the 7th European Conference on Antennas and Propagation (EuCAP '13)*, pp. 1427–1431, April 2013.
 - [14] W. Fan, J. O. Nielsen, X. Carreno, J. S. Ashta, G. F. Pedersen, and M. B. Knudsen, "Impact of system non-idealities on spatial correlation emulation in a multi-probe based MIMO OTA setup," in *Proceedings of the 7th European Conference on Antennas and Propagation (EuCAP '13)*, pp. 1663–1667, April 2013.
 - [15] A. Scannavini, L. J. Foged, M. Anouar, N. Gross, and J. Estrada, "OTA throughput measurements by using spatial fading emulation technique," in *Proceedings of 4th European Conference on Antennas and Propagation (EuCAP '10)*, pp. 1–5, April 2010.
 - [16] S.-S. Oh, J.-M. Kim, J.-H. Yun, and S.-Y. Kang, "Antenna measurement method in fresnel region by φ -variation scanning," *IEEE Antennas and Wireless Propagation Letters*, vol. 7, pp. 206–209, 2008.
 - [17] A. Adardour, G. Andrieu, and A. Reineix, "Influence of a stirrer on the cavity modes within a reverberation chamber," in *Proceedings of the International Symposium on Electromagnetic Compatibility (EMC EUROPE '12)*, pp. 1–4, September 2012.
 - [18] J. F. Dawson and L. Arnaut, "Reverberation (modestirred) chambers for electromagnetic compatibility," June 2007, http://www.compliance-club.com/archive/old_archive/030530.htm.
 - [19] P. Plaza-González, J. Monzó-Cabrera, J. M. Catalá-Civera, and D. Sánchez-Hernández, "New approach for the prediction of the electric field distribution in multimode microwave-heating applicators with mode stirrers," *IEEE Transactions on Magnetics*, vol. 40, no. 3, pp. 1672–1678, 2004.
 - [20] B. Zhang, Z. Yuan, and J. He, "Comparison on the test results between reverberation chamber and anechoic chamber," in *Proceedings of the Asia-Pacific Symposium on Electromagnetic Compatibility (APEMC '12)*, pp. 769–772, IEEE, Singapore, May 2012.
 - [21] C. Bruns and R. Vahldieck, "A closer look at reverberation chambers—3-D simulation and experimental verification," *IEEE Transactions on Electromagnetic Compatibility*, vol. 47, no. 3, pp. 612–626, 2005.
 - [22] A. B. Ubin and M. Z. B. M. Jenu, "Field uniformity evaluation of different stirrer structure in a reverberation chamber," in *Proceedings of the 5th IEEE Asia-Pacific Conference on Applied Electromagnetics (APACE '12)*, pp. 32–35, December 2012.
 - [23] B. Auinger, *On the performance testing of MIMO-enabled wireless mobile user devices [Ph.D. thesis]*, Graz University of Technology, Graz, Austria, 2015.
 - [24] C. von Gagern, "Decomposition test results from the second CTIA round robin test," COST IC1004, (TD(13)07049), 2013.
 - [25] B. Auinger, M. Gadringer, A. Tankielun, C. V. Gagern, and W. Boesch, "Numerical analysis of the decomposition method using LTE reference antennas," in *Proceedings of the International Conference on Computer and Network Engineering (ICCNE '14)*, December 2014.
 - [26] A. Tankielun, "Two-Channel Method for OTA performance measurements of MIMO-enabled devices," White Paper, Rohde & Schwarz, Munich, Germany, 2011.
 - [27] H. Zarrinkoub, *Understanding LTE with MATLAB- From Mathematical Modelling to Simulation and Prototyping*, Wiley, West Sussex, UK, 1st edition, 2014.
 - [28] I. Szini, "Reference antennas proposal for MIMO OTA," European Cooperation in Science and Technology (COST) IC1004, Document Nr. 1(TD(11)02009), October 2011.
 - [29] C. Gagern and A. Tankielun, "Test results from the second CTIA round robin test," The Wireless Association (CTIA), February 2013.
 - [30] A. Tankielun and C. Von Gagern, "On spatial characteristics of the decomposition method in MIMO OTA testing," in *Proceedings of the 8th European Conference on Antennas and Propagation (EuCAP '14)*, pp. 3674–3678, Hague, The Netherlands, April 2014.
 - [31] A. Paulraj, R. Nabar, and D. Gore, *Introduction to Space-Time Wireless Communications*, Cambridge University Press, Cambridge, UK, 2003.
 - [32] D. Kececioglu, *Reliability Engineering Handbook Volume 1*, DEStech Publications, Lancaster, Pa, USA, 2002.
 - [33] 3GPP, "Technical specification group radio access network; evolved universal terrestrial radio access (EUTRA); user equipment (UE) radio transmission and reception," (Release 12), September 2014.

- [34] C. Oestges, "Validity of the Kronecker model for MIMO correlated channels," in *Proceedings of the IEEE 63rd Vehicular Technology Conference (VTC '06)*, vol. 6, pp. 2818–2822, Melbourne, Australia, July 2006.
- [35] ETSI AND 3GPP, *Technical Specification: LTE; Evolved Universal Terrestrial Radio Access (E-UTRA); Base Station (BS) Conformance Testing (3GPP TS 36.141 Version 12.5.0 Release 12)*, 2014.
- [36] U. Mengali, *Synchronization Techniques for Digital Receivers*, Plenum Press, New York, NY, USA, 1997.
- [37] J. G. Proakis, *Digital Communications*, McGraw-Hill, New York, NY, USA, 5th edition, 2008.
- [38] N. J. Salkind, *Encyclopedia of Research Design*, Sage, Thousand Oaks, Calif, USA, 1st edition, 2010.
- [39] E. Telatar, "On limits of wireless communications in a fading environment when using multiple antennas," *European Transactions on Telecommunications*, vol. 10, no. 6, pp. 585–595, 1999.
- [40] W. Fan, I. Szini, M. D. Foegelle, J. O. Nielsen, and G. F. Pedersen, "Measurement uncertainty investigation in the multi-probe OTA setups," in *Proceedings of the 8th European Conference on Antennas and Propagation (EuCAP '14)*, pp. 1068–1072, Hague, The Netherlands, April 2014.
- [41] Third Generation Partnership Project (3GPP), "Errors and uncertainties in the mimo ota measurements r4-131673," Meeting 65, New Orleans, November 2012.
- [42] 3GPP, "Measurement uncertainty evaluation of multiprobe method," in *Proceedings of the 3GPP Meeting 66*, Chicago, Ill, USA, November 2012.
- [43] CTIA, "Draft CTIA MIMO OTA test plan version 0.2 (CTIA MOSG131214; sub working group document available to CTIA sub-working group members)," December 2013.

Research Article

Attenuation by a Human Body and Trees as well as Material Penetration Loss in 26 and 39 GHz Millimeter Wave Bands

Qi Wang,¹ Xiongwen Zhao,^{1,2,3} Shu Li,¹ Mengjun Wang,² Shaohui Sun,² and Wei Hong³

¹School of Electrical and Electronic Engineering, North China Electric Power University, Beijing 102206, China

²State Key Laboratory of Wireless Mobile Communications, China Academy of Telecommunications Technology (CATT), Beijing 100191, China

³State Key Laboratory of Millimeter Wave, Southeast University, Nanjing 210096, China

Correspondence should be addressed to Xiongwen Zhao; zhaowx@ncepu.edu.cn

Received 13 October 2016; Revised 13 March 2017; Accepted 20 March 2017; Published 28 March 2017

Academic Editor: Stefan R. Panic

Copyright © 2017 Qi Wang et al. This is an open access article distributed under the Creative Commons Attribution License, which permits unrestricted use, distribution, and reproduction in any medium, provided the original work is properly cited.

This paper investigates the attenuation by a human body and trees as well as material penetration loss at 26 and 39 GHz by measurements and theoretical modeling work. The measurements were carried out at a large restaurant and a university campus by using a time domain channel sounder. Meanwhile, the knife-edge (KE) model and one-cylinder and two-cylinder models based on uniform theory of diffraction (UTD) are applied to model the shape of a human body and predict its attenuation in theory. The ITU (International Telecommunication Union) and its modified models are used to predict the attenuation by trees. The results show that the upper bound of the KE model is better to predict the attenuation by a human body compared with UTD one-cylinder and two-cylinder models at both 26 and 39 GHz. ITU model overestimates the attenuation by willow trees, and a modified attenuation model by trees is proposed based on our measurements at 26 GHz. Penetration loss for materials such as wood and glass with different types and thicknesses is measured as well. The measurement and modeling results in this paper are significant and necessary for simulation and planning of fifth-generation (5G) mm-wave radio systems in ITU recommended frequency bands at 26 and 39 GHz.

1. Introduction

Attenuation by a human body and trees and penetration loss of material at the ITU proposed frequency bands [1], 24.25–27.5 and 37–40.5 GHz, are important issues for future 5G (fifth-generation) wireless access systems. In this paper, attenuation by a human body and trees and penetration loss of different materials with 1 GHz bandwidth were measured with time domain channel sounder at 26 and 39 GHz, respectively. As far as we know, there are no measurements and modeling work reported in open literature on human blockage, attenuation by trees, and penetration loss of different materials at 24.25–27.5 and 37–40.5 GHz frequency bands. The prediction of attenuation by a human body and trees and the penetration loss in this work are important and necessary for future mm-wave wireless communication systems.

By considering a human body as an infinite absorbing screen, KE model was used to predict the attenuation by a person in a frequency range from 4 to 10 GHz in [2]. In

addition, measurements in [3] showed that double knife-edge approach was suitable for both 60 GHz and 300 GHz bands. In addition to regarding a human body as an absorbing screen, a cylindrical model by uniform theory of diffraction (UTD) was also applied to predict human body attenuation. Measurements in [4, 5] were performed at 10 GHz which showed a strong correlation between a human body and a perfect conducting cylinder. By comparison with measurements at 60 GHz [6], it is shown that the UTD model was clearly overestimating the human attenuation.

In [7], measurements by a single tree were taken at a frequency range between 7.25 and 8.0 GHz and the attenuation by a tree is between 15 dB and 23 dB. In [8], measurements were taken at 9.6 GHz, 28.8 GHz, 57.6 GHz, and 96.1 GHz, and the results show that the vegetation loss increases nearly linearly at a range rate from 1.3 to 2.0 dB per meter. The ITU-R P-833-8 [9] proposes a model for the range from 30 MHz to 60 GHz: an exponential slant path model with elevation angle correction. Other widely used penetration loss models

are the exponential models proposed in [10–12], which do not consider the factor of elevation and are said to present frequency application ranges up to 57.6, 95, and 40 GHz, respectively. However, the coefficients of these models have been mainly computed from limited sets of data measured at frequencies close to 2 GHz. Therefore, there is still a need for verification measurements to test their correctness and applicability for higher frequencies.

Previous literatures about penetration loss of material in millimeter wave bands focused on 28 GHz and 60 GHz. In [13], signals through a hollow plasterboard wall resulted in a penetration loss ranging between 5.4 dB and 8.1 dB. In [14], the measured penetration losses are 2 dB, 9 dB, and 35.5 dB at 60 GHz through a glass door, a plasterboard wall with metallic studs, and a wall with a metal-backed blackboard, respectively.

In this paper, the measurements of the attenuation by a human body and trees as well as penetration loss for material were carried out. Attenuation by a human body was measured with a person laterally crossing the transceiver connection line. The KE and UTD methods are used to predict human body's attenuation. When using UTD, the human body was regarded as a cylinder and a combined model, respectively. In the combined model, the shoulders are regarded as two cylinders. By comparisons with different human models, the target is to get a better model to predict human body's attenuation at 26 and 39 GHz. In addition, we have measured the attenuation by willow trees at 26 GHz, and then the ITU-R P-833-8 model is modified by comparison with the measurement results. Measurements of the penetration loss for different materials were carried out in this work as well, for example, transparent glass with different thickness, frosted glass, and wood with plastic cladding.

The remainder of this paper is organized as follows. In Section 2, the measurement campaigns are introduced. In Section 3, attenuation models by a human body including KE and UTD one-cylinder and UTD two-cylinder models as well as the attenuation model by trees in ITU-R P-833-8 are investigated. Section 4 presents the measurement results with the comparisons of the models. Finally, we conclude the work in this paper in Section 5.

2. Measurement Campaigns

2.1. Attenuation by a Human Body and Trees. Channel measurements of the attenuation by a human body and trees were conducted at Keysight, Beijing office, and in the campus of North China Electric Power University, respectively. Table 1 lists the detailed specification of the system.

Figure 1 shows the measurement environment at a restaurant with more than 150 m² for human body attenuation. The heights of the transmitter (Tx) and receiver (Rx) are both 1.3 m above the ground level with distance of 15 meters.

The attenuation was measured with a person laterally crossing the Tx-Rx connection line as shown in Figure 2. When doing the measurement, the person was moving from -0.5 to 0.5 m crossing the Tx-Rx connection line with 2.5 cm distance step. Because of the sounding system limitation, the continuous measurement with time is not possible; the

TABLE 1: Specification of the system.

Parameter	26 GHz	39 GHz
Bandwidth	1 GHz	1 GHz
Maximum delay	1.024 us	1.024 us
Delay resolution	1 ns	1 ns
Tx power	24 dBm	24 dBm
Heights of the Tx/Rx	1.3/1.3 m (human)	1.3/1.3 m (human)
	6.0/2.0 m (tree)	6.0/2.0 m (tree)
Gain of the horn antenna	24.3 dBi	27 dBi
Polarization of the horn antenna	Vertical	Vertical
HPBW of the horn antenna	10°	10°



FIGURE 1: Measurement environment for human attenuation.

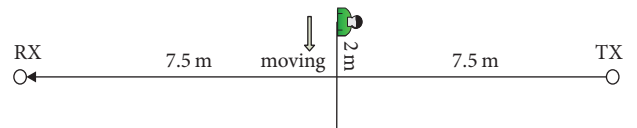


FIGURE 2: A person laterally crossing the Tx-Rx connection line.

measurement had to be done with the human blocker moving step by step in different positions. The received power was measured when the Tx and Rx were placed in free space and the person was at fixed positions. In each position, the measurement was done 10 times (human blocker adjusting their positions 10 times as well); then the mean received power was calculated to prevent position randomness, rare moving scatterers occurring during the measurements, and the instability of the measurement system. The shoulder width of the measured person is 0.49 m, and thickness of the body is 0.24 m. The human body attenuation was measured at both 26 and 39 GHz, respectively.

Figure 3 shows the measurement environment for trees attenuation at 26 GHz; 1–4 willow trees were measured between the Tx and Rx with the heights of 6.0 m and 2.0 m, respectively. The height of the willow trees is about 14 m. The tree radius is about 3 m with sparse branches and leaves. An omnidirectional biconical horn with 3 dBi gain was used at the Tx, and a 26 dBi horn with the height of 2 m was applied at the Rx and rotated just in the elevation plane with azimuth



FIGURE 3: Measurement environment for tree attenuation.

angle of 0° . The 0° direction in the azimuth plane points to the Tx. At locations 1 and 2, the horn was rotated in the elevation plane from 10° to 50° with a step of 10° , while at locations 3 and 4, the horn was rotated in elevation plane from 10° to 40° and from 10° to 30° with a step of 10° , respectively. When doing the measurements, the Rx was placed in the middle of the two adjacent trees.

2.2. Penetration Loss of Different Materials. Penetration loss for different materials was measured at KeySight office in Beijing. The received power was measured when the transceiver was in free space and the tested material was placed in the middle of the transceiver; then the power difference is defined as the penetration loss of the material.

Figure 4 shows the measurement scenarios for tested materials. The wood and glass with different thickness and surface were measured. In Figure 4(a), it is a wooden door with painting. In Figure 4(d), it is a wooden door with plastic cladding. Two kinds of glass are measured: one is transparent glass shown in Figure 4(b) and the other is frosted glass shown in Figure 4(c). In addition, there are two transparent glass doors in the hall; the penetration losses through one door and two doors were measured, respectively.

Transmit power was set from 0, 10, and 20 dBm in each measurement; the channel impulse responses were recorded 10 times with same transmit power. Finally, the mean penetration loss with different transmit power is calculated to avoid possible instability of the measurement system.

3. Models of Attenuation by a Human Body and Trees

3.1. Attenuation Models by a Human Body

3.1.1. Double Knife-Edge Model. In this model, a human body is regarded as an absorbing screen with infinite height, where shoulders are regarded as two knife edges. Figure 5 shows the geometry of the two knife edges, where h_a and h_b are the widths for the left and right human shoulders. d_T and d_R are the distances from the Tx and Rx to the human, respectively. The diffraction field A_S is the sum of two knife edges, which is given by

$$A_S [h_a, h_b] = A_H [h_a] + A_H [h_b]. \quad (1)$$

The diffraction field A_H can be calculated as

$$A_H = \frac{U_H}{U_0} = \frac{1+j}{2} \left\{ \left(\frac{1}{2} - C(\nu) \right) - j \left(\frac{1}{2} - S(\nu) \right) \right\}, \quad (2)$$

where U_H and U_0 denote the diffracted field and the field in absence of an obstruction, respectively.

$C(\nu) + jS(\nu) = \int_0^\nu \exp(j\pi t^2/2) dt$ is the Fresnel integral, and

$$\nu(h) = h \sqrt{\frac{2}{\lambda} \frac{d_T + d_R}{d_T d_R}} \quad (3)$$

is relative to wavelength λ , obstruction depth h , and distance parameters.

3.1.2. One-Cylinder Model. In addition to the knife-edge models aforementioned, UTD model has been applied to predict the attenuation by human body as well, in which a human body is regarded as a cylinder. Figure 6 shows a cylinder model with radius of α . Point S is the source position. Points P and \tilde{P} are the observation positions, respectively, in the shadow and illuminated regions. Q_R in Figure 6 is the reflection point, while $S_{d1} \sim S_{d4}$ are the diffraction points.

As shown in Figure 6, when the observation point \tilde{P} is in the illuminated region, the total received field is the sum of the reflected field from the human body and the incident field in case the person does not block the Tx-Rx connection line with lateral crossing. When the person blocks the Tx-Rx connection line, the receiver appears to be in the shadow region and the diffracted fields from both sides of the human body contribute to the total received field.

The incident field of observation point \tilde{P} can be expressed as

$$E^i(r) = E^i(r_0) \sqrt{\left(\frac{\rho_1^i}{\rho_1^i + s^i} \right) \left(\frac{\rho_2^i}{\rho_2^i + s^i} \right)} e^{-jks^i}, \quad (4)$$

where ρ_1^i and ρ_2^i are the radii of curvatures of the incident wavefront. r_0 is the reference point, and s^i is the distance along the incident ray from r_0 to reference point r . k is wave number. Equation (4) can be simplified further to (5)–(7) if the incident wave is assumed as plane wave, spherical wave, and cylindrical wave, respectively:

$$E^i(r) = E^i(r_0) e^{-jks^i}, \quad (5)$$

$$E^i(r) = \frac{E^i(r_0) e^{-jks^i}}{s^i}, \quad (6)$$

$$E^i(r) = \frac{E^i(r_0) e^{-jks^i}}{\sqrt{s^i}}. \quad (7)$$



FIGURE 4: Penetration loss measurements for a wooden door of the laboratory (a), a transparent glass door of the hall (b), a frosted glass door of a small office (c), and a wooden door of the cabinet (d).

The reflected field is calculated by

$$E^r(P) = E^i(Q_R) \bar{\bar{R}} \sqrt{\left(\frac{\rho_1^r}{\rho_1^r + s^r}\right) \left(\frac{\rho_2^r}{\rho_2^r + s^r}\right)} e^{-jks^r}, \quad (8)$$

where ρ_1^r and ρ_2^r are the radii of curvatures of the reflected wave and $\bar{\bar{R}}$ includes hard reflection coefficients R_h and soft reflection coefficients R_s .

The reflection coefficient is defined as

$$R_{s,h} = - \left[\sqrt{\frac{-4}{\xi^L}} e^{-j(\xi^L)^3/12} \left\{ \frac{e^{-j(\pi/4)}}{2\sqrt{\pi}\xi^L} [1 - F(X^L)] + \hat{P}_{s,h}(\xi^L) \right\} \right], \quad (9)$$

where ξ^L and X^L are expressed in [15].

The diffracted field is

$$E^d(P) = E^i(S_{d1}) \bar{\bar{T}} \sqrt{\frac{\rho_2^d}{s^d(\rho_2^d + s^d)}} e^{-jks^d}, \quad (10)$$

when P is located in shadow region.

$$\begin{aligned} \rho_2^d &= s_0 + t, \\ \bar{\bar{T}}_{s,h} &= - \left[\sqrt{m(S_{d1})m(S_{d2})} \sqrt{\frac{2}{k}} \left\{ \frac{e^{-j(\pi/4)}}{2\sqrt{\pi}\xi^d} [1 - F(X^d)] + \hat{P}_{s,h}(\xi^d) \right\} \right] \sqrt{\frac{s_0}{s_0 + t}} e^{-jkt}, \end{aligned} \quad (11)$$

where t is the distance between two diffraction points. s_0 is the distance between the source and the first diffraction point S_{d1} , and s^d is the distance between the second point S_{d2} and P . The ‘‘Transition’’ function $F(X)$, ‘‘Pekeris’’ function, and other parameters can be found in [15–17].

TABLE 2: Summary of the maximum attenuation of the measurement and the upper bound of the KE, one-cylinder, and two-cylinder models.

Frequency	Measurement	The maximum attenuation (dB)		
		KE model (upper bound)	One-cylinder model (upper bound)	Two-cylinder model (upper bound)
26 GHz	12.66	11.51	14.25	17.89
39 GHz	19.03	13.46	15.66	19.99

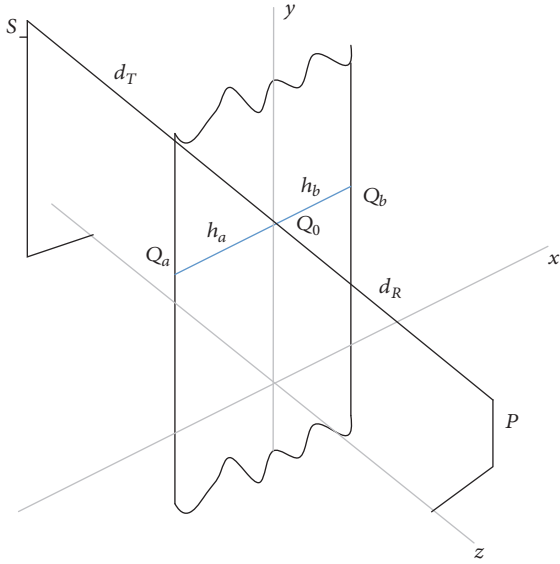


FIGURE 5: Double knife-edge model.

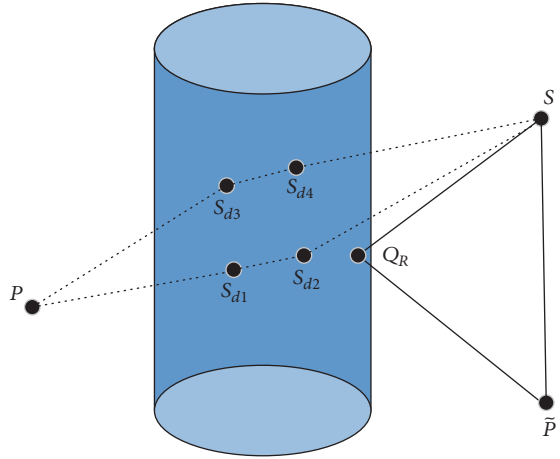


FIGURE 6: One-cylinder model.

3.1.3. *Two-Cylinder Model.* Two-cylinder model is based on one-cylinder model; instead of regarding a person as a whole cylinder, the shoulders are regarded as two cylinders with smaller radii as shown in Figure 7.

3.2. *Attenuation Models by Trees.* According to ITU-R P-833-8 [9], attenuation by trees can be expressed as

$$L = A \cdot f^B d_v^C \theta^D \text{ dB}, \quad (12)$$

where f is the carrier frequency in MHz, d_v is the penetration distance of the trees between transmitter and receiver, θ is

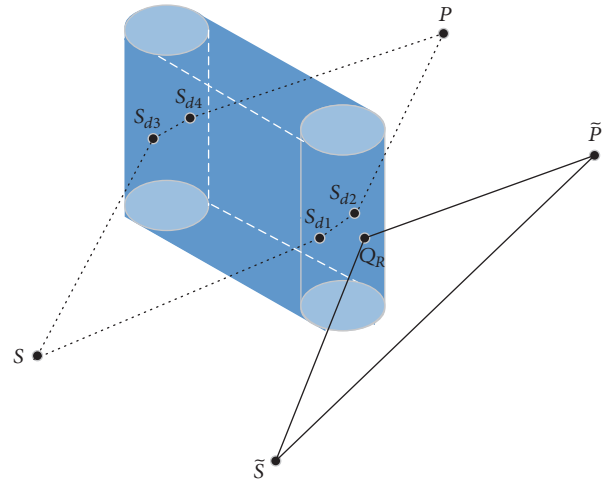


FIGURE 7: Two-cylinder model.

the elevation in degrees, and A , B , C , and D are empirical constants.

4. Measurement Results and Analysis

4.1. *Attenuation by a Human Body and Trees.* In the measurements, no moving scatterers existed close to the transceiver. The heights of the transceiver as well as the distance between transmitter and receiver were planned in detail to avoid reflection from the ground, especially in human blockage measurement with smooth ground. Because of very narrow beamwidth of the horn antennas, multipath from fixed scatterers can also be avoided. Therefore, the attenuation is essentially the diffraction loss around the blocker(s). When doing the measurements, at first, the CIRs were measured in free space; then the CIRs were recorded with the blocker(s). The noise floor was decided by averaging the last 200 delay samples, and we use 5 dB higher than the noise floor to remove the noise due to its fluctuation. The human attenuation was defined as the difference of the wideband received powers which was measured in free space and measured with human blocker.

Figures 8(a) and 8(b) are the comparisons between the measurements and theoretical models at 26 and 39 GHz, respectively. Table 2 summarizes the maximum attenuation of the measurements and the maximum attenuation of the upper bound of KE and one-cylinder and two-cylinder models at 26 and 39 GHz, respectively. In Figure 8(a), compared to the upper bound of one-cylinder and two-cylinder models, the measurement result agrees better with the upper bound of the KE model. The field fluctuation in shadowing

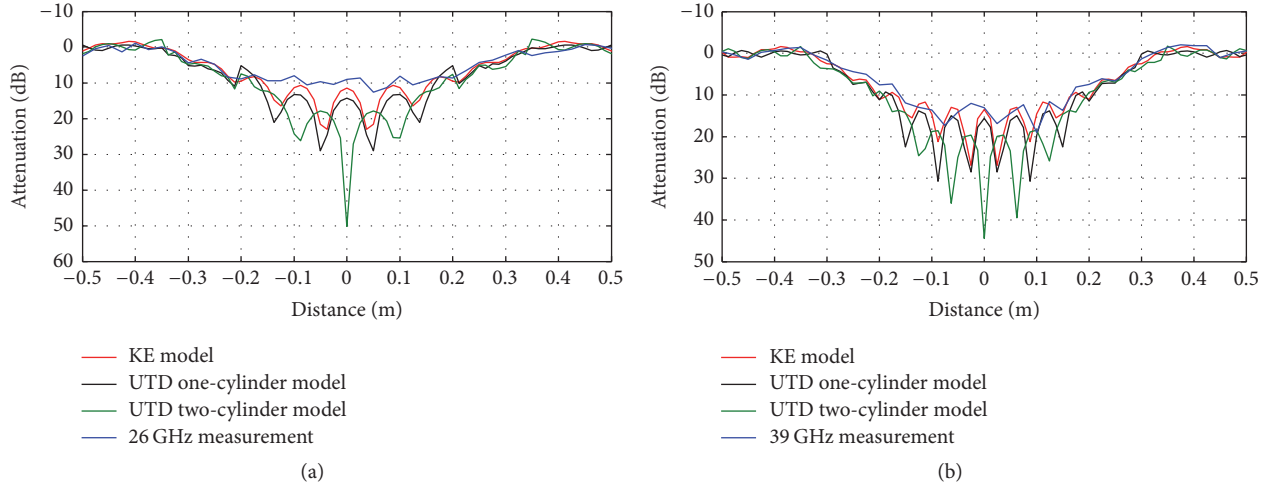


FIGURE 8: Comparison between the measurement and models: (a) 26 GHz and (b) 39 GHz.

region is obviously observed in the KE and one-cylinder and two-cylinder models due to the superposition of the field from both sides of the models in a coherent manner. The fluctuation intensity is very sensitive to the wavelength and measurement configurations. The maximum attenuation of measurement is 12.66 dB. If we just consider the upper bound values of models, the maximum attenuation of the KE and one-cylinder and two-cylinder models is 11.51, 14.18, and 18.32 dB, respectively, as shown in Table 2. The RMSEs are 1.97 dB, 2.50 dB, and 2.97 dB between measurements and the three models at 26 GHz, respectively. In Figure 8(b), the maximum attenuation of the measurement is 19.03 dB and it is close to the upper bound of two-cylinder model as shown in Table 2. The RMSEs are 2.01 dB, 2.40 dB, and 2.89 dB between measurements and KE and one-cylinder and two-cylinder models at 39 GHz, respectively. As a whole, the measurements agree better with the KE model at 26 and 39 GHz in the shadow region. Two-cylinder model might be more like the human body, but it overestimates the attenuation by numerical calculation. In addition, the KE model is concise; therefore it is good to be used to predict the human blockage effect at 26 and 39 GHz in a practical use case.

If the shape of a human body is neglected, we can use measured attenuation only to get more simple models with respect to distances at 26 and 39 GHz. Figure 9 shows the attenuation models based on measurements. Formulas 4.1 are the empirical piecewise functions for human attenuation at 26 and 39 GHz. When the human does not block the Tx and Rx connection line, the attenuation fluctuates around zero dB.

$$\begin{aligned}
 & -0.5 \times d + 0.1 \quad d < -\frac{W}{2}, \\
 & -128 \times d^2 - 0.1 \times d + 10.6 \quad -\frac{W}{2} \leq d \leq \frac{W}{2}, \\
 & -4.7 \times d + 2.4 \quad d > \frac{W}{2}, \\
 & -11.5 \times d - 4.2 \quad d < -\frac{W}{2},
 \end{aligned}$$

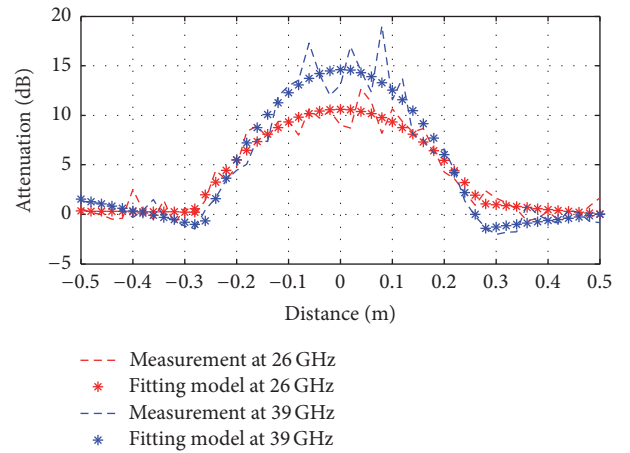


FIGURE 9: Simplified human attenuation models by measurements at 26 GHz and 39 GHz.

$$\begin{aligned}
 & -221 \times d^2 + 1.3 \times d + 14.6 \quad -\frac{W}{2} \leq d \leq \frac{W}{2}, \\
 & 6.4 \times d - 3.2 \quad d > \frac{W}{2},
 \end{aligned} \tag{13}$$

where W is the width of the human and d is the distance.

When measuring the attenuation by trees, the horn antenna was adjusted to point the trees with azimuth angle of 0° ; then the horn was rotated in the elevation plane to measure the attenuation from different parts of the trees. In the following text, measurement locations 1–4 are with respect to 1–4 trees, respectively. At locations 1 and 2, the horn was rotated in the elevation plane from 10° to 50° with a step of 10° , while at locations 3 and 4, the horn was rotated in elevation plane from 10° to 40° and from 10° to 30° with a step of 10° , respectively. Based on the transceiver distance and height difference of the transmitter and receiver, the elevation angles of the direct rays are 31.62° , 18.58° , 12.88° , and 10.26° , respectively, for locations 1 to 4.

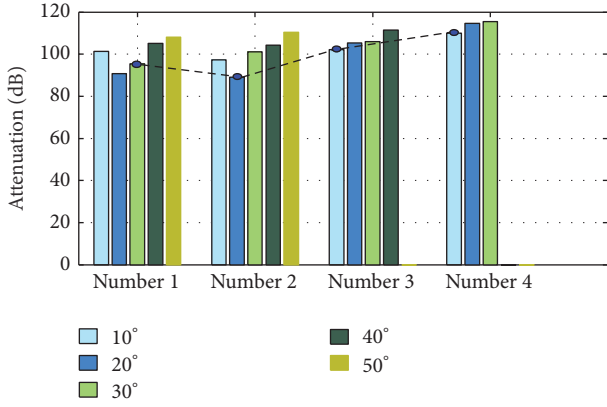


FIGURE 10: Measured attenuation by 1–4 trees with different elevation angles.

TABLE 3: Attenuation by 1–4 willow trees.

Location	1	2	3	4
Attenuation (dB)	18.50	12.80	15.54	22.42

Figure 10 shows the attenuation by 1–4 trees, respectively, including free space path loss in different elevation angles. Numbers 1–4 mean locations 1–4. The dashed line shows attenuation of the direct rays by the tree(s). The elevation angles for the direct rays by 1–4 trees are different because of different distances between transmitter and receiver.

We define here the attenuation by tree(s) as the difference between the attenuation of the direct path of the tree(s) and the path loss in free space. Therefore, the attenuation by 1–4 willow trees is shown in Table 3.

At location 1, the attenuation of the 1st tree is 18.50 dB, a large attenuation caused by the trunk and leaves. At location 2, the attenuation is 12.80 dB caused by the branches and leaves of the 1st and 2nd trees with 1.22 dB/m attenuation in average according to the penetration distance of the trees. Sparse branches and leaves make the attenuation small.

At location 3, the attenuation is 15.54 dB. The direct path is blocked by the branches and leaves of the 1st to 3rd trees with 0.97 dB/m attenuation in average. At location 4, the attenuation is 22.42 dB in total. The direct path is blocked by the branches and leaves of the 1st to 4th trees with 1.10 dB/m attenuation in average.

Based on our measurements, in case the direct path was blocked by the branches and leaves, the average attenuation is within 0.97 to 1.22 dB per meter, which is affected by the density of the branches and leaves. In case the direct path was blocked by the trunk, the attenuation by a willow tree is up to 18.50 dB. Therefore, difference between the attenuation by the trunk and that by branches and leaves is observed. In this work, the latter case is taken into consideration.

In Rec. ITU-R P-833-8 [9], attenuation in vegetation was investigated by measurements done in pine woodland in Austria for satellite slant paths as expressed in Section 3.2 for the model with A – D empirical parameters. The model for pin trees is expressed as follows:

$$L = 0.25 \cdot f^{0.39} \cdot d_v^{0.25} \cdot \theta^{0.05} \text{ dB}, \quad (14)$$

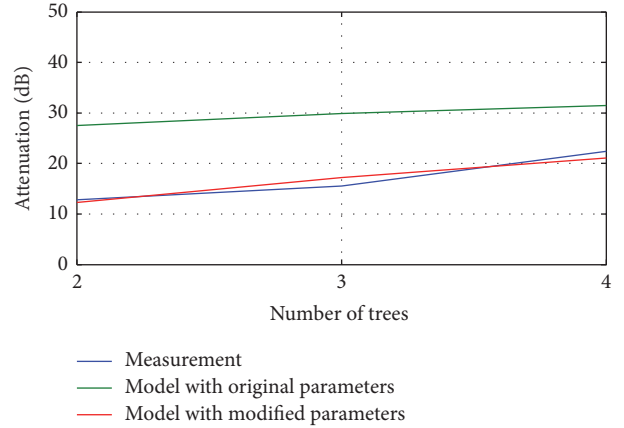


FIGURE 11: Comparison between the models and measurement.

where $A = 0.25$, $B = 0.39$, $C = 0.25$, and $D = 0.05$ are empirical parameters for (12). Figure 11 shows our measurement attenuation by the branches and leaves of willow trees in blue line; the attenuation of (14) for pin trees is in green line. It is seen that ITU model overestimates the attenuation of willow trees. ITU model may include the trunk attenuation inside with small elevation angles in satellite links. To use model (14) at 26 GHz, parameters in it need to be modified. In (14), parameter D shows the relationship between the attenuation and elevation angles. When D is positive, it means that the attenuation is proportional to an elevation angle. In fact, the branches and leaves in the upper part of the trees are more sparse and thinner than those in the lower part. Thicker branches and leaves make the attenuation larger; therefore the attenuation should grow inversely proportional to the elevation angles. Considering aforementioned reasons, (12) and (14) can be modified as follows:

$$\log(L) = 0.39 \cdot \log(A \cdot f) + 0.25 \cdot \log(d_v) + D \cdot \log(\theta) \text{ dB}, \quad (15)$$

where A and D are modified by measurement data at 26 GHz using least-square method; then (15) can be expressed as

$$L = 0.58 \cdot f^{0.39} \cdot d_v^{0.25} \cdot \theta^{-0.63} \text{ dB}. \quad (16)$$

It is seen from Figure 11 that the modified model (16) in red line agrees well with the measurement result.

4.2. Penetration Loss of Different Materials. Table 4 summarizes the penetration loss of different materials with specific thicknesses at 26 and 39 GHz, respectively. It is seen that the loss at 39 GHz is larger than that at 26 GHz for each material in general. From Table 4, it is found that the total thickness of the two transparent glass doors of the hall is 25.70 mm which is thinner than the wooden door of the laboratory, but their attenuation is almost the same; it means that wooden attenuation is smaller than that of transparent glass in the same thickness at 26 and 39 GHz, respectively. The wooden door of the cabinet is thinner than the wooden door of the laboratory; however, no big attenuation difference at 26 GHz

TABLE 4: Penetration losses of the materials.

Material	Thickness	26 GHz	39 GHz
Wooden door of the laboratory	47.94 mm	5.50 dB	9.69 dB
Transparent glass door of the hall (one door)	12.85 mm	3.95 dB	4.59 dB
Transparent glass door of the hall (two doors)	25.70 mm	5.55 dB	9.45 dB
Frosted glass door of the small office	12.30 mm	4.10 dB	4.65 dB
Wooden door of the cabinet	19.82 mm	4.16 dB	5.59 dB

is found. In addition, penetration loss of the frosted glass door is slightly larger than that of transparent glass.

5. Conclusions

In this paper, attenuation by human body and trees and penetration loss of different materials at 26 and 39 GHz are investigated for 5G wireless communications. By comparisons of the KE model, one-cylinder model, and two-cylinder model with measured human attenuation, it is found that the KE model is compact and concise and is a better model to be applied. In addition, more accurate attenuation models by a human are developed based on measurement attenuation using linear regression method at 26 and 39 GHz, respectively. The attenuation by trees is also investigated in this work at 26 GHz. In case the direct path is blocked by the branches and leaves, the attenuation by willow trees is within 0.97~1.22 dB per meter. In case the direct path is blocked by the trunk, the attenuation by a tree is up to 18.50 dB. The material penetration loss measurements are focused on wooden and glass. It is found that the penetration loss for wood is smaller than that of transparent glass in the same thickness, and the penetration loss of frosted glass is slightly larger than that of transparent glass.

Conflicts of Interest

The authors declare that they have no conflicts of interest.

Acknowledgments

This work is supported by State Key Laboratory of Wireless Communications, China Academy of Telecommunications Technology (CATT), and the open research fund of State Key Laboratory of Millimeter Waves, Southeast University (no. K201517). It is also supported by the Fundamental Research Funds for the Central Universities (2015 XS19). Thanks are due to Mr. Zhu Wen, Fei Cao, and Tiansheng Zhang from KeySight, Beijing, for their great help in making the measurements.

References

- [1] ITU, in *Proceedings of the World Radio Communication Conference (WRC '15)*, ITU 500-E, Geneva, Switzerland, November 2015.
- [2] J. Kunisch and J. Pamp, "Ultra-wideband double vertical knife-edge model for obstruction of a ray by a person," in *Proceedings of the IEEE International Conference on Ultra-Wideband (ICUWB '08)*, pp. 17–20, Hannover, Germany, September 2008.
- [3] M. Jacob, S. Priebe, R. Dickhoff, T. Kleine-Ostmann, T. Schrader, and T. Kürner, "Diffraction in mm and sub-mm wave indoor propagation channels," *IEEE Transactions on Microwave Theory and Techniques*, vol. 60, no. 3, pp. 833–844, 2012.
- [4] M. Ghaddar, L. Talbi, and T. A. Denidni, "Human body modelling for prediction of effect of people on indoor propagation channel," *Electronics Letters*, vol. 40, no. 25, pp. 1592–1594, 2004.
- [5] M. Ghaddar, L. Talbi, T. A. Denidni, and A. Sebak, "A conducting cylinder for modeling human body presence in indoor propagation channel," *IEEE Transactions on Antennas and Propagation*, vol. 55, no. 11, pp. 3099–3103, 2007.
- [6] M. Peter, M. Wisotzki, M. Raceala-Motoc et al., "Analyzing human body shadowing at 60 GHz: systematic wideband MIMO measurements and modeling approaches," in *Proceedings of the 6th European Conference on Antennas and Propagation (EuCAP '12)*, pp. 468–472, Prague, Czech, March 2012.
- [7] L. E. Bråten and V. Arneson, "Measurements of single tree attenuation for vehicular satellite communications at X-band," in *Proceedings of the 8th European Conference on Antennas and Propagation (EuCAP '14)*, pp. 1264–1268, Hague, The Netherlands, April 2014.
- [8] D. L. Jones, R. H. Espeland, and E. J. Violette, *Vegetation Loss Measurements at 9.6, 28.8, 57.6, and 96.1 GHz through a Conifer Orchard in Washington State*, U.S. Department of Commerce, 1989.
- [9] ITU, "Attenuation in vegetation," Rec. ITU-R P.833-8, 2013.
- [10] COST 235, "Radiowave propagation effects on next generation fixed services terrestrial telecommunications systems," Final Report, 1996.
- [11] M. A. Weissberger, "An initial summary of models for predicting the attenuation of radio waves by trees," Tech. Rep. ESD-TR-81-101, Electromagnetic Compatibility Analysis Center, 1982.
- [12] M. O. Al-Nuaimi and R. B. L. Stephens, "Measurements and prediction model optimisation for signal attenuation in vegetation media at centimetre wave frequencies," *IEE Proceedings—Microwaves, Antennas and Propagation*, vol. 145, no. 3, pp. 201–206, 1998.
- [13] E. J. Violette, R. H. Espeland, R. O. DeBolt, and F. Schwering, "Millimeter-wave propagation at street level in an urban environment," *IEEE Transactions on Geoscience and Remote Sensing*, vol. 26, no. 3, pp. 368–380, 1988.
- [14] K. Sato, T. Manabe, T. Ihara et al., "Measurements of reflection and transmission characteristics of interior structures of office building in the 60-GHz band," *IEEE Transactions on Antennas and Propagation*, vol. 45, no. 12, pp. 1783–1792, 1997.
- [15] R. G. Kouyoumjian and P. H. Pathak, "A uniform geometrical theory of diffraction for an edge in a perfectly conducting surface," *Proceedings of the IEEE*, vol. 62, no. 11, pp. 1448–1461, 1974.
- [16] P. H. Pathak, "An asymptotic analysis of the scattering of plane waves by a smooth convex cylinder," *Radio Science*, vol. 14, no. 3, pp. 419–435, 1979.
- [17] N. A. Logan, *General Research in Diffraction Theory. Volume I LMSD-288087; and Volume II LMSD-288088*, Missiles and Space Division, Lockheed Aircraft Corporation, 1959.

Research Article

Measured Performance Comparisons between Spatial Multiplexing and Beamforming Arrays in the 28 GHz Band

Dazhi Piao, Xingning Jia, Xiaochuan Ma, Qingxin Guo, and Zengrui Li

Department of Communication Engineering, Communication University of China, Beijing 100024, China

Correspondence should be addressed to Dazhi Piao; piaodazhi@hotmail.com

Received 31 October 2016; Revised 3 January 2017; Accepted 6 February 2017; Published 23 March 2017

Academic Editor: Rausley A. A. De Souza

Copyright © 2017 Dazhi Piao et al. This is an open access article distributed under the Creative Commons Attribution License, which permits unrestricted use, distribution, and reproduction in any medium, provided the original work is properly cited.

A spatial multiplexing (SM) array and a beamforming (BF) array with similar antenna size working at 28 GHz are designed and fabricated. In the SM array, a 4×4 MIMO system is realized with each port composed of a four-element subarray. In the BF array, the whole 16 elements are used to formulate a high-gain array. The measured S -parameters are in agreement with the simulated results. For both arrays, the channel capacities are computed by the measured channel matrix and signal-to-noise ratio (SNR) in an office room. Results show that capacity of the SM system is larger than that of the BF system, although the gain of BF array is about 5 dB larger than that of the SM array. However, the capacity of the SM array depends heavily on SNR; specifically, for the 1 dBm transmit power, communication distance $R = 25$ cm, the ergodic capacity of the SM system is 2.76 times that of the BF system, and if $R = 250$ cm, the capacity gain is reduced to 1.45. Furthermore, compared with the BF array, the SM array has a more robust performance over antenna misalignment, because of the wider beamwidth.

1. Introduction

Millimeter wave (mmW) has been attracting increased attention in the 5th-generation (5G) wireless systems [1], because huge amount of raw bandwidth is available for wireless communication services. In addition, the small wavelengths of this band make the use of a large number of antenna elements at the base station as well as the user equipment to formulate a multiple-input multiple-output (MIMO) system possible. Although MIMO techniques have been widely employed in cellular and wireless local area network systems working at sub-6 GHz [2–4], the potential and realization of MIMO technique in mmW band were still not fully understood, considering the unique multipath propagation characteristics and the increased path loss over the lower frequency bands used in current 3G/4G wireless communication.

Spatial multiplexing (SM) and beamforming (BF) are the most commonly used two approaches to realize a MIMO system. In a SM system, the whole information stream is divided into multiple pieces [5], each of which is transmitted simultaneously and parallel on the same frequency band through different antenna ports. The multiplexing gain can be obtained by exploiting the spatial difference of the channel

response in different transmit (Tx)-receive (Rx) element pair. On the other hand, in the mmW band, the propagation loss is higher compared to the lower frequencies; thus, the high-gain antenna arrays are expected to compensate for the increased path loss. In the systems with MIMO technique working at lower frequencies, such as LTE, digital BF with per-element weight adaptation to provide the best matching to the instantaneous channel state information can be realized. However, for mmW systems with large number of antenna elements, such a digital BF is infeasible in the near term, due to the cost of the large number of RF chains and mixed signal components [6, 7]. Thus, BF in this paper is considered to be realized at analog domain, where networks of phase shifter are used to formulate a directed beam patterns, focusing the array gain in the dominant propagation directions.

Some researches have been conducted on the performance of SM and BF in the mmW communications. The effect of BF on the improvement of some channel metrics of the indoor 60 GHz band system has been studied by measurements [8]; the performance of random beamforming has been analyzed for sparse mmW multiuser downlink channel based on a uniform random multipath channel model [9]. The feasibility of indoor mmW MIMO has been

investigated by ray-tracing based channel modeling [10, 11], by virtual antenna array based channel measurement [11, 12], and also by a 2×2 microstrip array in an underground mine environment [13]. A generalized spatial modulation MIMO scheme in indoor line-of-sight (LOS) mmW communication at 60 GHz is proposed and analyzed [14]. Furthermore, the suitability of SM and BF in the mmW band has also been studied by measurement-based statistical channel modeling [15, 16] in outdoor cellular environments and by the plane and spherical wave expressed channel modeling along with the virtual array based indoor experiments [17]. The performance of a hybrid transmission combining BF and SM in mmW communication is also analyzed based on a ray-tracing method in both LOS and multipath environment [18].

Given the Tx and Rx antenna aperture size and working frequency, the maximum number of antenna elements that could be supported is fixed. If more antenna ports are formulated for SM, the number of parallel subchannels will be increased but with a reduced subarray gain; on the contrary, if more antenna elements are used for BF, the array gain will be increased but the number of multiplexing channels will be reduced. Thus, a tradeoff between SM and BF should be made in the massive antenna mmW wireless systems, and which one has a better capacity performance depends on the radiation characteristics of the antennas, the multipath distribution, and the path loss of the particular environment. To make the tradeoff between SM and BF at mmW frequencies, channel measurements with respect to realistic antenna array configurations and propagation environments are required, yet, to date, there has been little such work about the performance comparisons between SM and BF in the mmW wireless communications.

In this paper, we provide the measurement-based channel capacity comparison between SM and BF under realistic antenna arrays, with the same Tx power, the same array position, and the same propagation condition. In particular, given the size of antenna aperture, there are totally 16 linearly polarized antenna elements working at 28 GHz, realized by a kind of L-probe microstrip antenna [19]. In the SM system, it is divided into 4 subarrays, and each consists of 4 elements, which corresponds to a 4×4 MIMO system. In the BF system, the antenna array is constructed by the whole 16 elements, which corresponds to a SISO system but with a larger array gain than that of the SM system. The results in this paper provide guidance for the design and application of SM and BF subarrays in the massive MIMO systems in the short-range indoor mmW scenarios, with the realistic array geometry, propagation characteristic, and SNR.

2. SM and BF Arrays Design

A coplanar waveguide (CPW) feed microstrip antenna array realized by a single layer printed circuit board technique is designed, because of the low material cost, planer structure, and ease of fabrication. Firstly, a subarray composed of 4 elements is constructed, as shown in Figure 1. Here, the defected ground technique is adopted to get a better impedance matching.

TABLE 1: Dimensions of the antenna element.

Parameter	Value (mm)
W	4.4
L	3.3
F_p	1.7
F_w	1.2
F_1	2.5
g_2	0.15
T	0.508
C_1	0.56
H_1	9
C_2	1.5
W_2	1.2
W_3	0.15
S_1	1.65
S_2	2
W_1	1.2
g	0.15
V_1	8.4

The dimensions of this 4-element array are shown in Table 1, and the detailed meaning of those parameters can be found in [19]. Based on this 4-element subarray, the SM array and BF array are constructed. A photograph of the fabricated SM and BF antenna is shown in Figure 2. The Rogers Duroid 5880 substrate ($\epsilon_r = 2.2$ and $\tan \delta = 0.0009$) is selected with a thickness of 0.508 mm.

The antennas are modeled and simulated using the Ansoft's HFSS full-wave simulator. The reflection and transmission coefficients are given in Figures 3 and 4, respectively. Those figures show that the measured and simulated S-parameters of the SM and BF array basically agree with each other. The measured return losses of the 4 ports in the SM antenna and that of the BF antenna are all below the -10 dB between 27.2 GHz and 29 GHz. Moreover, all the measured isolations among the 4 ports of the SM antenna are better than -25 dB.

In Figure 5 the array gain of the BF antenna and the SM antenna in different ports are illustrated, which shows that good agreements between the simulated and the measured results exist. The gain of the BF array is about 5 dB higher than that of the SM array, which has small difference in different port due to tiny deviations in the dimensions and the variations in the feeding lines of the fabricated antennas. In Figure 6, the measured yz plane radiation characteristics of the two arrays at 28 GHz are illustrated. It is shown that the SM antenna has a wider radiation pattern than that of the BF antenna; specifically, the 3 dB beamwidth of the SM array is 37.9° and that of the BF array is only 12.3° .

3. Measurement Experiment

3.1. Experiment Setup. The measurement scenario is an office room located on the 9th floor of the main building of the Communication University of China, with the dimensions

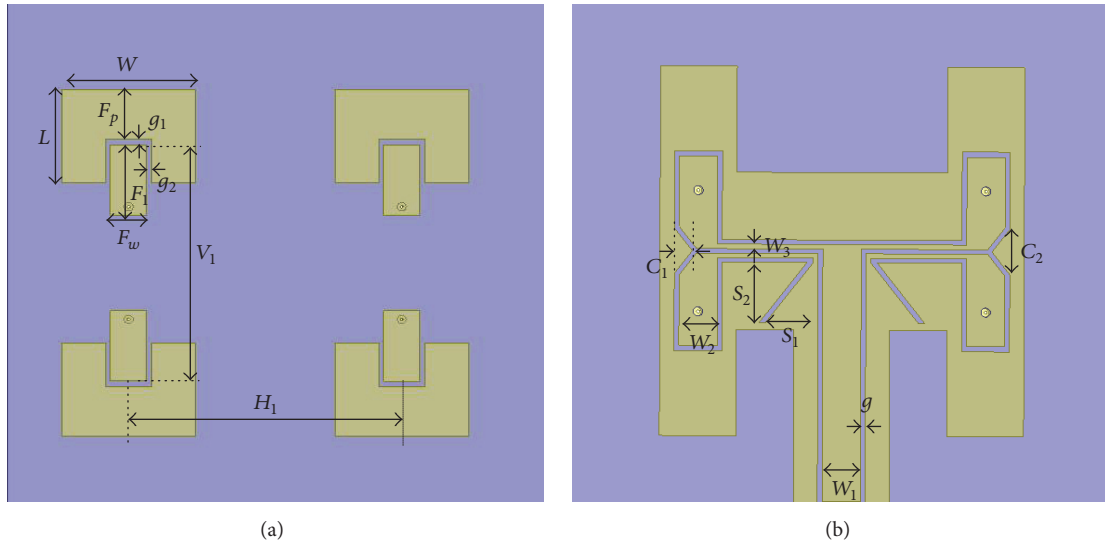


FIGURE 1: Geometry of the subarray composed of 4 elements. (a) Top view. (b) Bottom view.

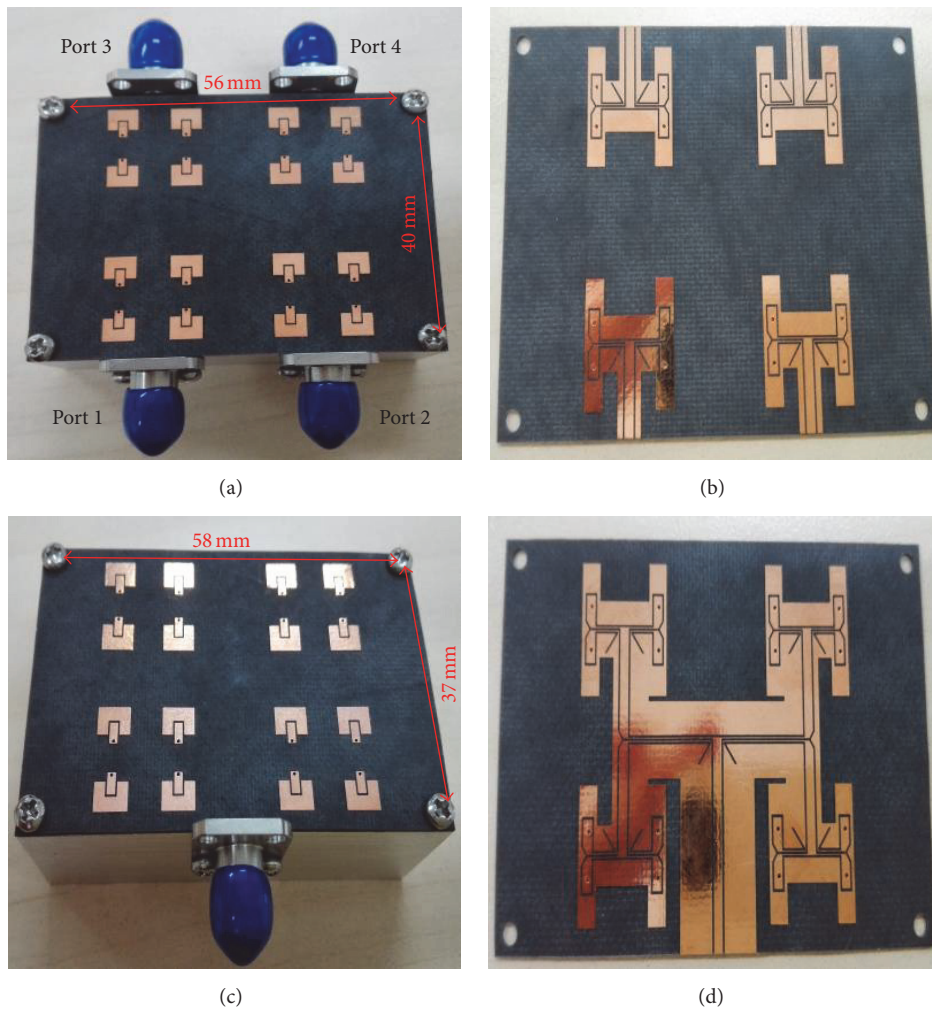


FIGURE 2: The fabricated SM and BF antenna. (a) Perspective view and (b) bottom view of the 4-port SM array. (c) Perspective view and (d) bottom view of the one-port BF array.

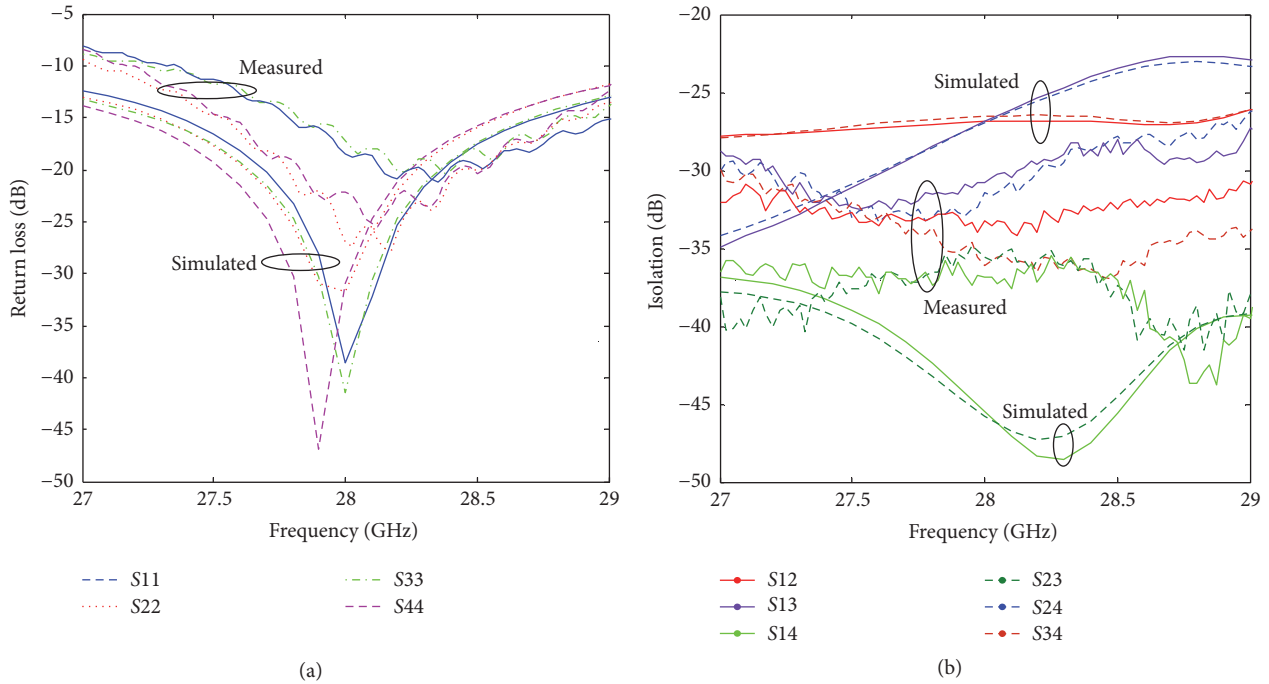


FIGURE 3: Simulated and measured S-parameters of the SM array. (a) Return loss. (b) Isolation.

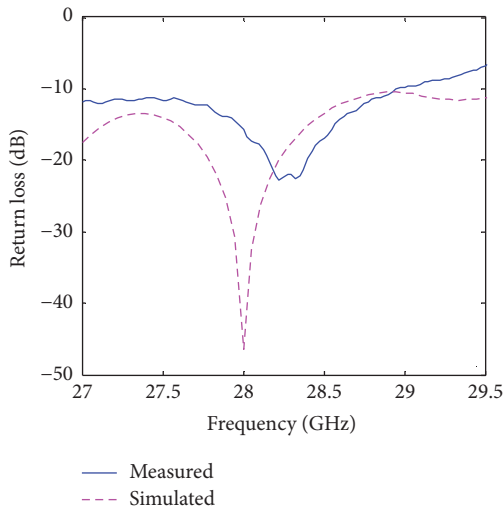


FIGURE 4: Simulated and measured S-parameters of the BF array.

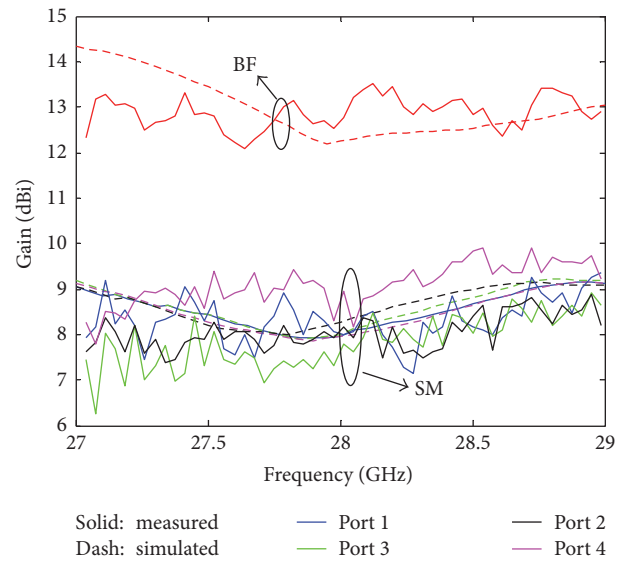


FIGURE 5: Simulated and measured gains of the SM and BF antenna array.

of $2.6\text{ m} \times 5.6\text{ m} \times 3.2\text{ m}$ ($W \times L \times H$). As shown in Figure 7, along the walls, there are some tables, computers, and experiment devices. The office room has one wooden door and several glass windows. The frame works of the building are reinforced concrete, and the walls and floors consist mainly of brick and plaster. During the experiment, the Tx antenna is fixed, and the Rx antenna is located in different positions. The scattering parameters are measured by a vector network analyzer (VNA) Agilent N5234A. Firstly, the fabricated SM array is employed at both the Tx and Rx ends, and each Tx port and Rx port are connected to the input and output ports of the VNA. The system is thoroughly

calibrated to eliminate frequency-dependent attenuation and phase distortion. Between the Tx and Rx array, there are no obstacles to insure LOS propagation existed for all positions.

The real-time S-parameters from VNA are saved by a computer automatically. The 4×4 channel matrix \mathbf{H} was determined by measuring the transfer parameters between each pair of the Tx and Rx antenna ports, with the remaining ports terminated by matched loads. For each position of the

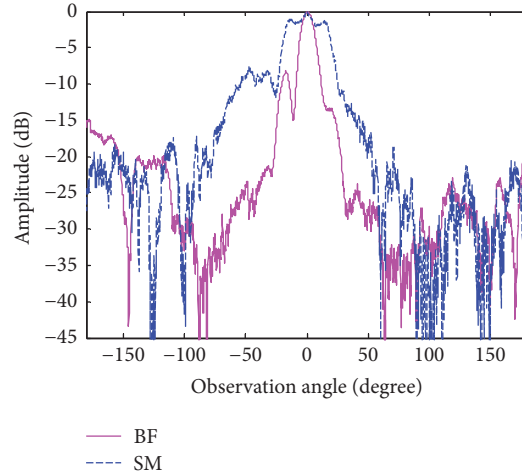


FIGURE 6: Measured radiation patterns of the SM and BF antenna array.

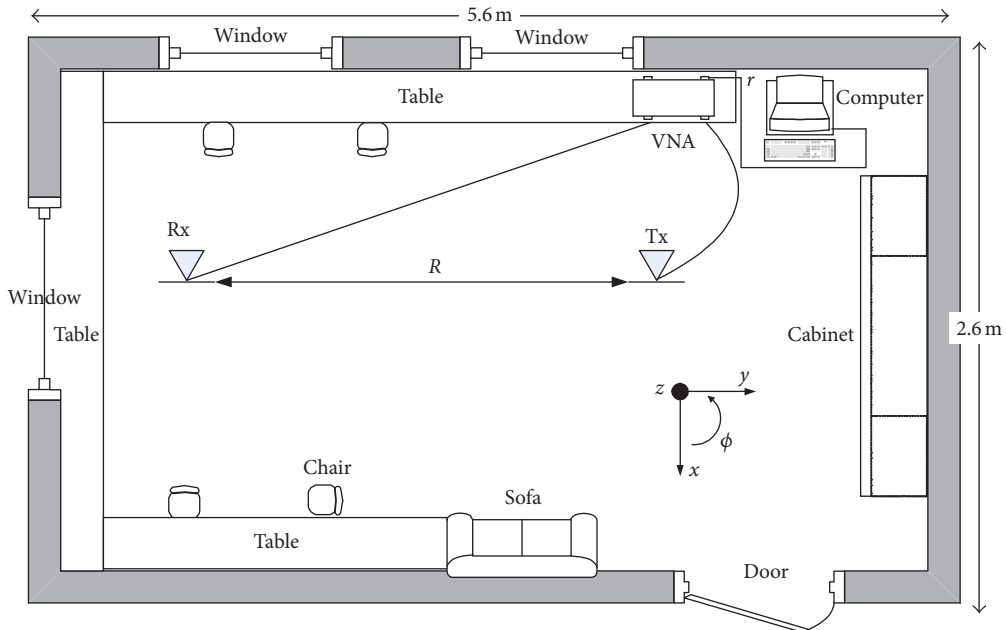


FIGURE 7: Measurement location and the schematic of the room.

Rx antenna, the data is recorded over 40 seconds with the sampling interval of 1 second. Over the working bandwidth of 27.2–29 GHz, with step sizes of 12.5 MHz, there are totally 145 frequency points. Thus, for each Tx and Rx antenna pair, the total number of measured channels is $145 \times 40 = 5800$. Then the measurement procedure is repeated for both the Tx and Rx ends are equipped with the BF array, with exactly the same Tx power and the antenna position. The personnel movement is kept to a minimum to ensure the statistical stationarity of the propagation.

3.2. Results. The performance of a MIMO system is generally evaluated by the channel capacity. If the channel state information is not available at the Tx end, the equal power allocation at each port is generally used, and the corresponding channel capacity can be computed by [5]

$$C = \log_2 \det \left(\mathbf{I} + \left(\frac{\text{SNR}}{n_T} \right) \mathbf{H} \mathbf{H}^\dagger \right), \quad (1)$$

where \mathbf{I} is the identity matrix, SNR is the signal-to-noise ratio, n_T is the number of transmit antennas, and \mathbf{H}^\dagger means the transpose conjugate of \mathbf{H} . In most of the pervious works, the channel matrix is normalized, and the capacity is computed with the assumed SNR values. By this method, only the effect of richness of the multipath on MIMO performance can be evaluated.

In this paper, we also used the normalized channel matrix; however, the real values of average received SNR for different antenna positions are measured and used in the capacity calculation, through which the effect of actual received power on the system property can be illustrated.

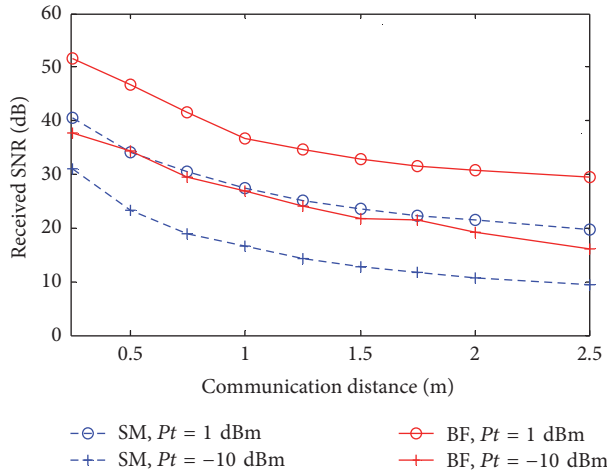


FIGURE 8: Relationship between the averaged received SNR and R .

Firstly, the variations of SNR and channel capacity with communication distance R are investigated. During the measurement, both the Tx and Rx antennas are vertically polarized and with the equal height to the floor $h_t = h_r = 118$ cm. The maximum radiation directions of Tx and Rx antennas are aligned to obtain the best LOS signal level. The position of the Tx antenna is fix, and the Rx antenna is moved away gradually from the Tx antenna, with R increased from 25 cm to 250 cm. To get the value of SNR, we measured the received power of the background noise and that of the transmitted signal, individually, and then calculated the ratio between them. The relationship between the received SNR and communication distance is shown in Figure 8, for each position, the SNR value is an averaged result over all the 5800 samples, and the result of SM array is the averaged value over 4 ports. As can be seen from Figure 8, for short range with R smaller than 1 m, the decreasing slope of SNR curve is obviously larger than that of the larger range. Furthermore, the SNR obtained by the BF array is about 7–10 dB larger than that of the SM array, which is basically consistent with the measured array gains.

It is well known that, besides SNR, the MIMO capacity also depends heavily on correlation properties of the channel matrix, which is decided by the complex interaction between antenna radiation characteristic and the surrounding environment. A MIMO system can only perform well if the channel elements are statistically independent [20]. In Figure 9, the Rx correlation coefficients (CCs) with respect to Tx port 1 of the SM array are described, and the results corresponding to other Tx ports are similar. Figure 9 tells us that, for $R = 25$ cm, the CCs are comparatively high due to the dominating contribution of the LOS signal, and, for larger communication distance, the CCs get smaller, because the contributions of multipath components get larger. However, even the CCs in Figure 9(a) are not very high, which have almost no negative impact on the performance of the MIMO system.

In Figure 10, the cumulative distribution functions (CDFs) of the channel capacity corresponding to the $4 \times$

4 SM MIMO system and that of the BF SISO system are compared, with the increasing of communication distance. For each curve, it is the statistical result based on 5800 samples. The corresponding ergodic capacity has also been calculated based on these CDF results. From Figure 10(a), for $P_t = 1$ dBm, if $R = 25$ cm, the ergodic capacity of the SM system is 2.76 times that of the BF system; however, if $R = 250$ cm, the capacity gain is reduced to only 1.45. From Figure 10(b), for $P_t = -10$ dBm, the corresponding ergodic capacity gain drops slightly, 2.43 and 1.37, respectively. Results in Figure 10 indicate that, in the SM array MIMO system, large capacity gain can only be obtained with a sufficiently high SNR.

Figure 10 gives the results of the Tx and Rx antennas best aligned to get the largest SNR; however, in the actual communications, the antennas cannot be always adjusted to the best direction. Thus, the performances of these arrays with angle deviations from the best one are also investigated in Figure 11, in the azimuth (φ) and elevation (θ) angle plane, individually. In the measurement of Figure 11(a), $P_t = 1$ dBm, h_t and h_r are also set to 118 cm, and R is kept as a constant of 1 m. The position of Rx is changed, to make the azimuth deviation angle with respect to the maximum radiation direction gradually increase from 0° to 25° . As to the test in Figure 11(b), the position of Tx is also fixed with $h_t = 118$ cm, h_r is increased gradually to get an incremental elevation angle deviation, and the horizontal distance between the Tx and Rx is kept also as 1 m.

Figure 11 shows that, with the increasing of angle deviation from both the horizontal and vertical planes, the channel capacity obviously declines; however, it behaves differently for different arrays and shows a strong dependence on the antenna radiation pattern. In particular, the SM array has a more robust performance over the angle deviation in the horizontal plane; as calculated by the data in Figure 11(a), if $\varphi = 10^\circ$, the ergodic capacity drop is only 1.85% for the SM array, whereas the value for the BF array is 27.03%. In the vertical plane, performances of both arrays degrade quickly with the increase of θ , and if $\theta = 10^\circ$, as calculated by the data in Figure 11(b), the drop in ergodic capacity will reach 30.53% and 26.56% for the SM array and BF array, respectively. The results in Figure 11 could be explained that, in the horizontal plane, the SM array has a wider radiation pattern than that of the BF array, but, in the vertical plane, there are no obvious differences.

4. Conclusion

A BF SISO array and a SM MIMO array with 4 ports working at 28 GHz are designed and fabricated, with totally 16 antenna elements. To make a comparison and tradeoff between the channel capacities of those arrays, their channel responses are measured and compared in an indoor office room. The dependence of the channel capacity of both arrays on communication distance is computed with the actual received SNR. Furthermore, the effects of antenna array misalignment on the degradation of the channel capacity are also investigated, both in the azimuthal and in the elevation angle plane. It is found that although the BF array can get a

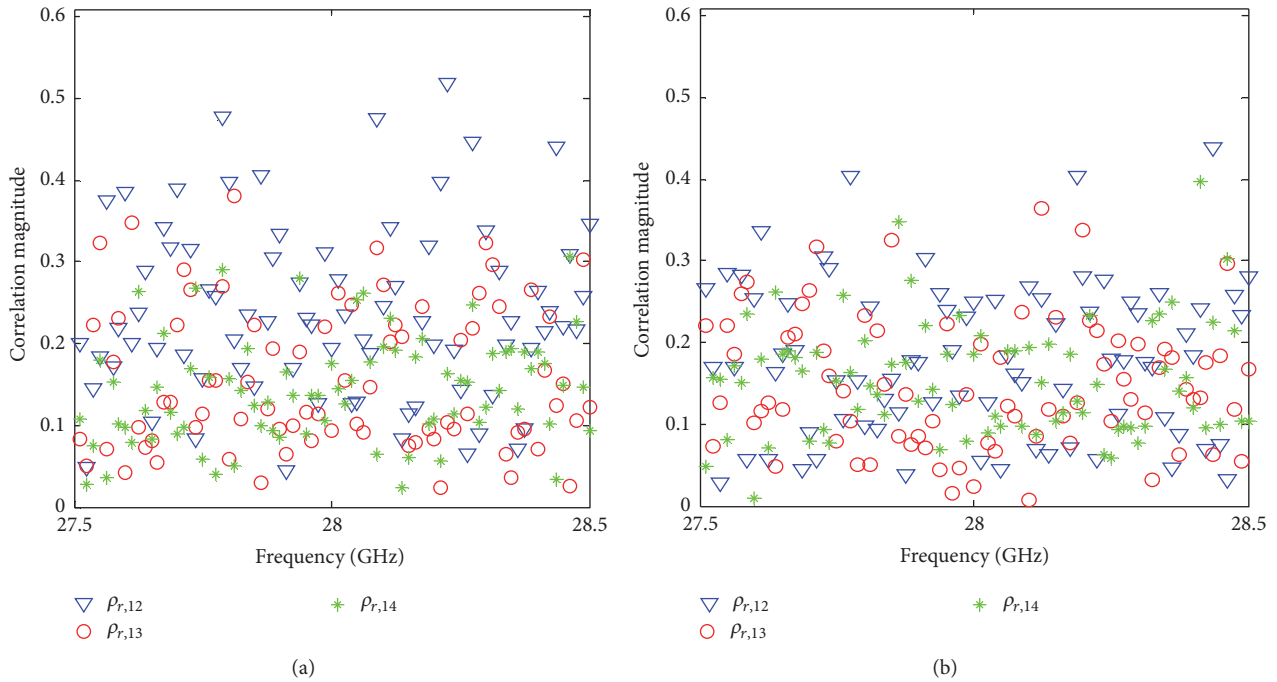


FIGURE 9: Dependence of the receive correlation coefficients on frequency. (a) $R = 25$ cm. (b) $R = 125$ cm.

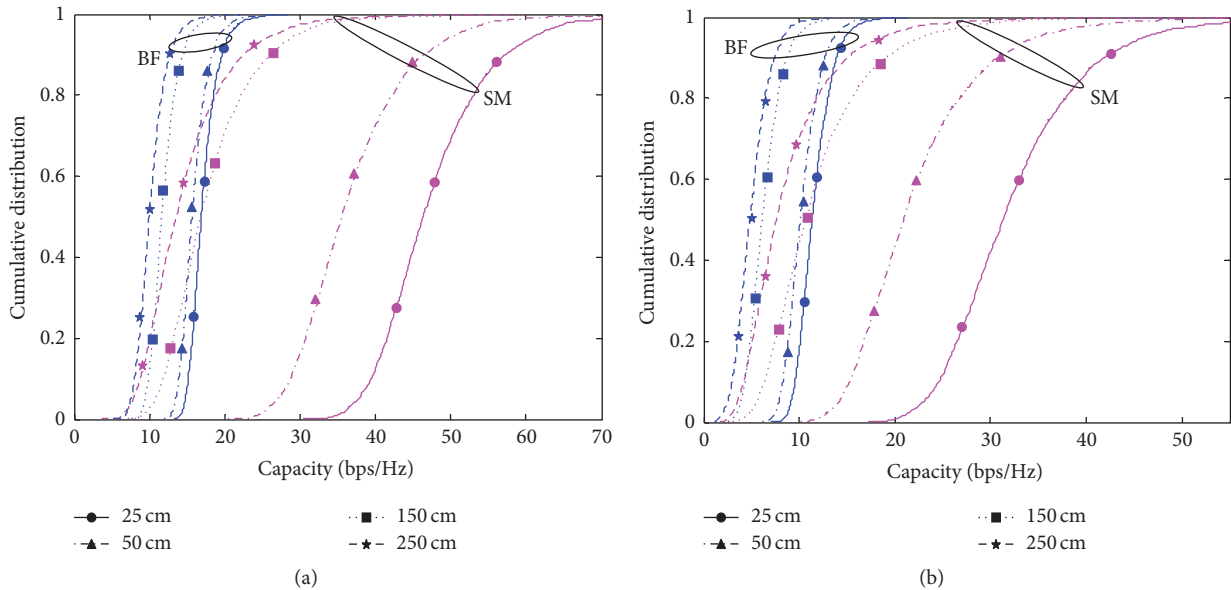


FIGURE 10: Dependence of capacity on R . (a) $P_t = 1$ dBm. (b) $P_t = -10$ dBm.

concentrated and directed beam pattern to get an increased SNR, the SM array can still get a larger channel capacity, thanks to the spatial multiplexing gain obtained in the MIMO channel, and thus the incoming data stream can be divided into several parallel substreams transmitted simultaneously. High spatial multiplexing gain obtained by the SM array in the indoor office room in 28 GHz can be explained that, for shorter distance, such as $R = 0.25$ m, enough difference of the channel responses in space can be obtained since the subarray spacing is about 2.1λ , and, for longer distance, the channel

provides enough multipath angular spread which is beneficial for the channel decorrelation.

Furthermore, the SM array has a more robust performance over the antenna misalignment because of the wider radiation pattern. However, the large channel capacity gain of the SM array can only be obtained with a sufficiently high SNR. Here, we only considered a mmW array with totally 16 antenna elements, for the arrays with larger size and more elements, there will be more realizations of the MIMO array, and which one has a better and more robust performance

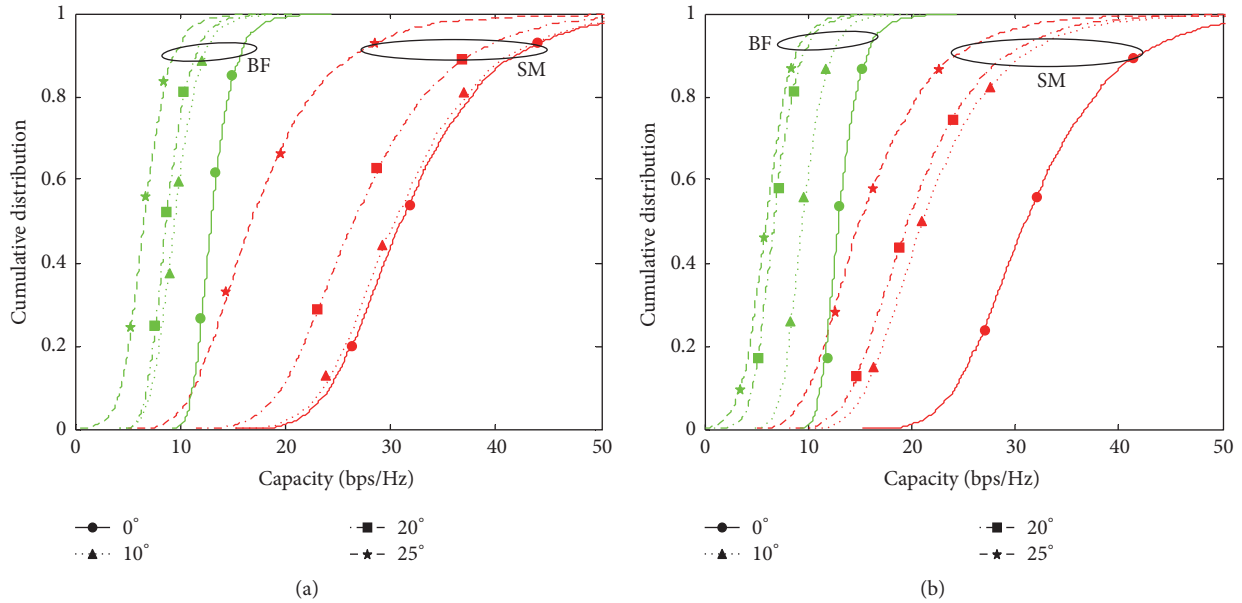


FIGURE 11: Dependence of capacity on the deviation angle. (a) Azimuth plane. (b) Elevation plane.

will be investigated in the future by measurement as well as theoretical modeling.

Conflicts of Interest

The authors declare that there are no conflicts of interest regarding the publication of this paper.

Acknowledgments

This work was supported by the National Natural Science Foundations of China (Grant no. 61201235) and the Young Talents Program of Beijing Universities (no. YETP0595).

References

- [1] F. Boccardi, R. Heath Jr., A. Lozano, T. L. Marzetta, and P. Popovski, "Five disruptive technology directions for 5G," *IEEE Communications Magazine*, vol. 52, no. 2, pp. 74–80, 2014.
- [2] H. Sampath, S. Talwar, J. Tellado, V. Erceg, and A. Paulraj, "A fourth-generation MIMO-OFDM broadband wireless system: design, performance, and field trial results," *IEEE Communications Magazine*, vol. 40, no. 9, pp. 143–149, 2002.
- [3] Q. Li, G. Li, W. Lee et al., "MIMO techniques in WiMAX and LTE: a feature overview," *IEEE Communications Magazine*, vol. 48, no. 5, pp. 86–92, 2010.
- [4] J. Kim and I. Lee, "802.11 WLAN: history and new enabling MIMO techniques for next generation standards," *IEEE Communications Magazine*, vol. 53, no. 3, pp. 134–140, 2015.
- [5] G. J. Foschini and M. J. Gans, "On limits of wireless communications in a fading environment when using multiple antennas," *Wireless Personal Communications*, vol. 6, no. 3, pp. 311–335, 1998.
- [6] A. Alkhateeb, J. Mo, N. González-Prelcic, and R. W. Heath Jr., "MIMO precoding and combining solutions for millimeter-wave systems," *IEEE Communications Magazine*, vol. 52, no. 12, pp. 122–131, 2014.
- [7] J. Singh and S. Ramakrishna, "On the feasibility of codebook-based beamforming in millimeter wave systems with multiple antenna arrays," *IEEE Transactions on Wireless Communications*, vol. 14, no. 5, pp. 2670–2683, 2015.
- [8] S. Wyne, K. Haneda, S. Ranvier, F. Tufvesson, and A. F. Molisch, "Beamforming effects on measured mm-wave channel characteristics," *IEEE Transactions on Wireless Communications*, vol. 10, no. 11, pp. 3553–3559, 2011.
- [9] G. Lee, Y. Sung, and M. Kountouris, "On the performance of random beamforming in sparse millimeter wave channels," *IEEE Journal on Selected Topics in Signal Processing*, vol. 10, no. 3, pp. 560–575, 2016.
- [10] E. Torkildson, U. Madhow, and M. Rodwell, "Indoor millimeter wave MIMO: feasibility and performance," *IEEE Transactions on Wireless Communications*, vol. 10, no. 12, pp. 4150–4160, 2011.
- [11] M.-T. Martinez-Ingles, D. P. Gaillot, J. Pascual-Garcia, J.-M. Molina-Garcia-Pardo, M. Lienard, and J.-V. Rodríguez, "Deterministic and experimental indoor mmW channel modeling," *IEEE Antennas and Wireless Propagation Letters*, vol. 13, pp. 1047–1050, 2014.
- [12] S. Ranvier, C. Icheln, and P. Vainikainen, "Measurement-based mutual information analysis of MIMO antenna selection in the 60-GHz band," *IEEE Antennas and Wireless Propagation Letters*, vol. 8, pp. 686–689, 2009.
- [13] I. Ben Mabrouk, J. Hautcoeur, L. Talbi, M. Nedil, and K. Hettak, "Feasibility of a millimeter-wave MIMO System for short-range wireless communications in an underground gold mine," *IEEE Transactions on Antennas and Propagation*, vol. 61, no. 8, pp. 4296–4305, 2013.
- [14] P. Liu, M. Di Renzo, and A. Springer, "Line-of-sight spatial modulation for indoor mmWave communication at 60 GHz," *IEEE Transactions on Wireless Communications*, vol. 15, no. 11, pp. 7373–7389, 2016.
- [15] M. R. Akdeniz, Y. Liu, M. K. Samimi et al., "Millimeter wave channel modeling and cellular capacity evaluation," *IEEE Journal on Selected Areas in Communications*, vol. 32, no. 6, pp. 1164–1179, 2014.

- [16] S. Sun, T. S. Rappaport, R. W. Heath, A. Nix, and S. Rangan, "MIMO for millimeter-wave wireless communications: beamforming, spatial multiplexing, or both?" *IEEE Communications Magazine*, vol. 52, no. 12, pp. 110–121, 2014.
- [17] K. Haneda, C. Gustafson, and S. Wyne, "60 GHz spatial radio transmission: multiplexing or beamforming?" *IEEE Transactions on Antennas and Propagation*, vol. 61, no. 11, pp. 5735–5743, 2013.
- [18] S. J. Lee and W. Y. Lee, "Capacity of multiple beamformed spatial stream transmission in millimetre-wave communication channels," *IET Communications*, vol. 7, no. 12, pp. 1263–1268, 2013.
- [19] M. Li and K.-M. Luk, "Low-cost wideband microstrip antenna array for 60-GHz applications," *IEEE Transactions on Antennas and Propagation*, vol. 62, no. 6, pp. 3012–3018, 2014.
- [20] D. Piao, L. Yang, Q. Guo, Y. Mao, and Z. Li, "Measurement-based performance comparison of colocated tripolarized loop and dipole antennas" *IEEE Transactions on Antennas and Propagation*, vol. 63, no. 8, pp. 3371–3379, 2015.

Research Article

Novel Method for Optimal Synthesis of 5G Millimeter Wave Linear Antenna Array

Zarko Rosic,¹ Olivera Mihic,¹ Danijela Aleksic,² and Dejan Drajić³

¹Faculty of Organizational Sciences, University of Belgrade, Jove Ilića 153, 11000 Belgrade, Serbia

²Faculty of Technical Sciences, University of Kragujevac, Svetog Save 55, 32000 Cacak, Serbia

³Faculty of Electrical Engineering, University of Belgrade, Bulevar Kralja Aleksandra 73, 11000 Belgrade, Serbia

Correspondence should be addressed to Zarko Rosic; zarko.rosic88@gmail.com

Received 10 December 2016; Accepted 5 February 2017; Published 13 March 2017

Academic Editor: Stefan R. Panic

Copyright © 2017 Zarko Rosic et al. This is an open access article distributed under the Creative Commons Attribution License, which permits unrestricted use, distribution, and reproduction in any medium, provided the original work is properly cited.

We will propose a useful method for 5G mm wave antenna array synthesis, based on Genetic Algorithm for the synthesis of linear array with nonuniform interelement spacing. Our design method was used to obtain the optimal position of the elements in order to get the minimum side lobe level and nulls in desired directions. The simulation results verify that proposed method outperforms the previously published methods in terms of suppression side lobe level while maintaining nulls in specified directions. The flexibility of proposed algorithm shows good potential for the antenna array synthesis.

1. Introduction

In order to satisfy necessary 5G quality-of-standard criteria and meet user mobility, due to the higher path loss at mm wave frequency range, multiple antenna arrays are typically used in outdoor mm wave systems for providing additional gain [1, 2]. They play an important role in detecting and processing signals arriving from different directions. The performance of the systems depends on the efficient design of the antenna arrays. The desired radiation pattern can be realized by choosing geometrical shape of antenna array, element excitation amplitude, element excitation phase, and element spacing. The objectives in design of the antenna arrays are archiving minimum side lobe level (SLL) and narrow first null beam width (FNBW). Interference issues will become of crucial importance for coexistence of 5G devices, since number of mm wave devices will grow extensively in near future [3]. The increasing growth of 5G devices number will prompt the study of array pattern nulling techniques. This problem will reach its culmination in future dense mm wave application, such as for the 60 GHz dense indoor communication, and various outdoor mm wave 5G communication in densely populated urban areas [4]. So the goal of antenna array synthesis is to achieve the minimum SLL with narrow

FNBW and obtaining narrow or broad nulls in directions of interfering signals. The broad nulls are needed when the direction of arrival of interference may vary slightly with time.

For the linear array geometry, by optimizing the spacing between the elements while keeping the uniform excitation we can suppress side lobe level while preserving the gain of the main beam and can control nulling.

Methods used for the antenna array synthesis can be classified in two categories: deterministic and stochastic. There are several deterministic methods: Schelkunoff Polynomial Method [5], Dolph-Chebyshev Method [6, 7], Woodward-Lawson Method [8, 9], and Fourier Transform Method [6, 8, 9]. In modern research the most common methods are stochastic, because stochastic methods can almost all be proven to find a global minimum with asymptotic convergence in probability. The biggest advantages of using stochastic methods are their ability in dealing with large number of optimization parameters and avoiding getting stuck in local minima. Some of the methods used for the antenna array synthesis are Evolutionary Algorithms (EA) [10], Genetic Algorithms (GA) [11–13], Tabu Search (TS) [11, 14], Particle Swarm Optimization (PSO) [15–17], Ant Colony Optimization (ACO) [18], Nature-Inspired Cuckoo Search

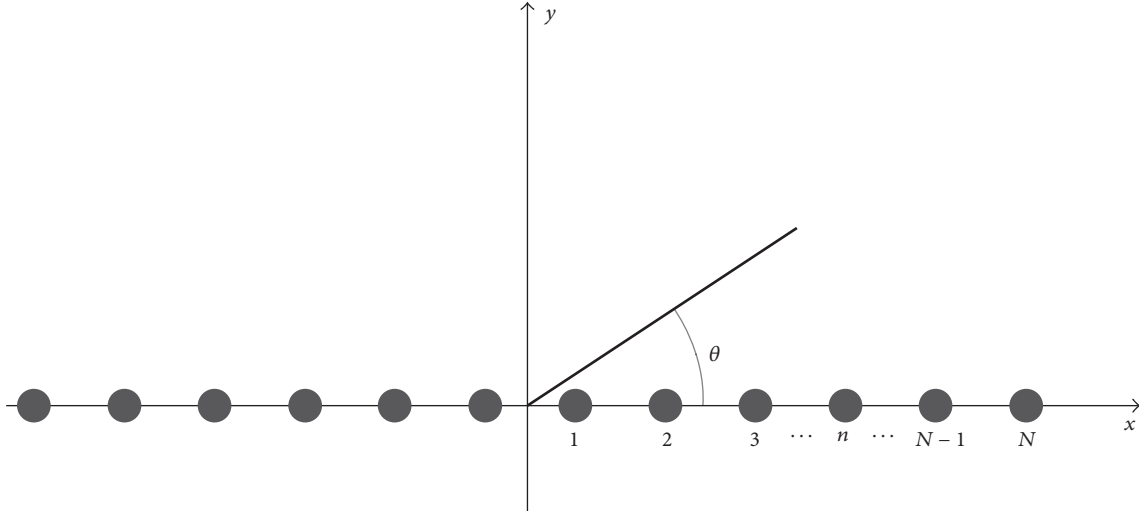


FIGURE 1: Geometry of $2N$ -element linear antenna array.

(CS) [19, 20], Combination of Global and Local Search [21], and Cat Swarm Optimization [22]. All the above-mentioned methods have shown the capability of searching for global solution in electromagnetic optimization problems.

In this paper, we proposed a useful method based on combination of two global searches. The main idea comes from method based on combination of global and local search [21]. Changing local search into global search we avoid getting stuck in local minimum and this leads to better exploration of feasible region. Better exploration leads to better solution of optimization problem. Presented algorithm was used to obtain the optimal position of the elements in order to get the minimum side lobe level and nulls in desired directions. We applied for optimization the same radiation pattern requirements of the selected papers. The simulation results reveal that design of antenna arrays using the presented method provides considerable enhancements compared with the synthesis obtained from other published methods. In this approach we will concern arrays of isotropic point sources; this is of great value because the pattern of any antenna can be regarded as being produced by an array of point sources.

Description of antenna array design problem is given in Section 2. In Section 3, a description of the used algorithm is presented. Results are presented in Section 4. Finally, the conclusion of this work is presented in Section 5.

2. Problem Formulation

The antenna array radiation pattern (RP) may be found according to the pattern multiplication theorem (see, e.g., Ch. 6 from [6, 24] and Ch. 3 from [25]):

$$\text{RP} = \text{EL} \cdot \text{AF}. \quad (1)$$

EL (element pattern) is the pattern of the individual array element.

AF (array factor) is a function dependent on the physical placement of antenna elements, amplitude, and phase of excitation.

If we replace each element of the antenna array with an isotropic point source the resulting pattern is the array factor, because the element pattern of isotropic point source is equal to 1. The geometry of the linear antenna array with $2N$ isotropic elements placed symmetrically along the x -axis is given in Figure 1.

In this paper linear antenna array has identical elements with nonuniform interelement spacing and uniform excitation. Array factor in the azimuth plane can be expressed as follows (for more see [6, 8, 9, 24–26]):

$$\text{AF}(\theta) = 2 \sum_{n=1}^N I_n \cos [kd_n \sin(\theta) + \varphi_n], \quad (2)$$

where $k = 2\pi/\lambda$ is wave number, λ is the wavelength, I_n is excitation amplitude of n th element, φ_n is excitation phase of n th element, d_n is location of n th element, and θ is angle between the line of observer and the source position.

If we assume a uniform excitation of phase as $\varphi_n = 0$ for each antenna array element, the array factor can be written in a simple form as follows:

$$\text{AF}(\theta) = 2 \sum_{n=1}^N I_n \cos [kd_n \sin(\theta)]. \quad (3)$$

In the field of electromagnetism the decibel (dB) is often used as a unit of measurement for array factor. Normalized array factor and normalized array factor in dB are given by

$$(\text{AF}(\theta))_{\text{norm}} = \frac{|\text{AF}(\theta)|}{|\max(\text{AF}(\theta))|}, \quad (4)$$

$$(\text{AF}(\theta))_{\text{norm,db}} = 20 \log \frac{|\text{AF}(\theta)|}{|\max(\text{AF}(\theta))|}. \quad (5)$$

```

Begin
Set an initial solution  $x^1$ ;
Define  $k_{\max}$ ,  $R$  and  $l_{\max}$ ;
Set  $k \leftarrow 1, l \leftarrow 1, \text{SLL}^* = 0, x^* = 0$ ;
if (cost function is with nulls) set  $\text{depp}_k^* = -60$  dB;
Global search for  $\theta$ . Solution of the search is  $\theta^1$ ;
While ( $l < l_{\max}$ )
  Global search for  $x$ . Solution of the search is  $x^{l+1}$ ;
  Global search for  $\theta$ . Solution of the search is  $\theta^{l+1}$ ;
  Set  $\text{SLL}^{l+1} = \text{AF}(\theta^{l+1})_{\text{norm}}$ ;
  if (cost function is with nulls)  $\text{depp}_k = \text{AF}(\theta_k)_{\text{norm}}$ ;
  end
  if (cost function is with nulls)
    if ( $\text{SLL}^{l+1}$  is better than  $\text{SLL}^*$  and  $\text{depp}_k < \text{depp}_k^*$ )
      set  $k \leftarrow 1, \text{SLL}^* = \text{SLL}^{l+1}$  and  $x^* = x^{l+1}$ ; end
    else
      if ( $\text{SLL}^{l+1}$  is better than  $\text{SLL}^*$ ) set  $k \leftarrow 1, \text{SLL}^* = \text{SLL}^{l+1}$  and  $x^* = x^{l+1}$ ; end
    end
  If ( $k \geq k_{\max}$ ) STOP;
  end
   $l \leftarrow l + 1$ ;
   $k \leftarrow k + 1$ ;
end
Outputs of the algorithm are  $\text{SLL}^*$  and  $x^*$ ;
end

```

ALGORITHM 1

3. Algorithm

The presented algorithm is applied to achieve the desired radiation pattern with minimum SLL and narrow or broad nulls in specified directions. Our approach uses a combination of two global searches: global search with respect to θ and global search with respect to x . The global searches were performed using Genetic Algorithm with existing function “ga” from MATLAB software package (R2016a). The global search with respect to θ was performed on region $[\theta_{11}, \theta_{12}]$ with fixed permanent solution x^l for the cost function (4). With this global search we locate maximum side lobe level.

The cost function for step global search for x following expression was used:

$$\text{Cost} = \max \left(\text{AF}(\theta)_{\text{norm}} \Big|_{\theta_{11}}^{\theta_{12}} \right) + \sum_k \text{AF}(\theta_k)_{\text{norm}}. \quad (6)$$

First term in (6) is employed to minimize the side lobe level between the desired angles θ_{11} and θ_{12} , whereas the second one is for achieving deep nulls in desired directions θ_k . For reducing mutual coupling effects between the elements of the antenna array the following conditions must be satisfied:

$$\begin{aligned} |x_i - x_j| &> 0.25\lambda, \\ \min(x_i) &> 0.125\lambda, \quad i = 1, 2, \dots, N, \quad i \neq j. \end{aligned} \quad (7)$$

The global search with respect to x on a small neighbourhood of current solution was performed with fixed θ^l . Lower

and upper bounds for each coordinate of vector x^l are defined using the following expression:

$$\begin{aligned} \text{LOW}_i &= (x_i^l - R), \quad i \in N, \quad R \in \mathfrak{R}, \\ \text{UP}_i &= (x_i^l + R), \quad i \in N, \quad R \in \mathfrak{R}. \end{aligned} \quad (8)$$

Pseudocode of proposed algorithm is given in Algorithm 1.

4. Simulation Results

In the first experiment we performed the synthesis of $2N = 28$ element antenna array in order to get the minimum side lobe level and nulls at $\theta_1 = 30^\circ$, $\theta_2 = 32.5^\circ$, and, $\theta_3 = 35^\circ$. In this paper we performed experiments for $R = 0.05$ and 0.1 (with respect to $\lambda/2$) where $\theta_{11} = 4^\circ$ and $\theta_{12} = 90^\circ$.

The cost function for the algorithm following expression was used:

$$\text{Cost} = \max \left(\text{AF}(\theta)_{\text{norm}} \Big|_{4^\circ}^{90^\circ} \right) + \sum_k \text{AF}(\theta_k)_{\text{norm}}. \quad (9)$$

We can see that in this paper cost function is not same as that in paper [23]. The main reason why the form of the cost function (9) was taken, rather than form (10), is that the value of the second part of cost function tends towards negative infinity for $\text{AF}(\theta_k)_{\text{norm}} = 0$. This case would adversely affect the search in such a way that the search for the second part of (10) would be predominant. In this case, we took normalized

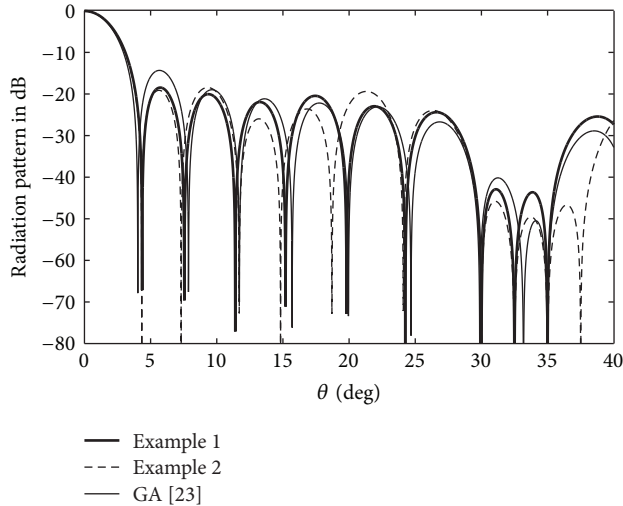


FIGURE 2: The normalized radiation pattern of 28-element linear array.

array factor and therefore it is unlikely that such a case could occur.

$$\text{Cost} = 20 \log \left\{ \max \left(\text{AF}(\theta)_{\text{norm}} \Big|_{4^{\circ}}^{90^{\circ}} \right) \right\} + 20 \log \left\{ \sum_k \text{AF}(\theta_k)_{\text{norm}} \right\}. \quad (10)$$

The radiation pattern has been shown in Figure 2. As it is seen from Figure 2 obtained results give lower side lobe level than results from paper [23]. Region $[30^{\circ}, 35^{\circ}]$ is under -40 dB and it is lower than obtained region from published work. The optimal locations with respect to λ obtained by using the provided algorithm are shown in Table 1. In Table 2 SLL, FNBW, and nulls depth at $\theta_1 = 30^{\circ}$, $\theta_2 = 32.5^{\circ}$, and $\theta_3 = 35^{\circ}$ are shown. Convergence characteristics in terms of side lobe level versus the number of iterations are shown in Figure 3. It is observed that the cost function value converges to the optimum result quickly.

The observed results were better for $R = 0.05$. From Table 2, it is seen that the results provide side lobe level lower than -18 dB, with nulls deeper than -100 dB. Minimum side lobe level of the array optimized using presented algorithm showed improvement (4 dB) over the published works GPS [23], ACO [18], and CSO [22] (Table 3). All three nulls are deeper than -100 dB and all nulls are deeper than nulls from published works. The FNBW is slightly higher than previously published works.

In the second experiment, we performed the synthesis of $2N = 20$ elements' antenna array with fixed excitation Dolph-Chebyshev amplitudes, which form the side lobe level at -30 dB. Excitation amplitudes have values = $[1, 0.97, 0.912, 0.831, 0.731, 0.620, 0.504, 0.391, 0.285, 0.325]$. Null is located at the position of $\theta_1 = 20^{\circ}$, whereas $\theta_{11} = 8^{\circ}$ and $\theta_{12} = 90^{\circ}$.

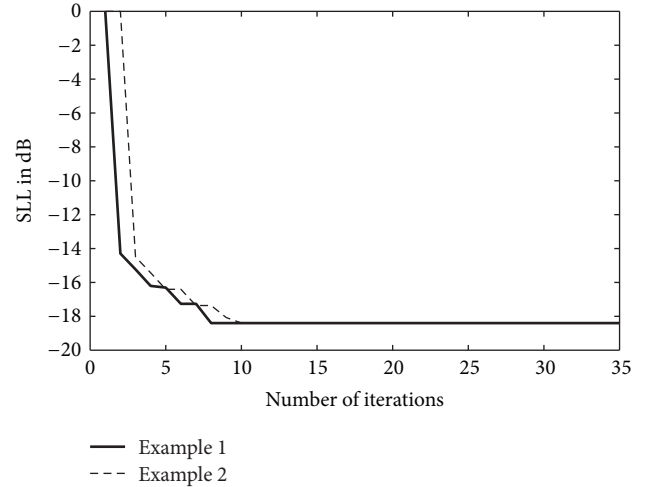


FIGURE 3: The convergence characteristics of side lobe level for optimization of a 28-element linear array.

TABLE 1: Element position of the 28-element linear array (normalized with respect to λ).

Element	Example 1 ($R = 0.05$)	Example 2 ($R = 0.1$)	GA [23]
± 1	0.1901	0.2081	0.252
± 2	0.6309	0.6048	0.752
± 3	1.0720	1.0688	1.251
± 4	1.5273	1.4997	1.754
± 5	2.0043	1.8792	2.257
± 6	2.4929	2.4284	2.756
± 7	2.9220	3.0077	3.284
± 8	3.5061	3.5671	3.792
± 9	3.9975	4.1606	4.291
± 10	4.4910	4.5425	4.790
± 11	5.2269	5.2225	5.463
± 12	5.9271	6.0085	5.965
± 13	6.4800	6.5472	6.465
± 14	7.1298	7.2607	7.094

TABLE 2: Comparative results for $2N = 28$ elements' linear array.

	SLL	FNBW	Null depth in dB		
			30°	32.5°	35°
Example 1 ($R = 0.05$)	-18.41	8.7	-163.19	-100.01	-186
Example 2 ($R = 0.1$)	-18.39	8.6	-171.77	-140.42	-164.82

For the objective function the following relations were taken:

$$\text{Cost} = \max \left(\text{AF}(\theta)_{\text{norm}} \Big|_{8^{\circ}}^{90^{\circ}} \right) + \text{AF}(20^{\circ})_{\text{norm}}. \quad (11)$$

Mutual coupling effects were under consideration during the processing. In this experiment, we fixed $R = 0.1$. The optimal locations with respect to λ obtained by using the provided algorithm are shown in Table 4 together with the results obtained in [23].

TABLE 3: Comparison with published results for $2N = 28$ elements optimized with respect to position.

	SLL	FNBW	Null depth in dB		
			30°	32.5°	35°
Example 1 ($R = 0.05$)	-18.41	8.7	-163.19	-100.01	-186
GPS [23]	-14.39	7.8	-71.89	-46.87	-74.13
ACO [18]	-14.88	8.4	-57.42	-59.20	-60.46
CSO [22]	-13.23	8.2	-75.00	-67.05	-65.32

TABLE 4: Element position of the 20 element linear array (normalized with respect to λ).

Element	Obtained results	GPS [23]	GA [23]
± 1	0.2387	0.25	0.264
± 2	0.7396	0.75	0.779
± 3	1.2454	1.25	1.283
± 4	1.7750	1.787	1.840
± 5	2.2821	2.338	2.382
± 6	2.7785	2.838	2.884
± 7	3.2473	3.338	3.389
± 8	3.7092	3.838	3.897
± 9	4.2077	4.338	4.419
± 10	4.8180	4.990	5.079

TABLE 5: Comparison with published results for $2N = 20$ elements optimized with respect to position.

	SLL	FNBW	Null depth in dB at 20°
Obtained results	-28.5025	16.8	-233.00
GPS [23]	-27.7376	16.9	-61.01
GA [23]	-26.6344	16.4	-80.06

Figure 4 shows a radiation pattern produced by the presented method together with radiation pattern obtained in the work [23]. We can notice that the resulting null is at the position of 20°. In Table 5 SLL, FNBW, and null depth at $\theta_1 = 20^\circ$ are shown. We can also notice that SLL obtained by presented method is -0.8 dB lower than the examined results obtained in [23]. Radiation pattern obtained with the presented method has a deeper null than the published work [23]. FNBW has a negligible difference.

5. Conclusion

In the presented work, we proposed a new algorithm for finding the optimal position of the 5G mm wave antenna array elements which minimize side lobe level and placing nulls in desired directions. In both experiments, suppression of SLL was achieved, while nulls were maintained in specified directions and cost function value of presented method converges to the optimum result quickly. Given algorithm provides better results than the compared methods and shows good potential for the 5G mm wave antenna array synthesis.

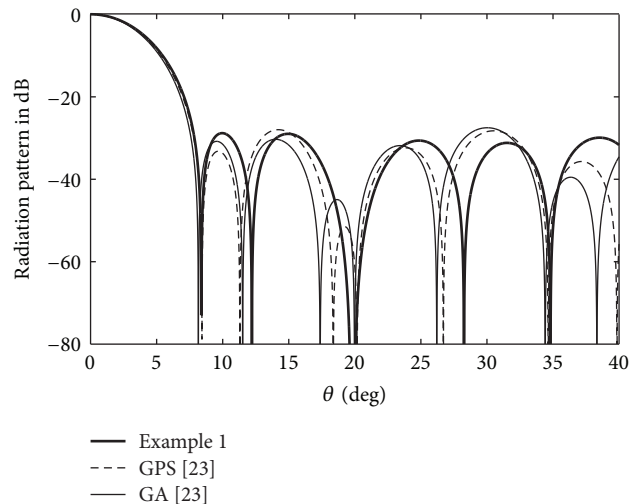


FIGURE 4: The normalized radiation pattern of 20-element linear array.

Conflicts of Interest

The authors declare that they have no conflicts of interest.

References

- [1] J. Zhang, X. Ge, Q. Li, M. Guizani, and Y. Zhang, "5G millimeter-wave antenna array: design and challenges," *IEEE Wireless Communications*, pp. 2–8, 2016.
- [2] L. Fa-Long and C. J. Zhang, *Signal Processing for 5G: Algorithms and Implementations*, John Wiley & Sons, 2016.
- [3] S. Rangan, T. S. Rappaport, and E. Erkip, "Millimeter-wave cellular wireless networks: potentials and challenges," *Proceedings of the IEEE*, vol. 102, no. 3, pp. 366–385, 2014.
- [4] M. Park and P. Gopalakrishnan, "Analysis on spatial reuse and interference in 60-GHz wireless networks," *IEEE Journal on Selected Areas in Communications*, vol. 27, no. 8, pp. 1443–1452, 2009.
- [5] S. A. Schelkunoff, "A mathematical theory of linear arrays," *The Bell System Technical Journal*, vol. 22, no. 1, pp. 80–107, 1943.
- [6] C. A. Balanis, *Antenna Theory: Analysis and Design*, John Wiley & Sons, San Francisco, Calif, USA, 3rd edition, 2005.
- [7] A. D. Bresler, "A new algorithm for calculating the current distributions of Dolph-Chebyshev arrays," *IEEE Transactions on Antennas and Propagation*, vol. 28, no. 6, pp. 951–952, 1980.
- [8] S. J. Orfanidis, *Electromagnetic Waves and Antennas*, Rutgers University, New Brunswick, NJ, USA, 2014.

- [9] R. S. Eliot, *Antenna Theory and Design*, Prentice Hall, Upper Saddle River, NJ, USA, 2003.
- [10] C. Ramesh and R. Mallikarjuna, "Antenna array synthesis for suppressed side lobe level using evolutionary algorithms," *International Journal of Engineering and Innovative Technology (IJEIT)*, vol. 2, pp. 235–239, 2012.
- [11] Y. Cengiz and H. Tokat, "Linear antenna array design with use of genetic, memetic and tabu search optimization algorithms," *Progress In Electromagnetics Research C*, vol. 1, pp. 63–72, 2008.
- [12] G. K. Mahanti, N. Pathak, and P. Mahanti, "Synthesis of thinned linear antenna arrays with fixed sidelobe level using real-coded genetic algorithm," *Progress in Electromagnetics Research*, vol. 75, pp. 319–328, 2007.
- [13] A. Monorchio, S. Genovesi, U. Serra, A. Brizzi, and G. Manara, "A technique to optimize nonuniformly spaced arrays with low sidelobe level by using a genetic algorithm," in *Proceedings of the IEEE Antennas and Propagation Society International Symposium*, vol. 2, pp. 275–278, Pisa, Italy, July 2005.
- [14] K. Güney and A. Akdağlı, "Null steering of linear antenna arrays using a modified tabu search algorithm," *Progress in Electromagnetics Research*, vol. 33, pp. 167–182, 2001.
- [15] M. M. Khodier and C. G. Christodoulou, "Linear array geometry synthesis with minimum sidelobe level and null control using particle swarm optimization," *IEEE Transactions on Antennas and Propagation*, vol. 53, no. 8, pp. 2674–2679, 2005.
- [16] M. Rattan, M. S. Patterh, and B. S. Sohi, "Design of a linear array of half wave parallel dipoles using particle swarm optimization," *Progress in Electromagnetics Research M*, vol. 2, pp. 131–139, 2008.
- [17] M. Khodier and M. Al-Aqeel, "Linear and circular array optimization: a study using particle swarm intelligence," *Progress In Electromagnetics Research B*, vol. 15, pp. 347–373, 2009.
- [18] E. Rajo-Iglesias and Ó. Quevedo-Teruel, "Linear array synthesis using an ant-colony-optimization-based algorithm," *IEEE Antennas and Propagation Magazine*, vol. 49, no. 2, pp. 70–79, 2007.
- [19] K. N. Abdul Rani, M. F. Abd Malek, and N. Siew-Chin, "Nature-inspired cuckoo search algorithm for side lobe suppression in a symmetric linear antenna array," *Radioengineering*, vol. 21, no. 3, pp. 865–874, 2012.
- [20] H. Ahmed and H. Abdelhafid, "Cuckoo search optimization for linear antenna arrays synthesis," *Serbian Journal of Electrical Engineering*, vol. 10, no. 3, pp. 371–380, 2013.
- [21] Z. Rosic, "Antenna array synthesis for suppressed side lobe level using combination of global and local search," *International Journal of Engineering and Innovative Technology (IJEIT)*, vol. 4, no. 6, pp. 58–61, 2014.
- [22] L. Pappula and D. Ghosh, "Linear antenna array synthesis using cat swarm optimization," *AEU—International Journal of Electronics and Communications*, vol. 68, no. 6, pp. 540–549, 2014.
- [23] F. Tokan and F. Gunes, "Mutual coupling compensation in non-uniform antenna arrays using inter-element spacing restrictions," *Applied Computational Electromagnetics Society Journal*, vol. 26, no. 7, pp. 596–602, 2011.
- [24] W. Kummer, "Basic array theory," *Proceedings of the IEEE*, vol. 80, no. 1, pp. 127–140, 1992.
- [25] W. L. Stutzman and G. A. Thiele, *Antenna Theory and Design*, John Wiley & Sons, New York, NY, USA, 3rd edition, 2012.
- [26] M. T. Ma, *Theory and Application of Antenna Arrays*, John Wiley & Sons, 1974.

Research Article

Outage Analysis of Multihop Wireless Backhaul Using Millimeter Wave under Blockage Effects

Haejoon Jung¹ and In-Ho Lee²

¹Department of Information and Telecommunication Engineering, Incheon National University, Incheon 22012, Republic of Korea

²Department of Electrical, Electronic and Control Engineering, Hankyong National University, Anseong 17579, Republic of Korea

Correspondence should be addressed to In-Ho Lee; ihlee@hknu.ac.kr

Received 20 November 2016; Revised 30 January 2017; Accepted 5 February 2017; Published 21 February 2017

Academic Editor: Mihajlo Stefanovic

Copyright © 2017 Haejoon Jung and In-Ho Lee. This is an open access article distributed under the Creative Commons Attribution License, which permits unrestricted use, distribution, and reproduction in any medium, provided the original work is properly cited.

We consider multihop millimeter-wave (mm-Wave) wireless backhaul communications, by which small cell base station (SBS) clusters can connect to a macrocell base station (MBS). Assuming the mm-Wave wireless backhaul links suffer from outage caused by obstacles that block the line-of-sight (LoS) paths, we derive the statistics of a perhop distance based on the blockage model using stochastic geometry and random shape theory and analyze the multihop outage probability using the statistics of a perhop distance. We also provide an optimal number of hops to minimize the end-to-end outage performance between the MBS and the destination SBS cluster when the end-to-end distance is given.

1. Introduction

Dense deployment of small cells over traditional macrocell is considered as a key enabling technique for the emerging fifth-generation (5G) cellular networks [1–4]. For the small cell network deployment, millimeter-wave (mm-Wave) wireless backhaul is a cost-effective and scalable solution with large contiguous bandwidths. Moreover, the line-of-sight (LoS) nature of mm-Wave communication with directional antenna arrays can help to control the signal interference [5].

However, mm-Wave signals are more sensitive to blockage effects than signals in lower frequency bands, as indicated by the measurement data in [6–8]. Thus, the performances of the mm-Wave cellular systems are vastly affected by blockage effects [9]. There are two widely used approaches to incorporate the impact of blockages into signal propagation: ray tracing and stochastic modeling. In the ray tracing approach, blockages are characterized explicitly by their sizes, locations, and shapes. Therefore, this method is appropriate for environment-specific simulations based on electromagnetic simulation tools, which perform complex numerical calculations for ray tracing [10, 11]. On the other

hand, in the stochastic models, the statistics of blockages are characterized with smaller number of parameters compared to ray tracing. Therefore, the stochastic models are used to analyze general networks with acceptable accuracy.

In [12], the authors propose mm-Wave channel model incorporating the blockage effects based on stochastic geometry and random shape theory. Stochastic geometry has been a powerful technique to evaluate system performance in the conventional cellular networks [13], which reveals the impacts of multiple system parameters such as base station density, transmit power, and path-loss exponent. The key idea in [12] is to model random obstacles (e.g., buildings) as rectangles with random sizes and orientations whose centers form a Poisson point process (PPP) on 2-dimensional space. The model proposed in [12] can capture distance-dependent characteristics of the blockage effects, which is more realistic compared to the conventional shadowing model using log-normal distribution.

Using this mm-Wave propagation model in [10], the authors in [14] present a framework to derive signal-to-interference-plus-noise ratio (SINR) distributions, which can be used to analyze coverage and rate performances. Also, the

outage probability of a macrodiversity system with multiple base stations (BSs) that are connected by wire to each other is analyzed in [15], where an outage occurs when there is no LoS path from all the base stations to the user. The analysis in [15] presents that this macrodiversity coming from the unblocked BS selection can be exploited to mitigate blockage in mm-Wave cellular systems.

In [16], the outage performance of mm-Wave wireless backhaul links between a macrocell base station (MBS) and small cell base stations (SBSs) is also studied using the channel model in [10]. Specifically, in [16], the multiple SBSs in a cluster have wired connections to each other, and the wireless backhaul link between the MBS and the SBS cluster is assumed to be reliable as long as there exists one or more SBSs that have blockage-free LoS paths from the MBS. In other words, the MBS can selectively choose an unblocked SBS to construct a wireless backhaul link by beam steering, which is equivalent to the macrodiversity in [15].

However, while [16] only considers the one-hop communication between the MBS and a single SBS cluster, the 5G cellular networks may have multiple SBS clusters, which require multihop transmissions to improve the cell coverage [1, 2]. Considering the distance dependence of the blockage effects (i.e., the likelihood of a blockage event increases as the distance increases) at mm-Wave, multihop communication can be an effective solution to build mm-Wave wireless backhaul systems. In this context, motivated by the limitation in [16], we extend the single-hop wireless backhaul system in [16] to a multihop scenario with multiple SBS clusters. Moreover, it is noteworthy that the wireless backhaul links between two SBS clusters studied in this paper are distinct from the system model in [16] because we consider multiple-points-to-multiple-points (SBSs-to-SBSs) links, while [16] is focused on single-point-to-multiple-points (MBS-to-SBSs) links. Therefore, with different distance statistics from [16], the intercluster SBS-to-SBS communication can benefit from higher order of spatial diversity compared with the MBS-to-SBS communication in [16].

The contributions of this paper are fourfold. First, we derive the probability distribution, mean, and variance of a perhop distance (i.e., the distance between two randomly located SBSs in two adjacent SBS clusters), considering the spatial diversity. Second, we analyze the perhop outage performance of mm-Wave wireless backhaul links between two adjacent SBS clusters. Third, the outage analysis is extended from the perhop link to multihop systems. Lastly, we present an optimal and suboptimal hop count to minimize the end-to-end outage performance between the MBS and the destination SBS cluster for a given end-to-end distance, where the suboptimal hop count is derived based on only the perhop outage performance.

This paper is organized as follows. We introduce the system model in Section 2. We derive the probability distribution, mean, and variance of the distance between two SBS clusters in Section 3. The outage performances of perhop and multihop cases are analyzed in Section 4. In Section 5, we show optimal hop distance and hop count to minimize the outage performance and propose suboptimal hop distance and hop count that give close enough outage probabilities

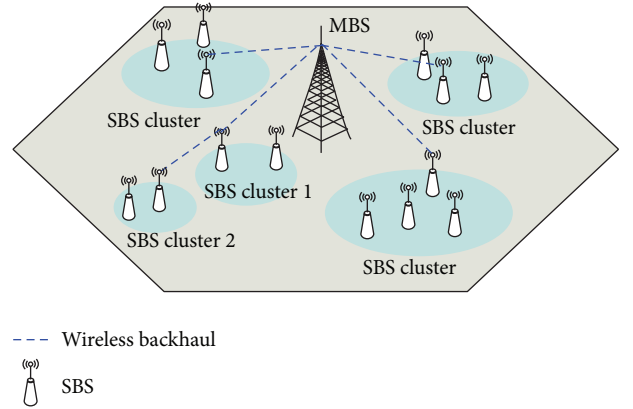


FIGURE 1: Illustration of a 5G-network with mm-Wave wireless backhaul.

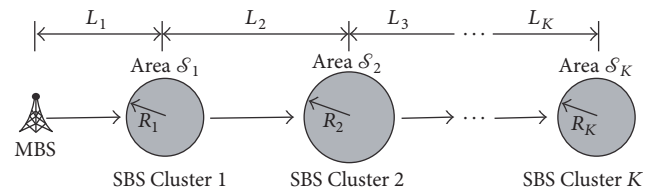


FIGURE 2: Multihop wireless backhaul.

to the optimal ones. Finally, conclusions are provided in Section 6.

2. System Model

We consider a 5G network with a single MBS and multiple SBS clusters as an example illustration in Figure 1. In the figure, the macrocell is indicated by the gray hexagon, and the SBS clusters are represented by the sky blue circles. Each SBS cluster has multiple SBSs, which are connected to each other through wires to enable spatial diversity in SBS cluster [15, 16]. The MBS is connected to the core network, and SBSs can access the core network via the MBS using wireless backhaul, which is indicated by the dotted blue lines in the figure. Moreover, some SBS clusters, which are far from the MBS, trigger multihop transmissions for the backhaul links to overcome path loss and blockage effects. For example, in Figure 1, SBS Cluster 2 communicates with the MBS in two hops over Cluster 1.

As shown In Figure 2 focusing on the multihop wireless backhaul links, we assume that SBSs in each cluster are distributed over a circle. In the figure, the areas of the multihop clusters are denoted by Areas $\mathcal{S}_1, \mathcal{S}_2, \dots,$ and \mathcal{S}_K with radii of R_1, R_2, \dots, R_K , respectively. Also, the hop distances are denoted by L_k , where $k \in \{1, 2, \dots, K\}$. As in [16], we assume that in k -th cluster multiple SBSs are uniformly distributed with intensity λ_k according to a homogeneous point process (PPP) [17], which is a widely used model for various types of

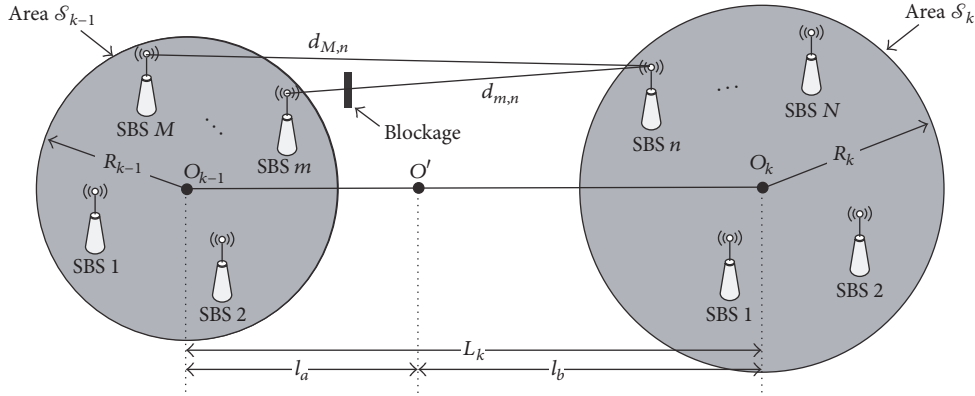


FIGURE 3: Intercluster mm-Wave wireless backhaul links.

cellular networks [18]. For the end-to-end wireless backhaul link with hops, the outage probability can be expressed as

$$P_{\text{out}} = 1 - \prod_{k=1}^K (1 - P_{\text{out};k}), \quad (1)$$

where $P_{\text{out};k}$ is the outage probability of k -th hop [19]. Assuming the outage events in different hops are mutually independent, the outage analysis over multiple hops can be decoupled into multiple intercluster links, while the first-hop outage $P_{\text{out};1}$ can be obtained based on the analysis in [16]. When we consider the multihop performance P_{out} , we assume uniform SBS clusters and equidistant hops for the mathematical tractability which we will explain in detail in Section 4.2. In general, however, the densities of the SBS clusters are dissimilar, which means variable $P_{\text{out};k}$ and hop distances for different k . Even in this case, the perhop analysis in this paper still can be used to optimize the end-to-end outage P_{out} , which is a function of the hop distances and the corresponding end-to-end hop count K .

To analyze the outage performances of the following hops, we consider the intercluster outage $P_{\text{out};k}$ for $k \geq 2$ as shown in Figure 3. Clusters $k-1$ and k have M and N SBSs, which are uniformly distributed over \mathcal{S}_{k-1} and \mathcal{S}_{k-2} with intensities λ_{k-1} and λ_k , respectively. These intensities correspond to the average numbers of SBSs per unit area (i.e., SBSs/m²). In other words, the numbers of the SBSs in the two clusters are assumed to be M and N , which are independent random variables following Poisson probability distributions as

$$\begin{aligned} \Pr[M = m] &= \frac{(\lambda_{k-1} \pi R_{k-1}^2)^m}{m!} e^{-\lambda_{k-1} \pi R_{k-1}^2}, \\ \Pr[N = n] &= \frac{(\lambda_k \pi R_k^2)^n}{n!} e^{-\lambda_k \pi R_k^2}, \end{aligned} \quad (2)$$

where $\Pr[X = x]$ denotes the probability that $X = x$ and x is a nonnegative integer. Therefore, the average numbers of the SBSs in the two clusters are given by $\mathbb{E}\{M\} = \lambda_{k-1} \pi R_{k-1}^2$ and $\mathbb{E}\{N\} = \lambda_k \pi R_k^2$, where $\mathbb{E}\{\cdot\}$ implies the expectation operator. We assume the centers of the two clusters are separated by L_k

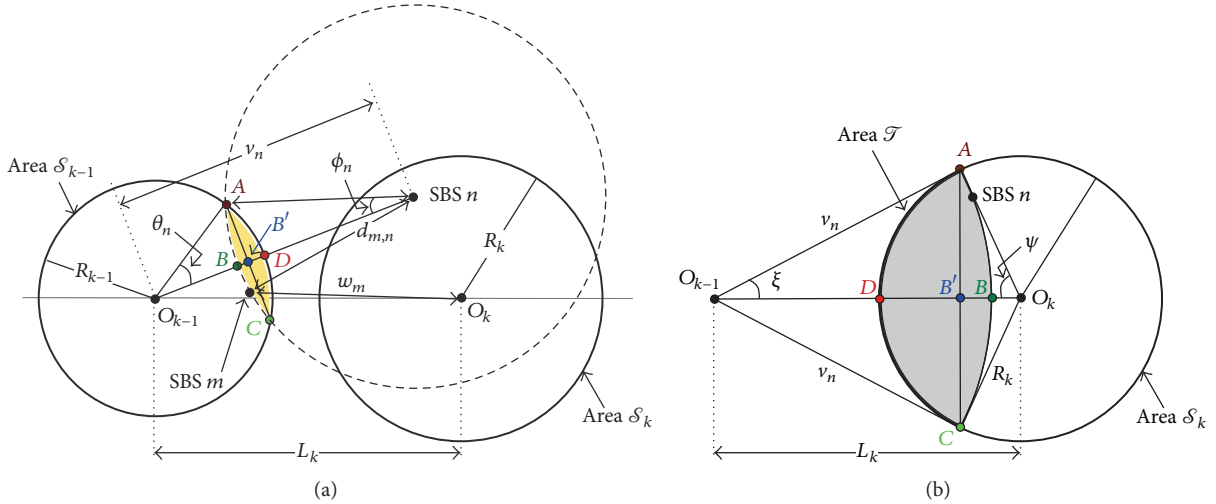
with fixed ratios to the two radii as $L_k = a_k R_{k-1} = b_k R_k$, where $a_k > 2$ and $b_k > 2$ (i.e., there is no intersection between \mathcal{S}_{k-1} and \mathcal{S}_k) (we assume the dense deployment of SBSs with wired connections in each cluster for coverage extension, especially to solve the *hotspots* problem, and the geographically disjoint SBS clusters. In addition, considering the construction cost, we assume that the SBSs in different clusters communicate with each other through the multihop wireless backhaul.)

Let $d_{m,n}$ be the distance between the mm-Wave SBSs m and n in \mathcal{S}_{k-1} and \mathcal{S}_k , respectively, as shown in the figure. Also, as in [12, 14–16], the probability of no blockage in an individual SBS-to-SBS (S2S) path is $P_{\text{LoS}(m,n)} = e^{-\beta d_{m,n}}$, where β is the parameter that captures density and size of obstacles. The greater β means obstacles with higher density and larger sizes, which results in lower $P_{\text{LoS}(m,n)}$. In this paper, we assume $P_{\text{LoS}(m,n)}$ can be interpreted as the probability that the communication link between the SBSs m and n in the two clusters is reliable.

As in [16], we assume that the multiple SBSs in the same cluster are connected to each other through wires and thus the wireless backhaul link between the two clusters is reliable if one (or more) of the individual S2S links between the two clusters is reliable. An outage event of the intercluster mm-Wave wireless backhaul link is caused by blockage of LoS path. Before data transmission, with beam steering, each SBS in Cluster $k-1$ can selectively connect to one of the SBSs in Cluster k whose LoS path is blockage-free. Also, once one SBS finds an unobstructed LoS path, the SBS notifies the other SBSs in the same cluster via the wired intracluster connections.

3. Probability Distribution of S2S Distance $d_{m,n}$ between Two SBS Clusters

In order to investigate the performance of the mm-Wave wireless backhaul system, we need to consider probability distribution of the S2S distance $d_{m,n}$ between the two SBS clusters, since $P_{\text{LoS}(m,n)}$ is a function of $d_{m,n}$, which is a random variable. As shown in Figure 4(a), suppose the distance between the center of the left SBS cluster O_{k-1} and SBS n in the right SBS cluster is v_n . To derive the probability distribution of

FIGURE 4: An example illustration to derive the PDF of $d_{m,n}$.

$d_{m,n}$, we first find the probability distribution function (PDF) of v_n using an example illustration in Figure 4 (because v_n is the distance between a random location in Area \mathcal{S}_k and the fixed point O_{k-1} , the PDF of v_n is identical to the PDF of the distance of the single-hop wireless backhaul in [16].), and then conditioned on v_n we will obtain the PDF of $d_{m,n}$. In Figure 4(b), the shaded area (Area \mathcal{T}) is the feasible region of v_n in the circle (Area \mathcal{S}_k). Consequently, the cumulative density function (CDF) of v_n is expressed as the ratio between Areas \mathcal{T} and \mathcal{S}_k as

$$F_{v_n}(x) = \Pr[v_n \leq x] = \frac{\psi R_k^2 + \xi x^2 - R_k L_k \sin \psi}{\pi R_k^2}, \quad (3)$$

Where $L_k - R_k \leq x \leq L_k + R_k$, $\psi = \arccos((R_k^2 + L_k^2 - x^2)/2R_k L_k)$, and $\xi = \arccos((x^2 + L_k^2 - R_k^2)/2x L_k)$. As a result, the PDF of v_n is

$$f_{v_n}(x) = \frac{x}{\pi R_k^2} \left(\frac{R_k/L_k}{\sqrt{1 - (L_k^2 - x^2 + R_k^2)^2 / 4L_k^2 R_k^2}} - \frac{(x/L_k - (L_k^2 + x^2 - R_k^2)/2L_k x)}{\sqrt{1 - (L_k^2 + x^2 - R_k^2)^2 / 4L_k^2 x^2}} - \frac{(L_k^2 - x^2 + R_k^2)/2L_k R_k}{\sqrt{1 - (L_k^2 - x^2 + R_k^2)^2 / 4L_k^2 R_k^2}} + 2 \arccos\left(\frac{L_k^2 + x^2 - L_k^2}{2L_k x}\right) \right), \quad (4)$$

where $L_k - R_k \leq x \leq L_k + R_k$. As shown in [16], when $L_k > 2R_k$, we can derive an approximate PDF by treating the area

enclosed by the path \overline{ABCD} as the region bounded by the path $\overline{AB'CDA}$ in Figure 4(b):

$$f_{v_n}^*(x) = \frac{2\sqrt{R_k^2 - (L_k - x)^2}}{\pi R_k^2}, \quad (5)$$

where $L_k - R_k \leq x \leq L_k + R_k$. With this approximated PDF, we can obtain $\mathbb{E}\{v_n\} = L_k$ and $\mathbb{V}\{v_n\} = R_k^2/4$.

Then, going back to Figure 4(a), conditioned on v_n , the PDF of $d_{m,n}$ can be derived as the ratio of the area within a closed path \overline{ABCD} to the entire circle \mathcal{S}_{k-1} , which is given by

$$F_{d_{m,n}|v_n}(x | v_n) = \frac{\theta_n R_{k-1}^2 + \phi_n x^2 - R_{k-1} v_n \sin \theta_n}{\pi R_{k-1}^2}, \quad (6)$$

where $v_n - R_{k-1} \leq x \leq v_n + R_{k-1}$, $\theta_n = \arccos((R_{k-1}^2 + L_k^2 - x^2)/2R_{k-1} v_n)$, and $\phi_n = \arccos((x^2 + v_n^2 - R_{k-1}^2)/2x v_n)$. Hence, the corresponding conditional PDF of $d_{m,n}$ is given by

$$f_{d_{m,n}|v_n}(x | v_n) = \frac{dF_{d_{m,n}|v_n}(x | v_n)}{dx} = \frac{x}{\pi R_{k-1}^2} \left(\frac{R_{k-1}/v_n - (v_n^2 - x^2 + R_{k-1}^2)/2v_n R_{k-1}}{\sqrt{1 - (v_n^2 - x^2 + R_{k-1}^2)^2 / 4v_n^2 R_{k-1}^2}} - \frac{x/v_n - (v_n^2 + x^2 - R_{k-1}^2)/2v_n x}{\sqrt{1 - (v_n^2 + x^2 - R_{k-1}^2)^2 / 4v_n^2 x^2}} + 2 \arccos\left(\frac{v_n^2 + x^2 - R_{k-1}^2}{2v_n x}\right) \right). \quad (7)$$

As the PDF of v_n , for a large enough L_k relative to R_k and R_{k-1} , this conditional PDF has an approximate form

$$f_{d_{m,n}|v_n}^*(x | v_n) = \frac{2\sqrt{R_{k-1}^2 - (v_n - x)^2}}{\pi R_{k-1}^2}, \quad (8)$$

where $v_n - R_{k-1} \leq x \leq v_n + R_{k-1}$. Hence, the PDF of $d_{m,n}$ is given by

$$\begin{aligned} f_{d_{m,n}}^*(x) &= \int_{L-R_k}^{L+R_k} f_{d_{m,n}|v_n}^*(x | v_n = y) f_{v_n}^*(y) dy \\ &= \int_{L-R_k}^{L+R_k} \frac{2\sqrt{R_{k-1}^2 - (y-x)^2}}{\pi R_{k-1}^2} \frac{2\sqrt{R_k^2 - (L-y)^2}}{\pi R_k^2} dy, \end{aligned} \quad (9)$$

where $L_k - R_{k-1} - R_k \leq x \leq L_k + R_{k-1} + R_k$. This approximate PDF $f_{d_{m,n}}^*(x)$ gives the mean and variance as follows:

$$\begin{aligned} \mathbb{E}\{d_{m,n}\} &= \mathbb{E}\{\mathbb{E}\{d_{m,n} | v_n\}\} = \mathbb{E}\{v_n\} = L_k, \\ \text{VAR}\{d_{m,n}\} &= \mathbb{E}\{\text{VAR}\{d_{m,n} | v_n\}\} \\ &\quad + \text{VAR}\{\mathbb{E}\{d_{m,n} | v_n\}\} \\ &= \frac{R_{k-1}^2}{4} + \text{VAR}\{v_n\} = \frac{R_{k-1}^2 + R_k^2}{4}. \end{aligned} \quad (10)$$

These two statistics will be used to derive the perhop outage probability in the next section.

4. Outage Analysis

4.1. Intercluster Outage Analysis. In this section, we derive the probability that there is no reliable S2S LoS link between the two SBS clusters \mathcal{S}_{k-1} and \mathcal{S}_k . We define an outage, if all the LoS S2S paths are blocked by obstacles. Let $U_{m,n}$ be a Bernoulli random variable as

$$U_{m,n} = \begin{cases} 1, & \text{w.p. } P_{\text{LoS}(m,n)} = e^{-\beta d_{m,n}}, \\ 0, & \text{w.p. } 1 - P_{\text{LoS}(m,n)} = 1 - e^{-\beta d_{m,n}}, \end{cases} \quad (11)$$

where if $U_{m,n} = 1$, it means that the mm-Wave link between SBS m in \mathcal{S}_{k-1} and SBS n in \mathcal{S}_k is reliable. Assuming that blockage is impenetrable, as in [12, 14–16], an outage event of the mm-Wave SBS occurs, if all $U_{m,n}$'s are zeros. In other words, if there is at least one LoS mm-Wave link with $U_{m,n} = 1$ for any pair m and n , the mm-Wave communication between the two SBS clusters is reliable. Therefore, the outage in k th hop can be defined as

$$\begin{aligned} P_{\text{out:k}} &= \sum_{m=1}^{\infty} \sum_{n=1}^{\infty} \Pr[U_{i,j}'\text{s are all zeros} | M = m, N = n] \\ &\quad \cdot \Pr[M = m, N = n] + \Pr[M = 0] \\ &\quad + \Pr[N = 0], \end{aligned} \quad (12)$$

where $1 \leq i \leq m$ and $1 \leq j \leq n$.

Following [12, 14–16], for analytical tractability, we assume the outage events indicated by $U_{i,j}$'s in (12) are mutually *independent* for all i and j . Strictly speaking, the blockage events on different links are not always independent. Therefore, as in [15, 16], the outage probability in this paper may be a lower bound as a reference of system design and analysis. However, we note that the numerical results in [12] show that the error caused by the *independent link assumption* is minor and acceptable in accuracy. With the assumption of the independent blockage events, we have

$$\begin{aligned} \Pr[U_{i,j}'\text{s are all zeros} | M = m, N = n] \\ = \prod_{j=1}^n \prod_{i=1}^m \mathbb{E}[1 - e^{-\beta d_{ij}}] = (E[1 - e^{-\beta d_{ij}}])^{mn}, \end{aligned} \quad (13)$$

where the distance d_{ij} between SBSs i and j from \mathcal{S}_{k-1} and \mathcal{S}_k is a random variable with the approximate PDF in (9). Letting $A = \mathbb{E}[1 - e^{-\beta d_{ij}}]$, it can be approximated by Taylor expansion as

$$\begin{aligned} A &\approx 1 - \int_{L-R_{k-1}-R_k}^{L+R_{k-1}+R_k} e^{-\beta x} f_{d_{ij}}^*(x) dx \\ &\approx 1 - \left(e^{-\beta \mathbb{E}\{d_{i,j}\}} + \frac{\beta^2}{2} e^{-\beta \mathbb{E}\{d_{i,j}\}} \text{VAR}\{d_{i,j}\} \right) \\ &\approx 1 - \left(1 + \frac{\beta^2 (R_{k-1}^2 + R_k^2)}{8} \right) e^{-\beta L_k}, \end{aligned} \quad (14)$$

where $L = a_k R_{k-1} = b_k R_k$. Thus, the outage probability in (12) is given by

$$P_{\text{out:k}} = \sum_{m=0}^{\infty} \sum_{n=0}^{\infty} A^{mn} \Pr[N = n] \Pr[M = m]. \quad (15)$$

Thus, we can interpret A in (14) as the expected $P_{\text{out:k}}$, when the number of SBSs in the two clusters is given ($N = n$ and $M = m$). Unfortunately, it is difficult to obtain a closed form expression of (15), but based on (14) and (15), we can observe some important properties of the intercluster outage probability $P_{\text{out:k}}$ as follows.

Property 1. For given positive β , λ_{k-1} , λ_k , a_k , and b_k , $P_{\text{out:k}} \rightarrow 1$ as $L_k \rightarrow 0$ (because $R_{k-1} = L_k/a_k \rightarrow 0$ and $R_k = L_k/b_k \rightarrow 0$) (as described in Section 2, we assume the two SBS clusters are disjoint by $L_k = a_k R_{k-1} = b_k R_k$ with $a_k > 2$ and $b_k > 2$). Thus, when $L_k \rightarrow 0$, the sizes of the two clusters also become zero, which triggers an outage since the clusters do not have any SBSs.). Moreover, as $L_k \rightarrow \infty$, $P_{\text{out:k}} \rightarrow 1$. This property can be proved by $A \rightarrow 1$, as $L_k \rightarrow 0$ or ∞ .

Property 2. For fixed β , λ_{k-1} , λ_k , R_{k-1} , and R_k , as L_k increases (i.e., a_k and b_k increase), $P_{\text{out:k}}$ increases, because A increases.

Property 3. When the other parameters are fixed, the greater β gives the higher $P_{\text{out:k}}$.

Property 4. As λ_{k-1} and λ_k increase, $P_{\text{out:k}}$ decreases because the expected numbers of the SBSs M and N increase.

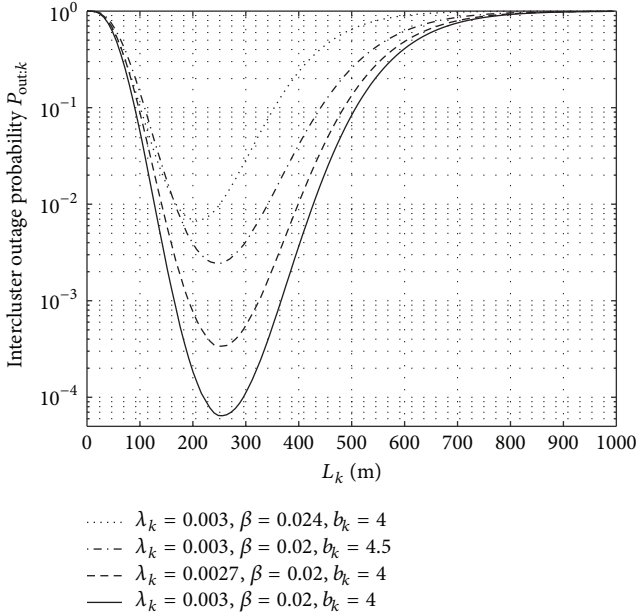


FIGURE 5: Intercluster outage probability $P_{\text{out}:k}$ versus L_k .

Figure 5 displays simulation results of the intercluster outage, where the horizontal axis indicates the hop distance L_k , while the vertical axis represents the intercluster outage probability $P_{\text{out}:k}$. Assuming $R_k = R_{k-1}$, $\lambda_k = \lambda_{k-1}$, and $a_k = b_k$, the solid line is the baseline, while the other three graphs correspond to changes in β , λ_k , and b_k , respectively. We can observe all the four properties in Figure 5. To be specific, all the four graphs in the figure are convex functions of L , which corresponds to Property 1. Also, as described in Property 2, compared to the solid line (i.e., the baseline case), the dash-dot graph, which indicates the higher $a_k = b_k$, shows the higher outage rates. Property 3 can be observed by the comparison between the solid and the dotted curves. Lastly, Property 4 is found by the dashed line in the figure.

4.2. Multihop Outage Analysis with a Constant Hop Distance. In this section, we extend the outage analysis to the multihop wireless backhaul assuming the uniform SBS clusters (i.e., $L_k = L$, $R_k = R$, and $\lambda_k = \lambda$ for all k). With this assumption, the end-to-end outage probability in (1) between the MBS and the K -th SBS cluster is simplified as

$$P_{\text{out}} = 1 - (1 - P_{\text{out}:1})(1 - P_{\text{out}:k})^{K-1}, \quad (16)$$

where $P_{\text{out}:1}$ is the outage probability for the first-hop link between the MBS and the first SBS cluster \mathcal{S}_1 presented in [16] and $P_{\text{out}:k}$ is given in (15). Because the height of the MBS is typically much greater than that of SBS, based on [12], we need to use a smaller blockage parameter $\beta' = c\beta$ for the first hop, where $c < 1$. Thus, $P_{\text{out}:1} < P_{\text{out}:k}$. When the end-to-end distance between the MBS to the center of the K -th SBS cluster O_K is D , then the hop distance is $L = D/K$.

Figure 6 shows multihop simulation results with $c = 1/4$, where the x - and y -axes are the number of hops K and the

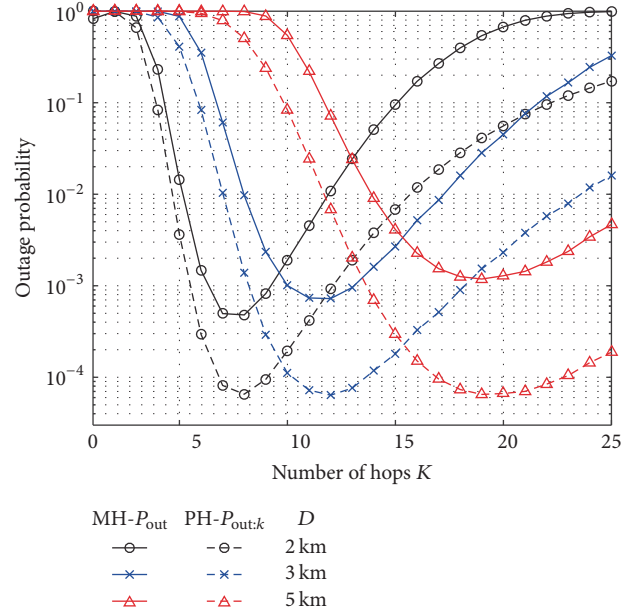


FIGURE 6: P_{out} versus K ($\beta = 0.02$, $\beta' = \beta/4$, $\lambda = 0.003$, and $b_k = 4$).

outage probability, respectively. The three different curves with the different markers (circle, x -marker, and triangle) represent the outage probability results for $D = 2, 3$, and 5 km, respectively. Also, the solid and dotted lines indicate the outage probabilities for the multihop (MH) and the perhop (PH) cases in (16) and (15), respectively. First, we can observe there exists an optimal hop count, denoted as K_{opt} , minimizes the outage probability for a given D . By the exhaustive search, we obtain $K_{\text{opt}} = 8, 12$, and 19, for $D = 2, 3$, and 5 km, which means that the corresponding optimal hop distances $L_{\text{opt}} = D/K_{\text{opt}}$ are almost the same for the three values of D . Also, the outage curves for both the MH and PH have the same K_{opt} because of (i) almost negligible first-hop error (because $\beta' = \beta/4$) and (ii) the same convex curves of $P_{\text{out}:k}$ for $k \geq 2$ as in Figure 6. Based on these observations, in the next section we propose the suboptimal hop count \widehat{K}_{opt} by mathematically deriving the suboptimal hop distance \widehat{L}_{opt} , instead of the exhaustive search of K .

5. Suboptimal Hop Count \widehat{K}_{opt}

As shown in Figure 5, there is an optimal hop distance L_k between two SBS clusters to minimize $P_{\text{out}:k}$. Assuming a_k and b_k are fixed, we derive the suboptimal L_k by treating the intercluster S2S path as two-hop link between the two SBS clusters. For example, in Figure 3, suppose that we place an imaginary relay at O' on the straight line connecting O_{k-1} and O_k , assuming that the two clusters communicate with each other only through the relay. Suppose that the outage rates “from the left cluster to the relay” and “from the relay to the right cluster” are $P'_{\text{out}:a}$ and $P'_{\text{out}:b}$ with the distances l_a and l_b , respectively. Then, as finding the center of mass, the best location of the relay O' corresponds to $P'_{\text{out}:a} = P'_{\text{out}:b}$.

Using the outage probability between SBS clusters to the MBS in [16], $P'_{\text{out}:a}$ and $P'_{\text{out}:b}$ are expressed as

$$P'_{\text{out}:a} = \exp\left(-\lambda_{k-1}\pi R_{k-1}^2 \left(1 + \frac{\beta^2 R_{k-1}^2}{8}\right) e^{-\beta l_a}\right),$$

$$P'_{\text{out}:b} = \exp\left(-\lambda_k\pi R_k^2 \left(1 + \frac{\beta^2 R_k^2}{8}\right) e^{-\beta l_b}\right). \quad (17)$$

Therefore, when $P'_{\text{out}:a} = P'_{\text{out}:b}$, l_a and l_b are, respectively, obtained as

$$l_a = \frac{L_k}{2} + \frac{1}{2\beta} \ln \left[\frac{\lambda_{k-1} R_{k-1}^2 (1 + \beta R_{k-1}^2)}{\lambda_k R_k^2 (1 + \beta R_k^2)} \right], \quad (18)$$

$$l_b = \frac{L_k}{2} + \frac{1}{2\beta} \ln \left[\frac{\lambda_k R_k^2 (1 + \beta R_k^2)}{\lambda_{k-1} R_{k-1}^2 (1 + \beta R_{k-1}^2)} \right], \quad (19)$$

$$\hat{L}_{\text{opt}} = \frac{-6\sqrt[3]{4b_k^2} + 8\sqrt[3]{9b_k^2 + 3\sqrt{6b_k^4 - 39b_k^2 + 192b_k + 32}} + 2\sqrt[3]{2} \left(9b_k^2 + 3\sqrt{6b_k^4 - 39b_k^2 + 192b_k + 32}\right)^{2/3} + 16\sqrt[3]{4}}{3\beta\sqrt[3]{9b_k^2 + 3\sqrt{6b_k^4 - 39b_k^2 + 192b_k + 32}}}, \quad (20)$$

where $R_{k-1} = L_k/a_k$ and $R_k = L_k/b_k$. If plugging l_a and l_b back into (17), the overall outage rate of the two-hop link with the imaginary relay is $P'_{\text{out}:k} = 1 - (1 - P'_{\text{out}:a})(1 - P'_{\text{out}:b})$. The proposed suboptimal hop distance \hat{L}_{opt} is L_k that minimizes $P'_{\text{out}:k}$. In other words, \hat{L}_{opt} corresponds to the solution of $\partial P'_{\text{out}:k}/\partial L_k = 0$, while $\partial^2 P'_{\text{out}:k}/\partial L_k^2 > 0$. This suboptimal \hat{L}_{opt} can be readily obtained by numerical calculation for given a_k , b_k , and β . If we assume the same SBS cluster sizes $R_k = R_{k-1}$ (i.e., $a_k = b_k$), we can obtain the suboptimal \hat{L}_{opt} in (20). Therefore, if the hop distances are the same with the uniform PPP intensities (i.e., $\lambda_k = \lambda$ for all k), the suboptimal hop count to reach the distance D is $\hat{K}_{\text{opt}} = \|D/\hat{L}_{\text{opt}}\|$, where $\|x\|$ means the nearest integer to x .

Figures 7(a) and 7(b) show the simulation results of L_{opt} and K_{opt} , respectively. In Figure 7(a), the horizontal axis is the blockage factor β , while the vertical axis is the optimal and suboptimal hop distances L_{opt} and \hat{L}_{opt} . As shown in the figure, both L_{opt} and \hat{L}_{opt} , which are indicated by the solid and dotted lines, decrease, as β increases, because of the greater blockage effects. Also, comparing the two graphs, $\hat{L}_{\text{opt}} < L_{\text{opt}}$ with the small gap in the entire range of β , which validates the proposed suboptimal hop distance. In Figure 7(b), the x -axis represents the distance D from the MBS to the K -th SBS cluster (i.e., the destination SBS cluster), while the y -axis indicates the optimal and suboptimal hop counts K_{opt} and \hat{K}_{opt} , which are denoted by the solid and dotted curves. In the figure, we can observe that K_{opt} and \hat{K} are almost linearly increasing, as D increases. Also, with the small difference, we observe that $\hat{K}_{\text{opt}} > K_{\text{opt}}$ because $\hat{L}_{\text{opt}} < L_{\text{opt}}$. Thus, based on $\hat{K}_{\text{opt}} = K_{\text{opt}} + \epsilon$ with a small ϵ , the suboptimal \hat{K}_{opt} can be used to reduce the exhaustive search range of \hat{K}_{opt} .

Figure 8 shows the end-to-end outage probabilities versus β , where the solid and dotted lines correspond to the outage probabilities with K_{opt} and \hat{K}_{opt} , respectively. The markers

represent different λ and D . As shown in the figure, the gap between the outage probabilities with K_{opt} and \hat{K}_{opt} becomes smaller as λ and D decrease. Especially, when $D = 1$ km, the outage performance with \hat{K}_{opt} becomes extremely close to that with K_{opt} as β increases, which can be expected from the simulation results in Figure 7(b).

6. Conclusion

In this paper, we study the outage performance of the multihop wireless backhaul systems at mm-Wave in the presence of the blockage effects. Assuming that multiple SBSs are distributed in a cluster with the wired connection to each other and considering the spatial diversity in a cluster, the outage probability between two SBS clusters is derived. Through analysis and simulation, it is shown that there exists an optimal hop distance that minimizes the intercluster (perhop) outage probability. Then, assuming uniform SBS clusters we extend the perhop outage analysis to the multihop scenario, where we find that there exist optimal hop distance and hop count that minimize the end-to-end outage probability between the MBS and the destination SBS cluster when the end-to-end distance is given. Using the same trend of the perhop and multihop outage performances with respect to the perhop distance, we propose the suboptimal hop distance and corresponding suboptimal hop count. The suboptimal hop count shows a small gap to the optimal hop count, which means that the exhaustive search range of the optimal hop count can be significantly reduced. Potential extensions of this paper include addressing a wider scenario with dissimilar sizes and densities of the SBS clusters.

Competing Interests

The authors declare that they have no competing interests.

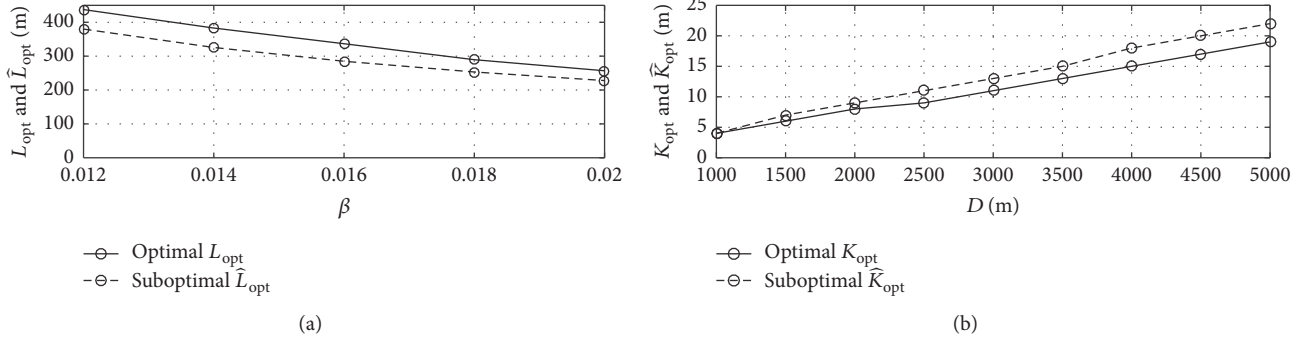


FIGURE 7: Optimal hop distance and hop count for $\lambda = 0.003$ and $b_k = 4$: (a) L_{opt} versus β and (b) K_{opt} versus D , when $\beta = 0.02$.

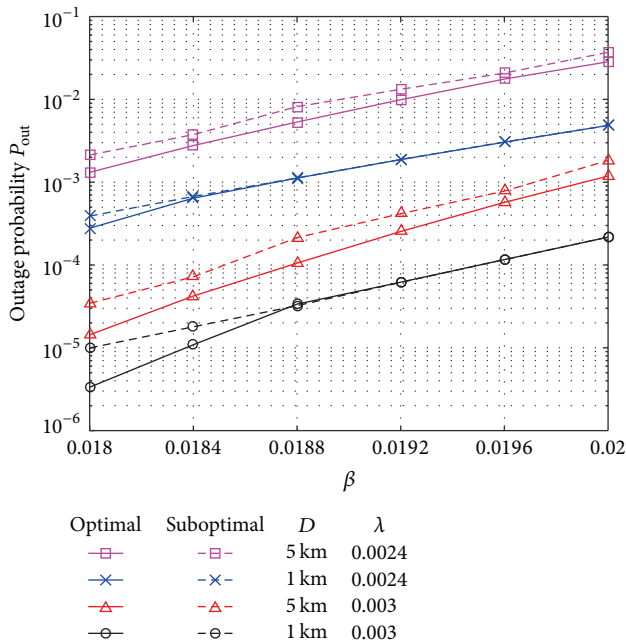


FIGURE 8: P_{out} versus β , when $b_k = 4$, $\lambda = \{0.0024, 0.003\}$, and $D = \{1 \text{ km}, 2 \text{ km}\}$.

Acknowledgments

This research was supported by Basic Science Research Program through the National Research Foundation of Korea (NRF) funded by the Ministry of Education (Grant no.: NRF-2016RID1A1B03930060).

References

- [1] U. Siddique, H. Tabassum, E. Hossain, and D. I. Kim, "Wireless backhauling of 5G small cells: challenges and solution approaches," *IEEE Wireless Communications*, vol. 22, no. 5, pp. 22–31, 2015.
- [2] W. Ni, I. B. Collings, X. Wang, and R. P. Liu, "Multi-hop point-to-point FDD wireless backhaul for mobile small cells," *IEEE Wireless Communications*, vol. 21, no. 4, pp. 88–96, 2014.
- [3] X. Ge, H. Cheng, M. Guizani, and T. Han, "5G wireless backhaul networks: challenges and research advances," *IEEE Network*, vol. 28, no. 6, pp. 6–11, 2014.

- [4] Z. Pi and F. Khan, "An introduction to millimeter-wave mobile broadband systems," *IEEE Communications Magazine*, vol. 49, no. 6, pp. 101–107, 2011.
- [5] S. Hur, T. Kim, D. J. Love, J. V. Krogmeier, T. A. Thomas, and A. Ghosh, "Millimeter wave beamforming for wireless backhaul and access in small cell networks," *IEEE Transactions on Communications*, vol. 61, no. 10, pp. 4391–4403, 2013.
- [6] T. S. Rappaport, S. Sun, R. Mayzus et al., "Millimeter wave mobile communications for 5G cellular: it will work!," *IEEE Access*, vol. 1, pp. 335–349, 2013.
- [7] T. S. Rappaport, F. Gutierrez, E. Ben-Dor, J. N. Murdock, Y. Qiao, and J. I. Tamir, "Broadband millimeter-wave propagation measurements and models using adaptive-beam antennas for outdoor Urban cellular communications," *IEEE Transactions on Antennas and Propagation*, vol. 61, no. 4, pp. 1850–1859, 2013.
- [8] S. Rajagopal, S. Abu-Surra, and M. Malmirchegini, "Channel feasibility for outdoor non-line-of-sight mmwave mobile communication," in *Proceedings of the IEEE Vehicular Technology Conference (VTC Fall '12)*, pp. 1–6, Quebec City, Canada, September 2012.
- [9] J. G. Andrews, S. Buzzi, W. Choi et al., "What will 5G be?" *IEEE Journal on Selected Areas in Communications*, vol. 32, no. 6, pp. 1065–1082, 2014.
- [10] S. Y. Seidel and T. S. Rappaport, "Site-specific propagation prediction for wireless in-building personal communication system design," *IEEE Transactions on Vehicular Technology*, vol. 43, no. 4, pp. 879–891, 1994.
- [11] A. Toscano, F. Bilotti, and L. Vegni, "Fast ray-tracing technique for electromagnetic field prediction in mobile communications," *IEEE Transactions on Magnetics*, vol. 39, no. 3, pp. 1238–1241, 2003.
- [12] T. Bai, R. Vaze, and R. W. Heath, "Analysis of blockage effects on urban cellular networks," *IEEE Transactions on Wireless Communications*, vol. 13, no. 9, pp. 5070–5083, 2014.
- [13] A. Ghosh, N. Mangalvedhe, R. Ratasuk et al., "Heterogeneous cellular networks: from theory to practice," *IEEE Communications Magazine*, vol. 50, no. 6, pp. 54–64, 2012.
- [14] T. Bai and R. W. Heath, "Coverage and rate analysis for millimeter-wave cellular networks," *IEEE Transactions on Wireless Communications*, vol. 14, no. 2, pp. 1100–1114, 2015.
- [15] J. Choi, "On the macro diversity with multiple BSs to mitigate blockage in millimeter-wave communications," *IEEE Communications Letters*, vol. 18, no. 9, pp. 1623–1656, 2014.
- [16] H. Jung and I. Lee, "Outage analysis of millimeter-wave wireless backhaul in the presence of blockage," *IEEE Communications Letters*, vol. 20, no. 11, pp. 2268–2271, 2016.

- [17] P. Billingsley, *Probability and Measure*, John Wiley & Sons, 2012.
- [18] J. G. Andrews, F. Baccelli, and R. K. Ganti, "A tractable approach to coverage and rate in cellular networks," *IEEE Transactions on Communications*, vol. 59, no. 11, pp. 3122–3134, 2011.
- [19] I.-H. Lee and D. Kim, "Spatial channel reuse in multi-hop decode-and-forward relaying systems in high path loss environments," *IEEE Communications Letters*, vol. 16, no. 7, pp. 990–993, 2012.